TISSUE ENGINEERED CANCER MODELS FOR IN VITRO RECAPITULATION OF THE NATIVE TUMOR MICROENVIRONMENT

by

Nicole Lee Habbit

A thesis submitted to the Graduate Faculty of
Auburn University
in partial fulfillment of the
requirements for the Degree of
Master of Science

Auburn, Alabama
August 4, 2018

Keywords: Cancer Tissue Engineering, Tumor Microenvironment,
in vitro Tumor Model, PEG-fibrinogen

Approved by

Elizabeth A. Lipke, Chair, Mary and John H. Sanders Endowed Associate Professor
of Chemical Engineering
Robert D. Arnold, Associate Professor of Drug Discovery and Development
Allan E. David, John W. Brown Associate Professor of Chemical Engineering
Virginia A. Davis, Alumni Professor of Chemical Engineering

Abstract

Despite having been first documented over 5000 years ago, cancer remains one of the most prevalent and lethal diseases to plague the human race to date. According to the National Cancer Institute, nearly half of Americans will be diagnosed with cancer during his or her lifetime, while the global incidence of cancer is projected to reach 21 million new cases diagnosed annually within the next decade. Thus, it has become exceedingly critical that highly-effective anti-cancer therapeutics be expeditiously developed and made clinically available. However, the current likelihood of approval for experimental oncology drugs entering clinical trials is only 5.1%. This poor performance can be partially attributed to the lack of a preclinical therapeutic testing platform that recapitulates the complex tumor microenvironment *in vitro*, and accurately predicts drug behavior in the human body.

Through the amalgamation of recent advancements in novel biomaterial synthesis and cancer cell biology, this study reports the development of a physiologically relevant *in vitro* bioengineered tumor tissue model that transcends the limitations of conventional two-dimensional, cell aggregate, or murine model platforms. Bioengineered tumor tissues were fabricated utilizing poly(ethylene glycol) based hydrogels, functionalized with denatured fibrinogen to support cell adhesion and cell-mediated remodeling of the polymer matrix milieu. A myriad of experiments were performed to characterize encapsulated cell behavior and validate the potential utility of the model to bridge the translational gap between preclinical and clinical trials. Chapter 1 elucidates tumorigenic progression and reviews

the current state of drug development processes and the cancer tissue engineering field. Chapter 2 reports the development and subsequent characterization of a bioengineered prostate tumor tissue model utilizing two prostate cancer cell lines in coculture with stromal fibroblasts. Chapter 3 presents a novel *in vivo-in vitro* tumor stiffness comparison study and investigates the effect of matrix stiffness on encapsulated prostate tumor cell behavior. Chapter 4 expounds the utility of the bioengineered tumor tissue model in personalized medicine and its ability to preserve cell populations of interest derived from colorectal cancer patient-derived xenograft tumors. Finally, the recommended future directions of the study are delineated, including extension to a notable microfluidic tumor-on-a-chip platform.

Acknowledgments

I would like to thank Dr. Elizabeth A. Lipke for her guidance and mentorship throughout the duration of this research project. I would like to also thank my committee members, Dr. Robert D. Arnold, Dr. Allan E. David, and Dr. Virginia A. Davis for their support and dedication. I would like to again thank Dr. Robert D. Arnold and Dr. Allan E. David, in addition to Dr. Tareq B. Anani, Dr. Balabhaskar Prabhakarpandian, Dr. Michael W. Greene, and Dr. Peter R. Panizzi for their collaborative assistance.

Next, I would like to thank current and former members of the Lipke Lab including Benny Anbiah, Morgan Ellis, Ferdous Finklea, Iman Hassani, Dr. Jessica Kelly, and Yuan Tian for their advice, support, and friendship. I would like to further thank the other Lipke Lab cancer researchers, Benny Anbiah and Iman Hassani, for their guidance and collaboration, without which this project would not be possible. I would like to expressly thank my undergraduate researchers, Luke Anderson and Joshita Suresh, for their assistance both experimentally and analytically, in addition to their immense work ethic, motivation, and friendship.

I would like to thank my Auburn Chemical Engineering graduate student family for their encouragement and for making my time at Auburn unbelievably fun. Lastly, but most importantly, I would like to thank my parents, Robert and Kelli Habbit, as well as my brother, Bobby Habbit, for their unending love, support, and encouragement throughout every single day of my life. I would not be here without your guidance.

Table of Contents

List of Tables

List of Figures

List of Abbreviations

^{1}H NMR	Proton Nuclear Magnetic Resonance
2D	Two-Dimensional
3D	Three-Dimensional
ADT	Androgen Deprivation Therapy
ANOVA	Analysis of Variance
APMA	4-Aminophenylmercuric Acetate
B2M	Anti-Human Beta-2-Microglobulin Antibody Clone
BCA	Bicinchoninic Acid Assay
BCE	Before Common Era
BSA	Bovine Serum Albumin
$CaCl_2$	Calcium Chloride
CAFs	Cancer Associated Fibroblasts
CAT	Catalog Number
cDNA	Complementary Deoxyribonucleic Acid
CK20	Anti-Keratin 20 D9Z1Z XP® Antibody Clone
CO_2	Carbon dioxide
CRC	Colorectal Cancer
CT	Computerized Tomography

CY5HQ	Cyanine 5
DAPI	4',6-Diamidino-2-Phenylindole
DMEM	Dulbecco's Modified Eagle's Medium
DMSO	Dimethyl Sulfoxide
DNAse	Deoxyribonuclease I
Em	Emission
EMT	Epithelial-Mesenchymal Transition
Ex	Excitation
F-12K	Kaighn's Modification of Ham's F-12K Medium
FBS	Fetal Bovine Serum
FDA	US Food & Drug Administration
FGF-2	Fibroblast Growth Factor-2
FITC	Fluorescein Isothiocyanate
Foxp3	Foxp3 Fixation and Permeabilization Solution
FRET	Fluorogenic Resonance Energy Transfer
G1	Group 1 Mice
G2	Group 2 Mice
GEMMs	Genetically Engineered Mouse Models
GFOGER	Gly-Phe-hydroxyproline-Gly-Glu-Arg peptide

GFP	Green Fluorescent Protein
H2Db	Anti-Mouse MHC Class I H-2 Db Antibody Clone
H33342	bisBenzimide Hoechst 33342 Fluorochrome
HA	Glycosaminoglycan Hyaluronic Acid
HBSS	Hank's Balanced Salt Solution
HPC	High-Perfusion Chip
hTERT	Human Telomerase Reverse Transcriptase
HTS	High Throughput Screening
HUVECs	Human Umbilical Vein Endothelial Cells
IKVAV	Ile-Lys-Val-Ala-Val peptide
IND	Investigational New Drug
Ki67	Anti-Ki67 Antibody Clone
LPC	Low-Perfusion Chip
MHC	Major Histocompatibility Complex
MMP	Matrix Metalloproteinase
$MSIgG_1$	Mouse IgG_1 Isotype Control
$MSIgG_{2a}$	Mouse IgG_{2a} Isotype Control
MSOT	Multispectral Optoacoustic Tomography
NaCl	Sodium Chloride

NCI	National Cancer Institute
NDA	New Drug Application
nHA	Nanohydroxyapatite
NK	Natural Killer
NVP	1-vinyl-2-pyrrolidinone
PA	Polyacrylamide
PBLs	Peripheral Blood Lymphocytes
PBS	Phosphate Buffered Saline
PCa	Prostate Cancer
PCL	Poly(ε-caprolactone)
PDMS	Poly(dimethyl siloxane)
PDX	Patient-Derived Xenograft
PEG	Poly(ethylene glycol)
PEGDA	Poly(ethylene glycol) diacrylate
Pen-Strep	Penicillin-Streptomycin
PF	Poly(ethylene glycol)-fibrinogen
PF+1%P	PF with 1% (w/v) excess PEGDA
PF+2%P	PF with 2% (w/v) excess PEGDA
PFA	Paraformaldehyde

PGA	Poly(glycolic acid)
PLA	Poly(lactic acid)
RADA	Arg-Ala-Asp-Ala peptide
RBIgG	Rabbit IgG Isotype Control
Red-FLuc	Red Shifted Firefly Luciferase
RFU	Relative Fluorescence Units
RGD	Arg-Gly-Asp peptide
ROI	Regions of Interest
RPMI	Roswell Park Memorial Institute
SD	Standard Deviation
TAMs	Tumor Associated Macrophages
TCEP-HCl	Tris (2-carboxyethyl) Phosphine Hydrochloride
TE-7	Anti-Fibroblast Antibody Clone
TEOA	Triethanolamine
TME	Tumor Microenvironment
TRIS-HCl	TRIS Hydrochloride
TRITC	Tetramethylrhodamine
US	United States
VEGF	Vascular Endothelial Growth Factor

Introduction

While the term cancer, translated from *carcinos*, was first introduced in 400 BCE by the ancient Greek physician Hippocrates, tumorigenic growths in the human body have been perpetually chronicled since the dawn of recorded history. The first known descriptions of cancerous masses were found in an Egyptian trauma surgery textbook, the *Edwin Smith Surgical Papyrus*, written in 3000 BCE, in which the script states, "There is no treatment" for the tumors.[1] Ancient techniques to combat both malignant and benign growths were comprised of cauterization and primitive surgical removal of the affected tissue. Tumor recurrence was often noted, and many physicians and scientists alike concluded that cancer could not be cured, a mindset that translated well into the 20th century. Throughout the roughly 5,000 years since the initial documentation of cancer, modern medicine has evolved to generate advanced diagnostic and therapeutic methodologies, however, a cure for the disease has yet to be discovered.

According to the National Cancer Institute (NCI), approximately 39.6% of Americans will be diagnosed with cancer during his or her lifetime; furthermore, the global incidence of cancer is projected to increase by 50% to 21 million new cases diagnosed annually by the year 2030.[2] Beyond affecting numerous lives, cancer also presents as an immense societal burden with an annual global economic cost of US $1.16 trillion, which is projected to increase by 70% within the next two decades.[3] Therefore, it has become

increasingly critical that highly effective anti-cancer therapeutics are expeditiously developed and made clinically available.

Although often referred to as a singular disease, cancer encompasses a wide range of pathophysiological disorders in which at least one genetically mutant cell divides uncontrollably, resulting in tumorigenesis.[4] A myriad of factors, entitled the hallmarks of cancer, have been found to enable tumorigenic progression. They have been defined as sustaining proliferative signaling, evading growth suppressors, resisting cell death, enabling replicative immortality, inducing angiogenesis, activating invasion and metastasis, reprogramming energy metabolism, and evading immune destruction.[5,6] The combinatorial effect of these hallmarks results in an extremely heterogeneous pathological profile that is characterized by both genotypic and phenotypic inter- and intratumoral variations.[7] It additionally initiates a cascade of highly complex cellular and molecular pathways which aid in the formation of and operate within the native tumor microenvironment (TME).[7,8]

The field of tissue engineering has emerged to implement chemical and biomedical engineering principles in the combination of novel biomaterials with cells and bioactive factors to construct functional tissue models.[9] More specifically, cancer tissue engineering research efforts aim to recapitulate the complexity of the TME for application in disease mechanism investigations and pharmacological testing.[10] The purpose of this thesis was to engineer three-dimensional (3D) biomimetic tumor tissues utilizing the hybrid biomaterial, poly(ethylene glycol)-fibrinogen (PF), as a tunable scaffold for cell adhesion and proliferation. Through the amalgamation of recent advancements in both cancer biology and biomaterial design and synthesis, the engineered tumor tissues were characterized and

modulated to closely mimic both biochemical and biophysical characteristics of tumors *in vivo*.

Chapter 1.   Background

1.1. The Drug Development Pathway

Bringing a new pharmaceutical drug to the market is a tremendously lengthy process during which the therapeutic is subjected to a myriad of investigations to determine its safety and efficacy. It is currently estimated that, on average, it takes between 10-15 years and approximately US $800 million to US $1 billion to successfully research and develop one new therapeutic.[11] Upon discovery, the development pathway begins with the preclinical research phase which serves to investigate the pharmacological profile and acute toxicity of the drug and its metabolites both *in vitro* and in at least two animal species *in vivo*.[12] If the therapeutic is found to be reasonably safe during this stage, an Investigational New Drug (IND) application can be filed with the US Food & Drug Administration (FDA) to begin clinical research.

Clinical trials are then conducted in four major phases with each geared towards answering a specific question about the safety and efficacy of the experimental agent *in vivo*. Phase I aims to investigate drug behavior and interaction in the diseased human body while determining the appropriate dosage to maximize treatment potential and limit side effects to an acceptable level.[12] Phase II then implements the dose found to be safest and most effective during Phase I in a larger number of participants to closely monitor how well the therapeutic achieves the goal of the treatment, as well as investigate rare side

effects.[12] Phase III further augments the Phase II findings by monitoring efficacy in a much larger patient population over a longer treatment period to examine both the desired and undesired long-term effects of the therapeutic. Furthermore, Phase III trials serve to determine how the experimental agent compares to the current standard treatment in terms of both safety and efficacy.[12] Upon successful completion of Phase III, a New Drug Application (NDA) is filed with the FDA to acquire approval for general use in patients with the disease for which it was tested. Finally, Phase IV serves to continuously monitor the FDA approved drug throughout its lifetime on the market to ensure it is still appropriately safe and efficacious to continue to be administered to patients.[12] Moreover, Phase IV considers factors such as treatment cost and patient quality of life that are not investigated during Phases I through III.

1.2. The Critical Need for Physiologically Relevant *In Vitro* Tumor Models

The compound probability of progressing from Phase I trials to FDA Approval for all drug development programs combined is only 9.6%, with the largest failure occurring at the progression from Phase II to Phase III.[13] Oncology drug development programs had an outsized, detrimental effect on the overall clinical trials success rate with only 5.1% of experimental drugs being successfully approved between 2006 and 2015.[13] This poor clinical translation leads to the conclusion that current preclinical therapeutic testing platforms are not nearly rigorous enough to accurately predict drug behavior in the human body.

In vitro preclinical studies are conventionally performed on two-dimensional (2D) cell sheets or 3D multicellular aggregate testing platforms. While these methods provide some insight into cell-therapeutic interactions, they are severely limited in their physiological relevancy and ability to model tumorigenic progression. 2D cell sheet cultures do not recapitulate important 3D cell-cell interactions formed in tumors *in vivo*, resulting in severe morphological and phenotypical deviations.[14,15] Cancer cells cultured in 2D have been found to present diversified receptor proteins and drug transporters, in addition to decreased metabolizing enzyme activity, leading to a lower innate resistance to anti-cancer drugs.[14] Furthermore, 2D cell sheet tissues also fail to recapitulate the limited molecular transport and subsequent differential drug distribution gradient found in tumors *in vivo*.[16,17] As a result, agents administered to 2D tissue cultures experience a near-infinite residence time during which they can initiate a therapeutic effect on each cell present in the culture, thus leading to a vast overestimation of their clinical capabilities.[18,19]

Multicellular aggregates, or tumor spheroids, have emerged to address the dimensionality limitations of 2D cell sheets by culturing clumps of cancer cells in 3D formation, thus allowing biochemical gradients to form across the mass. Many fabrication methods have been reported including cell suspension spinner flasks, liquid-overlay, hanging-droplet, non-adherent microwell, and microfluidic techniques.[20] Fundamentally, each of these methods preferentially initiate cell-cell interaction by suppressing cell-substrate interaction, thus inducing cellular aggregation. While tumor cell aggregates have the ability to express thickness-dependent genotypic and phenotypic cellular variations and can be used in high-throughput screening (HTS), they are limited by poor structural control, high batch to batch variability, and difficulty in employing multiple or non-aggregating

cell types.[20,21] Therefore, 3D tumor spheroids offer little more clinical relevancy than do 2D cell sheets.

In vivo preclinical studies employ animal models to provide the necessary drug safety and efficacy data needed for translation from bench to bedside. Furthermore, animal models provide a platform to study the events of tumorigenic progression from normal to invasive neoplastic tissue. Murine species, or rodents, are used most often and can be genetically engineered to develop *de novo* tumors or to modulate and humanize their immune response. Each mouse strain presents its own advantages and disadvantages in terms of its ability to serve as a preclinical oncology model. For example, immunocompetent syngeneic mice or genetically engineered mouse models (GEMMs) provide the ability to model a complete TME representative of the studied tumor with comprehensive stroma and murine immunity, however, experimental compounds must be cross-reactive for both humans and mice as the tumor will be comprised of only murine cells.[22,23] Meanwhile, human-derived xenografts on immunodeficient mice allow analysis of human tumor response to administered therapeutics, however, they are unable to fully capture the intact human immune factor and complex tumor milieu.[22]

Several additional challenges face all murine model studies, regardless of mouse strain. These include costly animal maintenance, slow tumor development, complicated orthotopic implantation, dissimilar metabolic processes, limited accessibility for imaging and analysis, and most notably, poor predictive value.[22,24] As a result, *in vivo* preclinical models fail to preferentially select efficacious, clinically translatable therapeutics, and thus cannot successfully bridge the gap between 2D *in vitro* and human studies. To begin to address some limitations of both *in vitro* and *in vivo* preclinical testing platforms, it is

imperative that 3D engineered tumor tissue models be developed and implemented in the drug development process.
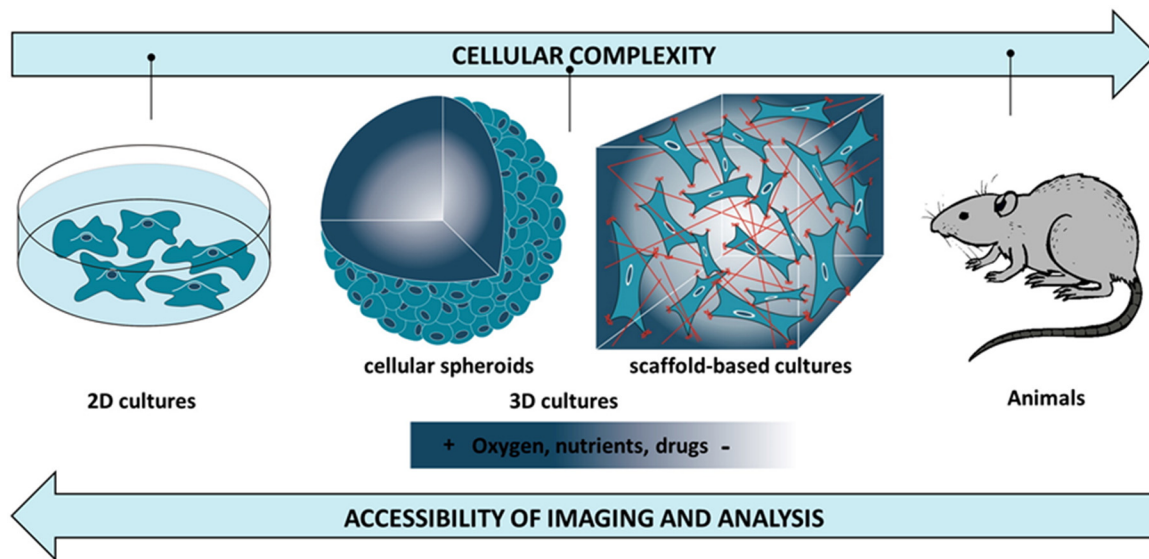
Figure 1: Preclinical anti-cancer therapeutic testing platforms. *Advancements in the field of 3D tissue engineering allow preclinical testing models to combine the advantages of increased cellular complexity and physiological relevancy in vitro over 2D models, in addition to the ability to more easily analyze tumor cell behavior in comparison to animal studies in vivo. (Reprinted with permission from Alemany-Ribes et al. 2014)*

1.3. Tumorigenic Progression and the Native Tumor Microenvironment

The native TME is a multifarious network characterized by spatial and temporal heterogeneities, and is found to contain genetically and phenotypically variable tumor, stromal, vascular endothelial, and immune cells embedded within the extracellular matrix (ECM).[25,26] Tumorigenic progression, and thereby formation of the TME, is initiated as a result of the uncontrollable division of a singular or small group of genetically mutant

cell(s). Mutations are often thought to occur in a proto-oncogene, tumor-suppression gene, or stability gene, which result in stimulation of cellular division, prevention of apoptotic processes, and inability to mitigate detrimental genetic alterations, respectively.[4]

While a tumor can be originated from a single mutation, not all tumor cells within the TME are genotypically and phenotypically similar. Intratumoral, or subclonal, heterogeneity often arises as a result of spatial variations within the TME, which are derived from immediate cell population, biochemical gradients, and microarchitectural structure.[7,26,27] Tumor cells are found to adapt to changes in their immediate milieu and as a result, phenotypically express features that ensure their survival.[7,28]

As the tumor cells proliferate and commence the neoplastic process, they begin to recruit stromal cells, attract infiltrates of inflammatory cells, and initiate angiogenesis, or the formation of new blood vessels.[8] Once entrapped within the TME, each of these cell types tend to deviate from their normal physiological roles and are coerced to promote tumorigenic progression.[8,29] For example, tumor associated macrophages (TAMs) are found to secrete pro-tumorigenic proteases, cytokines, and growth factors; similarly, cancer associated fibroblasts (CAFs) secrete ECM proteins and basement membrane components, while also suppressing immune response and supporting angiogenesis.[30]

As cells embedded within the TME proliferate to form cell-cell junctions and construct the ECM, several biophysical characteristics emerge within the tumor mass such as increased ECM stiffness, high interstitial pressure, and incomplete leaky vascularization.[29,31] These, in turn, induce biochemical gradients of pH, oxygen and nutrients, and metabolic waste, which most often lead to acidosis and hypoxia.[29,32] As a result, distinct zones develop within the 3D tissue in which cellular behavior varies

drastically. Tumor cells at the core of the mass experience a highly acidic environment with little to no oxygen or nutrients and increased accumulation of metabolic waste; therefore, the tissue becomes necrotic.[33,34] Conversely, tumor and stromal cells at the periphery of the mass are subjected to a highly vascularized environment and are thus tremendously proliferative and prone to metastasize.[30,33,34] Cells found at the midpoint of the mass, between the necrotic core and proliferative periphery, exist in a quiescent state in which they remain alive, however, do not actively divide.[34]

Metastasis, or the development of secondary tumor growths in tissues and organs beyond the point of origination, is the phenomenon that most directly results in cancer patient mortality.[35] It begins when primary tumor cells invade through the basement membrane and intravasate in to the vascular system.[36] From there, the tumor cell can circulate throughout the body until it preferentially extravasates at a distal location based upon the tissue or organ milieu. Increasing evidence has demonstrated that tumor metastasis is likely enabled via the epithelial-mesenchymal transition (EMT), during which polarized epithelial cells assume a mesenchymal phenotype and thus, acquire migratory and invasive properties.[37,38] Factors such as vascular structure, blood flow, tissue stiffness, and the presence of metastasis-initiating cells all contribute to the preferential metastatic pattern of circulating tumor cells.[30,35,39-41]

Collectively, the TME is a highly intricate network that directly contributes to the complex pathophysiology of cancer. Therefore, it is imperative to accurately recapitulate as many characteristics of the TME as possible when engineering a biomimetic *in vitro* cancer model for use in anti-cancer therapeutic testing.
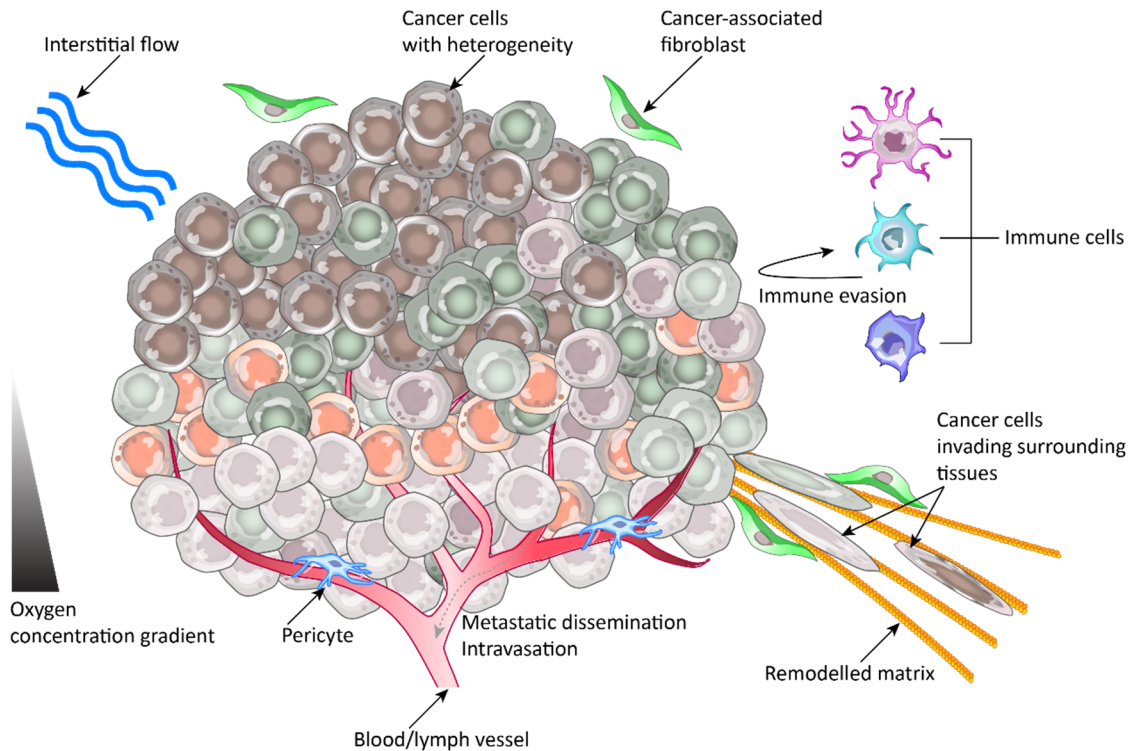
Figure 2: Characteristics of the complex tumor microenvironment. *The native TME encompasses numerous spatial and temporal heterogeneities that ultimately result in well-defined inter- and intratumoral variations. Tumors in vivo exhibit non-uniform vascularization, induced oxygen and nutrient gradients, evasive immune responses, high interstitial pressure, and invasion and metastatic dissemination of cancer and stromal cell types. (Adapted with permission from Junttila et al. 2013)*

1.4. Cell Sources for Cancer Tissue Engineering

As previously defined, cancer tissue engineering aims to combine novel biomaterials with cells and bioactive factors to produce functional tumor tissues. Cancer cells, as well as occasionally other supporting cell types, are employed in the model and

are primarily derived from two sources: commercially available immortalized cell lines and patient-derived cells.

1.4.1. Immortalized Cell Lines

Human-derived cancer cell lines are the most widely used cell source employed in the investigation of cancer biology and anti-cancer therapeutic testing. Cell lines are originated from a patient and are immortalized to acquire the ability to avoid replicative senescence and undergo unlimited divisions *in vitro*. The immortalization process can be performed via numerous methods of genetic manipulation; for example, the introduction of an exogenous human telomerase reverse transcriptase (hTERT) complementary deoxyribonucleic acid (cDNA) sequence encoding the catalytic subunit of telomerase can prevent the shortening of telomeres during the replication process, thus immortalizing the cell.[42] Cell lines directly derived from tumors, however, innately demonstrate an infinite lifespan *in vitro*, signifying that tumor cells *in vivo* evade telomere attrition and subsequently, replicative senescence, which contributes to their high proliferative capacity.[43]

The use of cell lines in cancer tissue engineering boasts numerous advantages such as an unlimited supply of a pure cell population, ability to yield reproducible results, and cost-effective culture.[44] However, this in turn, introduces a set of limitations to their clinical relevancy. Cell lines at early passage numbers are genetically homogeneous, however, with serially increasing passages, cells may begin to express genotypic and phenotypic variations within a singular culture.[44] Additionally, cell lines certainly do not incorporate the full range of cells found in tumors *in vivo*; moreover, the cancerous cells present often demonstrate poor correlation when compared back to tumor primary cells due to prolonged

2D culture *in vitro*.[44-46] This significantly impacts their native function and response to external stimuli, and thus detracts from their ability to serve as a clinically relevant, predictive therapeutic testing platform.

1.4.2. Patient-Derived Cells

To fully recapitulate both the genotypic and phenotypic variations of the myriad of cell types found in tumors *in vivo*, patient-derived cells must be employed. These cells originate from a current patient and are typically expanded in a mouse model prior to their implementation in cancer research efforts. To begin, tumor tissue samples are excised from the human patient and either dissociated to collect the cells or immediately grafted as a solid mass into the flank of immunocompromised mice.[47-50] This process is typically repeated multiple times to examine changes in the cell population and phenotypic expression after each regraftment, as well as to develop a bank of cells for future experimentation. Investigations utilizing patient-derived cells typically harvest the cells in one of two ways: first, cells from the primary tumor or from a subsequent induced murine tumor can be further passaged *in vitro* in 2D culture.[47,49,51] These are referred to as primary cells or primary cell lines. Second, cells can be used for experimentation immediately upon tumor excision and dissociation; these are denoted as patient-derived xenograft (PDX) cells.[47,49]

Primary and PDX cells are found to more closely resemble the inter- and intratumoral cellular heterogeneity of the native TME than do immortalized cell lines.[52] Important factors such as microarchitecture and gene expression profiles have been shown to be well preserved in PDX models.[53-55] Furthermore, when grafted into humanized mouse

models, these cells provide important insight into cancer biology and tumorigenic progression *in vivo*.[52,56]

While patient-derived cell sources overcome many limitations of immortalized cell lines, inherent impediments are unavoidable. Most notably, primary and PDX cells are extremely unstable and will express major deviations from the original tumor upon serial passaging.[52] Additionally, due to their propagation in host animals, a significant portion of the cell population is non-human, thus significantly affecting cell-cell interactions and targeting strategies. Finally, patient-derived cell sources are extremely limited, involve complex techniques, and require immense time and monetary investments throughout the duration of their use.[52]

1.5. Biomaterials for Cancer Tissue Engineering

Recent advances in biomaterial synthesis and characterization have revolutionized the cancer tissue engineering field by introducing precise control over the biochemical and biophysical cellular microenvironment, thus overcoming the limitations of 2D cell sheets and providing critical physiological context. As previously discussed, 2D cell culture does not accurately recapitulate the microarchitecture of the native TME, and as a result, induces both genotypic and phenotypic aberrations *in vitro*. By equipping the cells with a 3D biomaterial scaffold, crucial cell-cell and signaling interactions are facilitated, resulting in the presentation of native tumor-mimetic morphology, gene and protein expression, and reactivity to anti-cancer therapeutics.[57-60] Biomaterials in cancer tissue engineering can be

classified in three key categories: natural, synthetic, and hybrid, and are preferentially

chosen based upon the specific microenvironmental cues required by the application.[57]
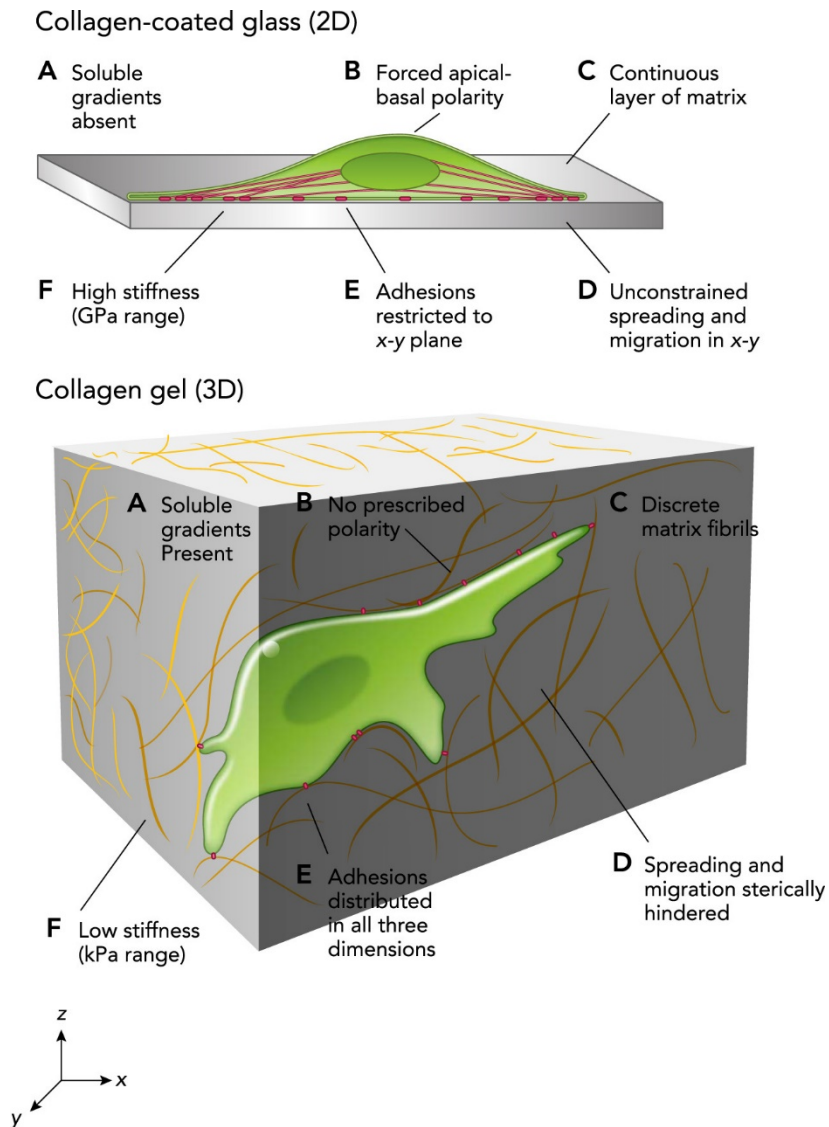
Figure 3: Biophysical advantages of 3D cell culture versus 2D cell culture. *The implementation of 3D engineered matrix scaffolds in cell culture introduces important biophysical cues at a cellular level, and thus yields more physiologically relevant cell behavior and morphology in vitro. (Reprinted with permission from Duval et al. 2017)*

1.5.1. Natural Biomaterials

Natural biomaterials are typically derived from plant or animal sources, and as a result, have the ability to more accurately recapitulate native ECM structure and stiffness, as well as cell-matrix interactions. Collagen, Matrigel, glycosaminoglycan hyaluronic acid (HA), and decellularized human tissue ECM are most frequently used in cancer tissue engineering, and offer an ample presence of ligands for cell adhesion, as well as cell-mediated matrix degradation sites.[58] Furthermore, due to the often fibrillar network of natural biomaterials, they are excellent candidates for the investigation of cellular migration and cancer cell metastasis.[61-63] This in turn, however, introduces a set of limitations including batch to batch variation, limited culture time due to scaffold remodeling, very limited control over the matrix and its mechano-architectural properties, and loss of biochemical functionality upon additional physical crosslinking.[58,59]

1.5.2. Synthetic Biomaterials

Conversely, synthetic biomaterials feature heightened control over the matrix complexity, as well as tunable physical physiognomies such as stiffness, pore size, and crosslinking density.[57] Common polymers include polyacrylamide (PA), poly(ε-caprolactone) (PCL), poly(lactic acid) (PLA), poly(glycolic acid) (PGA), and poly(ethylene-glycol) (PEG), with each introducing unique advantages and disadvantages to the model. For example, PA is cytotoxic in 3D culture yet presents an immense range of tunable substrate mechanics; similarly, the polyesters (PCL, PLA, PGA, etc.) are non-cytotoxic, however, require an additional porogen processing step to ensure appropriate pore size for cell encapsulation and culture medium diffusion.[58,59,64,65] Altogether, most synthetic biomaterials also exhibit restricted bioactivity and rely on non-specific protein

adsorption from culture medium to support cell adhesion and proliferation; furthermore, while the degradation of the synthetic matrices is well-characterized and predictable, it is unable to be cell-mediated.[58] As such, encapsulated cells cannot temporally remodel their microenvironment as they migrate and proliferate through the polymer matrix.

1.5.3. Hybrid Biomaterials

Many limitations of both natural and synthetic biomaterials can be alleviated through supplemental engineering efforts to adjust the biophysical and biochemical characteristics of the substrate. These hybrid, or biosynthetic, materials are often crosslinkable, boast precise control over the scaffold and its mechano-architectural properties, as well as ensure the presence of bioactive components to augment the biomimicry of the model and promote appropriate tumor cell behavior *in vitro*. For example, synthetic polymers can be improved through the intercalation of integrin-binding cell adhesion sites, such as an Arg-Gly-Asp (RGD) tripeptide, or cell-mediated degradation sites, such as a matrix metalloproteinase (MMP) hexapeptide substrate linked with the amino acid blocks, Arg-Ala-Asp-Ala (RADA).[66,67] Conversely, novel natural biomaterial-derived matrices can be fabricated the through the functionalization and acrylation of bioactive hydrogels, such as HA, to permit increased crosslinking ability.[68,69] Similarly, denatured fibrinogen fragments can be PEGylated utilizing poly(ethylene glycol) diacrylate (PEGDA), thus resulting in a photocrosslinkable hybrid matrix featuring both cell adhesion and cell-mediated degradation sites.[70]

17
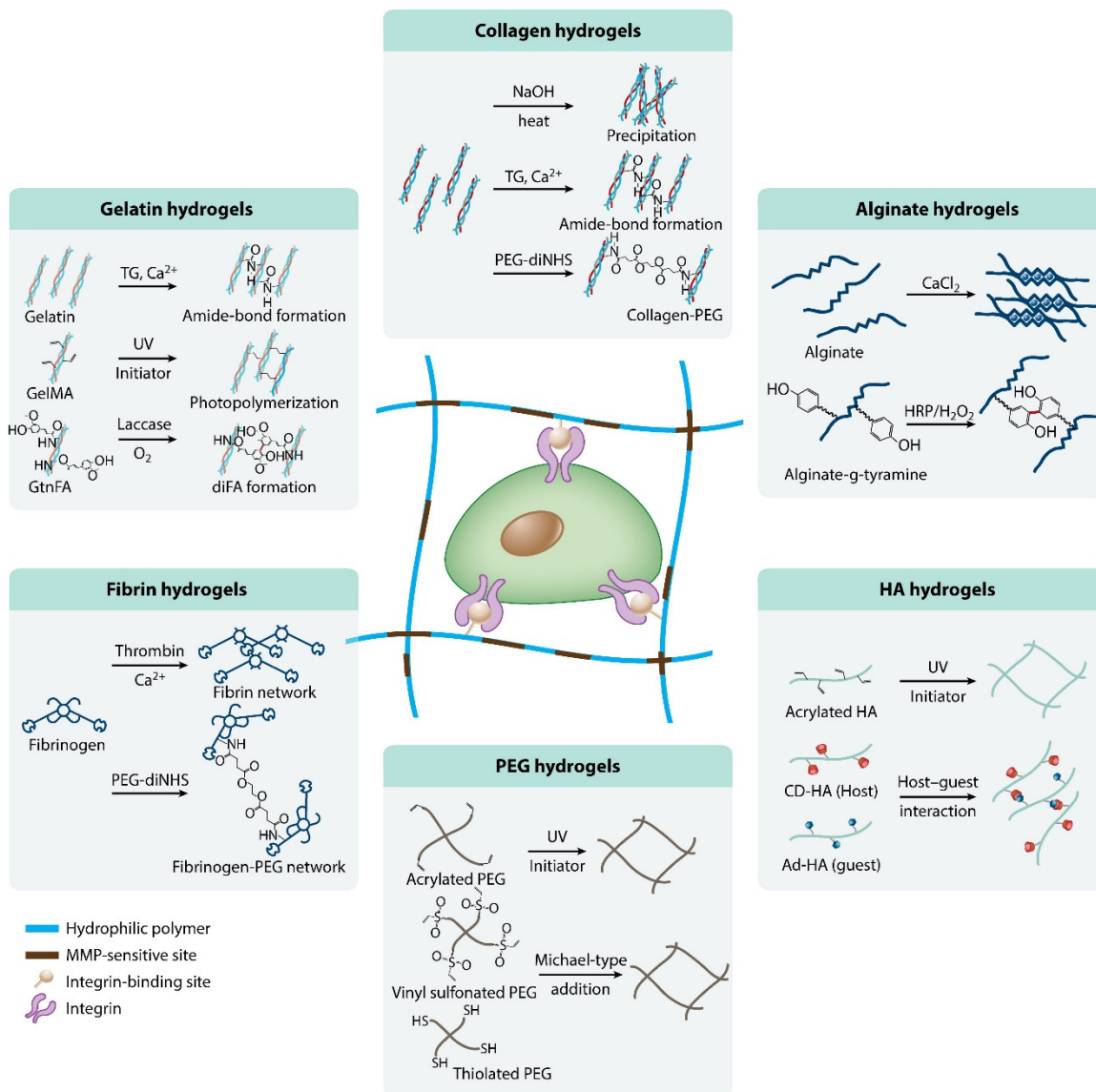
Figure 4: Examples of *in situ* crosslinkable hydrogels for 3D cell culture. *A wide variety of natural, synthetic and hybrid materials present the ability to be chemically, enzymatically, or photo- crosslinked to generate a scaffold for cell adhesion. (Reprinted with permission from Park et al. 2017)*

Overall, the incorporation of biocompatible materials in 3D cancer cell culture augments the ability of the *in vitro* model to mimic key characteristics of the native TME. Most notably, hybrid biomaterials boast the ability to amalgamate the biomimetic features of natural biomaterials required for appropriate cellular function with the tunability and reproducibility of synthetic biomaterials; thus, demonstrating immense potential for scalable production and increasing the likelihood of implementation in the drug development process.[71]

A Bioengineered Prostate Tumor Tissue Model for *In Vitro* Recapitulation of the Native Tumor Microenvironment

Chapter 2.   3D Coculture of Metastatic Prostate Cancer Cells and Stromal Fibroblasts in PEG-fibrinogen Based Hydrogels

2.1. Introduction

Prostate cancer (PCa) presents a high incidence rate in American men with approximately 1 in 9 being diagnosed during his lifetime; furthermore, 1 in 41 men will die as a direct result of PCa, rendering it the second leading cause of male cancer-related death in the US.[72] A cure for PCa does not currently exist, however, many traditional cancer treatment options are available to patients, such as active surveillance, surgery, and chemo- and radiation therapy. In advanced cases, these can also be administered in tandem with treatments such as the Sipuleucel-T cancer vaccine or androgen deprivation therapy (ADT) to increase patient life expectancy.[73] While effective in some cases, these treatments are often accompanied by painful and detrimental side effects, as well as potential tumor recurrence and the development of androgen-sensitive or castration-resistant tumor cells.[74] Similar to most types of cancer, there exists a great need for highly effective, clinically translatable anti-PCa therapeutics, however, the current development of experimental agents is critically hindered by the lack of a physiologically relevant, TME-mimetic drug testing platform.

The native PCa TME is generated through numerous biochemical signaling pathways between the tumor cells and surrounding stromal and epithelial milieu that result

in tumorigenic progression, initiation of the EMT, and subsequently, tumor metastasis to distal locations.[75,76] Stromal cells such as fibroblasts and endothelial cells are found to express increased remodeling of the ECM, amplified angiogenesis, and most notably, upregulated MMP activity.[74,77]

MMPs are a family of either soluble or membrane-anchored, zinc-binding endopeptidase enzymes involved in the degradation of the ECM, as well as the modulation of growth factor bioavailability.[78,79] More specifically, the gelatinases MMP-2 and MMP-9, provided by the stromal cadre, are found to not only promote release of angio- and lymphangiogenic factors *in vivo*, but also to cleave type IV collagen, which is ubiquitously abundant in the basement membrane.[79,80] By penetrating this physical barrier and supporting the foundation for metastasis, MMP-2 and MMP-9 create the opportunity for not only tumor cell invasion, but also infiltration of T-lymphocytes into the tumor mass, thus resulting in poor clinical prognoses.[79,81,82]

To begin to recapitulate the complex PCa TME *in vitro*, engineered tumor tissue models must address the following considerations: 1) the presence of human cancer, stromal, and/or immune cell types in coculture, 2) the use of a 3D scaffold that supports both cell adhesion and cell-mediated degradation, 3) the ability to modulate the mechanical properties of the scaffold to recapitulate native tissue microarchitecture, and 4) the ability to be maintained long-term for temporally-dependent cellular behavior investigations. Several models have been reported thus far, with most employing the commercially-available PC-3 or LNCaP PCa cell lines. The androgen insensitive, metastatic PC-3 PCa cells were initiated from a lumbar vertebral bone metastasis of a grade IV prostatic adenocarcinoma and are found to be highly aggressive.[83,84] Conversely, the androgen

sensitive LNCaP PCa cells were initiated from a left supraclavicular lymph nodal metastasis and are typically utilized to represent a more indolent form of PCa.[83,84]

Both LNCaP and PC-3 cells are reported to have been individually cocultured with supporting cell types in several biomaterials through the implementation of varying 3D fabrication techniques.[85-92] For example, in an effort to recapitulate the PCa bone metastasis microenvironment, PC-3 and LNCaP cells have been cocultured with a human fetal osteoblast cell line, hFOB 1.19, for up to 14 days at a 1:1 ratio by direct seeding onto disc-shaped collagen-nanohydroxyapatite (nHA) composite scaffolds.[85,86] Cell proliferation was found to be reduced by approximately 50%, while MMP-9 secretion was increased up to 4-fold in coculture relative to monoculture; thus indicating a more physiologically relevant microenvironment.[86] Utilizing a similar fabrication technique, PC-3 cells have also been employed in a 3D Matrigel coculture for 7 days at a 1:1 ratio with a human bone stromal derived cell line, HS-5, and were found to display upregulated invasive and proliferative qualities.[87] Furthermore, LNCaP cells have been directly seeded on 3D porous chitosan-alginate scaffolds, and cultured in the presence of human peripheral blood lymphocytes (PBLs) for 55 days to enable investigation of the interactions between tumor cells and tumor-infiltrating B cells, T lymphocytes, and natural killer (NK) cells.[88]

While each of these engineered tumors achieved a higher degree of physiological relevancy than 2D or monoculture models and enabled important investigations into coculture cell interactions, they are still hindered by limited control over the scaffold microarchitecture, as well as restricted cell-mediated matrix transformation. Recent studies have begun to address these constraints through the encapsulation of PC-3 and LNCaP cells, as well as endothelial cells, mesenchymal stromal cells, and primary human

osteoblasts, in PEG hydrogels functionalized with RGD, Gly-Phe-hydroxyproline-Gly-Glu-Arg (GFOGER), Ile-Lys-Val-Ala-Val (IKVAV), TG-MMP-Lys, or TG-Gln-RGD peptide motifs to support cell adhesion and cell-mediated degradation over periods of 14-28 days.[93-95] PEG is an FDA approved, highly biocompatible, crosslinkable polymeric material that offers tunable physical properties through the modulation of selected molecular weight, weight percent, or crosslinking density.[70,96-98] These synthetic hydrogels have thus far provided a basis for further investigation into important tumor-stromal cell-cell interactions yet are still limited by the need for complex peptide synthesis for polymer functionalization and limited production of biochemical cues for cell migration and proliferation.

To overcome the collective limitations of each of the aforementioned models, this study reports the encapsulation of metastatic PC-3 and LNCaP PCa cells, cocultured in varying cancer to stromal cell ratios with BJ-5ta human foreskin-derived fibroblasts, in 3D PF hydrogels. PF is a hybrid biomaterial comprised of a natural fibrinogen backbone covalently bound to synthetic difunctional PEG side chains.[70,99] Fibrinogen is abundantly present in the ECM, found to promote angiogenesis, cell proliferation, and cell migration through molecular interaction with fibroblast growth factor-2 (FGF-2) and vascular endothelial growth factor (VEGF), and is additionally naturally assembled and secreted by cancer cells in culture.[100-102] Furthermore, fibrinogen provides an enzymatically cleavable site for cell-mediated remodeling of the 3D culture scaffold, as well as two RGD cell adhesion sites found within the amino acid sequence of the fibrinogen α chain.[70,103]

PF is synthesized through a conjugate, or Michael-type, addition reaction between the acrylate end groups on PEGDA and free thiols on the fibrinogen cysteines.[99] It is

photocrosslinkable under high-intensity visible light in the presence of a free-radical photoinitiator, with and without the presence of a cell suspension, and thus can form a 3D biomimetic hydrogel tissue.[70,97,104,105] The bioengineered PF prostate tumor tissues discussed in this study aim to recapitulate key biochemical and biophysical characteristics of the native TME and as a result, provide insight into variations in tumor-stromal coculture cell interactions, cell-matrix interactions, and 3D cell behavior and growth in response to cell ratio and tumor cell type modulation. Overall, these findings can be further implemented in the fabrication of TME-mimetic *in vitro* 3D PCa models for application in anti-cancer therapeutic testing and disease modeling.

(A) PEGylated Denatured Fibrinogen (B) PEG-Fibrinogen Hydrogel Assembly
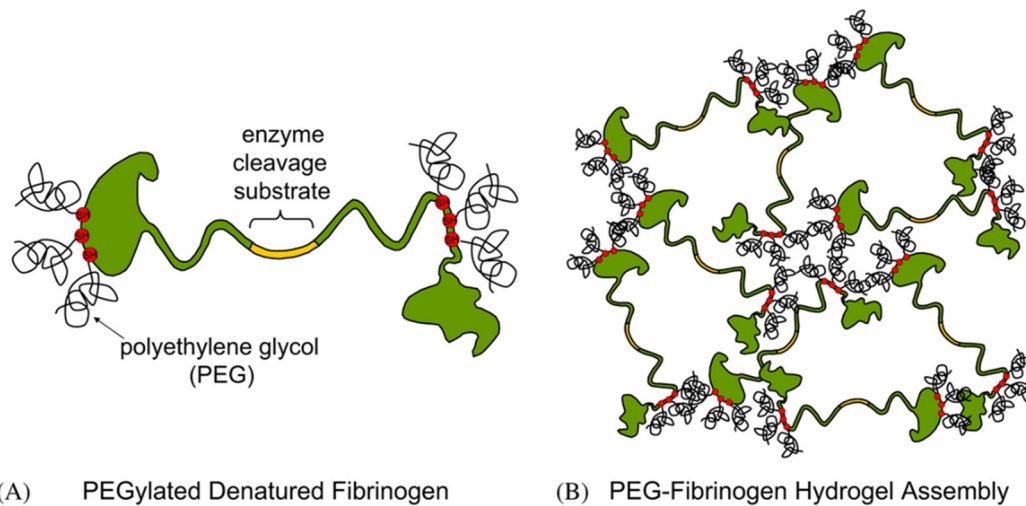
Figure 5: PEG-fibrinogen hydrogel assembly. *Denatured fibrinogen is functionalized utilizing poly(ethylene glycol) and can be photocrosslinked in the presence of a photoinitiator, under high intensity visible light, to form a 3D matrix conducive to cell adhesion and cell-mediated degradation. (Reprinted with permission from Almany et al. 2005)*

2.2. Materials and Methods

All chemicals were acquired from Sigma-Aldrich (St. Louis, MO) unless stated otherwise.

2.2.1. PEGDA Synthesis and Characterization

Poly(ethylene glycol) diacrylate (PEGDA) was synthesized according to established protocols.[106] 10kDA molecular weight PEG was reacted with acryloyl chloride (1:4 molar ratio) in anhydrous dichloromethane with triethylamine (1:2 molar ratio) under argon overnight at 25 ºC. The resultant PEGDA was purified through phase separation with 2M potassium carbonate. The organic phase, containing PEGDA, was dried using anhydrous magnesium sulfate and subsequently filtered. Finally, the synthesized PEGDA was precipitated utilizing diethyl ether, again filtered, and dried overnight under vacuum at 25 ºC. Proton nuclear magnetic resonance (^{1}H NMR) was performed to characterize the degree of acrylation achieved during synthesis. PEGDA was stored at -20 ºC.

2.2.2. PEG-fibrinogen Synthesis and Characterization

PF was synthesized according to established protocols.[70] Bovine fibrinogen was dissolved in an 8M urea solution in 10mM phosphate buffered saline (PBS) at a final concentration of 7 mg/mL. Tris (2-carboxyethyl) phosphine hydrochloride (TCEP-HCl) was added to the solution at a TCEP to fibrinogen cysteine molar ratio of 1.5:1. The final solution pH was adjusted to 8.0. Synthesized PEGDA was also dissolved and subsequently centrifuged in an 8M urea in 10mM PBS buffer solution at a final concentration of 280 mg/mL. The PEGDA solution was slowly added to the fibrinogen solution, and the consequent reaction was allowed to proceed under dark conditions for 3 hours at 25 ºC.

The reaction solution was next diluted with an equal volume of the urea-PBS buffer solution and precipitated through the addition of acetone at a 4:1 volumetric ratio of acetone to reaction solution. The precipitate product was separated from the liquid phase via centrifugation, weighed, and re-dissolved in the urea-PBS buffer at a final concentration of 2.2 mL buffer per gram of precipitate. The product solution was then dialyzed against 1L sterile PBS three times over a period of 24 hours under dark conditions at 4 ºC. The final PF product was aliquoted into sterile microcentrifuge tubes and stored at -80 ºC. A standard Pierce™ BCA Protein Assay Kit (Thermo Fisher Scientific, Rockford, IL) was utilized to characterize the protein concentration of the synthesized PF.

2.2.3. Cell Culture and Maintenance

PC-3 human prostatic adenocarcinoma cells were kindly provided by Dr. Allan David (Department of Chemical Engineering, Auburn University). PC-3 cells were cultured in F-12K (Kaighn's Modified Media) culture media (Corning®, Corning, NY) supplemented with 10% fetal bovine serum (FBS) (Atlanta Biologicals, Flowery Branch, GA) and 1% (v/v) penicillin-streptomycin (Pen-Strep) (GE Healthcare Bio-Sciences, Pittsburgh, PA). BJ-5ta normal human foreskin hTERT immortalized fibroblasts were acquired from ATCC (Manassas, VA) and were cultured in 4 parts of Dulbecco's Modified Eagle's Medium (DMEM) (Lonza, Walkersville, MD) containing 4 mM L-glutamine, 4.5 g/L glucose and 1.5 g/L sodium bicarbonate, and 1 part of Medium 199 (Lonza, Walkersville, MD) supplemented with 0.01 mg/mL hygromycin B (MilliporeSigma, Burlington, MA), and 10% FBS. LNCaP human prostatic carcinoma cells were also kindly provided by Dr. Allan David (Department of Chemical Engineering, Auburn University). LNCaP cells were cultured in Roswell Park Memorial Institute (RPMI)-1640 (Thermo

Fisher Scientific, Rockford, IL) culture media supplemented with 10% FBS and 1% (v/v) Pen-Strep.

All cells were maintained within plasma-treated polystyrene tissue-culture flasks stored in a humidified atmosphere with 5% carbon dioxide (CO_2) and a constant temperature of 37 ºC; culture media was renewed twice weekly. Cells adherently cultured in 2D were enzymatically dissociated from the tissue-culture flask surface in preparation for passaging or 3D culture utilizing 0.25% trypsin/2.21 mM EDTA (Corning®, Corning, NY).

2.2.4. Cell Encapsulation in PF Hydrogels

Bioengineered tumor tissues were formed in cylindrical shaped poly(dimethyl siloxane) (PDMS) molds, which were prefabricated for use in the encapsulation process. PDMS sheets were constructed utilizing the SYLGARD 184 Elastomer Kit (Thermo Fisher Scientific, Rockford, IL) and shaped utilizing a 4mm diameter biopsy punch. PDMS molds were firmly adhered to the bottom of a 6-well polystyrene plasma treated tissue-culture plate to prevent leakage of the cell-laden hydrogel precursor solution. The hydrogel precursor solution was prepared by adding 1.5% (v/v) triethanolamine (TEOA), 37 mM 1-vinyl-2-pyrrolidinone (NVP), and 0.1 mM Eosin Y as a photoinitiator to the synthesized PF in solution with 1X PBS.

To encapsulate cells within the hydrogel scaffold, cancer and stromal cells maintained in 2D tissue-culture flasks were enzymatically dissociated from the flask surface as previously stated, counted utilizing a hemocytometer with 0.4% Trypan Blue (Lonza, Walkersville, MD), and resuspended in the hydrogel precursor solution at a concentration of 20×10^6 cells/mL at cancer cell to fibroblast ratios of 5:1, 2:1, 1:1, 1:2,

and 1:5. A volume of 10 μL of the cell-laden hydrogel precursor solution was pipetted into each PDMS mold well and photocrosslinked via high-intensity visible light exposure (light intensity: 203 mW/cm^2) for 2 minutes. Upon crosslinking completion, the PDMS mold was carefully peeled back from the well plate surface, thus leaving behind disc-shaped, bioengineered tumor tissues. Appropriate culture media was added to the well plate, which was finally stored in a humidified atmosphere with 5% CO_2 and a constant temperature of 37 ºC; culture media was renewed twice weekly.
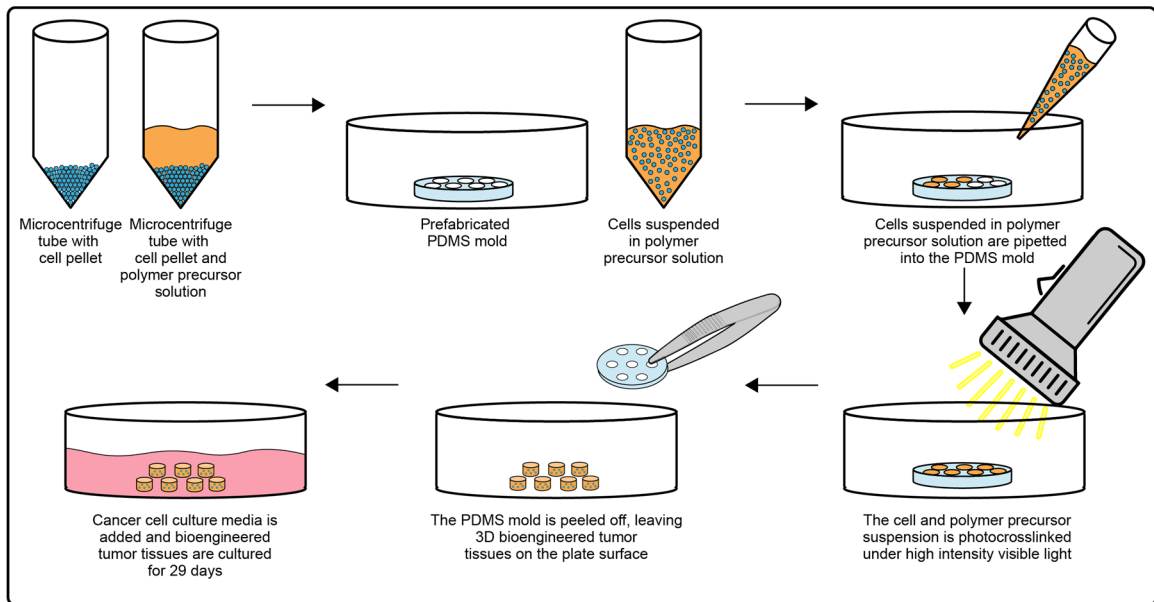
Figure 6: The fabrication progression of 3D bioengineered tumor tissues.

2.2.5. Image Acquisition and Analysis

Phase contrast images of the bioengineered tumor tissues were acquired at several levels of magnification (2X, 10X, 20X) utilizing an inverted Nikon Eclipse Ti microscope fitted with an Andor Luca S camera on culture days 1, 8, 15, 22, and 29, post-encapsulation. The resultant images were analyzed utilizing ImageJ software, version 1.52c (NIH), to quantify both whole hydrogel tissue and individual cell colony physical characteristics.

Regions of interest (ROI) were delineated on the acquired phase contrast images utilizing the ImageJ software capabilities and the tissue or colony area and roundness were subsequently measured and exported to Microsoft Excel.

$$Roundness = \frac{4}{\pi} \times \frac{Area}{(Major\ Axis)^2} \qquad\qquad 1$$

2.2.6. Cell Viability Investigation

Encapsulated cell viability was assessed via fluorescent microscopy through the visualization and quantification of both live and dead cells within the bioengineered tumor tissues. Utilizing the LIVE/DEAD™ (Invitrogen, Carlsbad, CA) mammalian cell cytotoxicity kit, live cells were positively labeled with green-fluorescent Calcein-AM, indicating intracellular esterase activity and an intact plasma membrane. Simultaneously, dead cells were positively labeled with red-fluorescent Ethidium Homodimer-1, indicating the loss of plasma membrane integrity. The bisBenzimide Hoechst 33342 (H33342) (CAT#: 382065, MilliporeSigma, Burlington, MA) fluorochrome was also used to positively label deoxyribonucleic acid (DNA) within all cellular nuclei. It is important to note that the photoinitiator utilized during the encapsulation process auto-fluoresces on the same wavelength as the Calcein-AM live cell stain and thus can interfere with image analysis.

Bioengineered tumor tissues were incubated in the LIVE/DEAD/H33342 stain on days 1 and 15 post-encapsulation for 30 minutes at 25 ºC, washed with 1X PBS, and imaged utilizing an inverted Nikon Eclipse Ti microscope fitted with an Andor Luca S camera. The live cell stain was visualized via the fluorescein isothiocyanate (FITC) filter, the dead cell stain was visualized via the tetramethylrhodamine (TRITC) filter, and the nuclei stain was

visualized via the 4',6-diamidino-2-phenylindole (DAPI) filter. The resultant z-stack images were analyzed with ImageJ software and cellular viability was quantified by manually counting the live and dead cells in each slice of the z-stack.

2.2.7. Immunostaining and Fluorescence Microscopy

The 3D cell morphology and population distribution of cancer and stromal cells within the bioengineered tumor tissues was visualized by immunostaining and confocal fluorescent microscopy on days 1, 15, and 29. Alexa Fluor™ 568 Phalloidin (CAT#: A12380, Thermo Fisher Scientific, Rockford, IL) at a 1:200 dilution in 1X PBS was utilized to positively label F-actin filaments. H33342 at a 1:200 dilution in 1X PBS was utilized to positively label intranuclear DNA. Finally, a Zenon™ Alexa Fluor™ 647 Mouse IgG$_1$ Labeling Kit (CAT#: Z25008, Thermo Fisher Scientific, Rockford, IL) was employed with the anti-fibroblast monoclonal antibody clone TE-7 (CAT#: CBL271, MilliporeSigma, Burlington, MA) at a 1:100 dilution.

In preparation for staining, bioengineered tumor tissues were washed in 1X PBS and fixed overnight at 4 ºC with 4% paraformaldehyde (PFA) (Electron Microscopy Sciences, Hatfield, PA). Encapsulated cells were permeabilized with 0.5% Triton-X for 30 minutes and subsequently blocked via incubation in 0.2 μm filtered blocking buffer (10% FBS and 0.5% bovine serum albumin (BSA) in 1X PBS) for 1 hour at 25 ºC. Bioengineered tumor tissues were then labelled in a Phalloidin/Zenon™ Alexa Fluor™ 647-TE-7 staining solution for a minimum of 1 hour at 25 ºC, rinsed with 1X PBS, again labelled in a H33342 staining solution for a minimum of 1 hour at 25 ºC, and finally rinsed with 1X PBS.

Immunostained bioengineered tumor tissues were mounted on glass coverslips and imaged utilizing confocal microscopy (Nikon AI Confocal Scanning Laser Microscope).

The Phalloidin stain was visualized via the TRITC filter, the H33342 stain was visualized via the DAPI filter, and finally the Zenon™ Alexa Fluor™ 647-TE-7 stain was visualized via the cyanine-5 (CY5HQ) filter. Fluorescent images were analyzed utilizing ImageJ software and ROI were drawn to quantify the area and roundness of each of the cell colonies throughout the z-stacks; calculated values were then exported to Microsoft Excel.

2.2.8. Cell Population Investigation

Flow cytometry was performed by two methods to quantify cell populations within the bioengineered tumor tissues on days 1, 15, and 29 post-encapsulation. In the first method, Zombie Green™ (BioLegend®, San Diego, CA) was utilized to positively label dead cells and cell debris. The Zenon™ Alexa Fluor™ 647 Mouse IgG$_1$ Labeling Kit and anti-fibroblast antibody clone TE-7 at a 1:100 dilution were utilized to positively label BJ-5ta fibroblast cells. Positive and negative controls were performed utilizing PC-3 and BJ-5ta monoculture tumor tissues; additionally, isotype controls were performed utilizing the antibody Mouse IgG$_1$ Isotype Control (MSIgG$_1$) (CAT#: MA110406, Thermo Fisher Scientific, Rockford, IL) with the Zenon™ Alexa Fluor™ 647 Mouse IgG$_1$ Labeling Kit. Unstained single cell suspensions were also analyzed to monitor cell auto-fluorescence as well as auto-fluorescence from the Eosin Y photoinitiator used in the PF photocrosslinking procedure.

Bioengineered tumor tissues were dissociated at 37 ºC utilizing collagenase type IV (CAT#: LS004188, Worthington Biochemical Corporation, Newark, NJ) at a concentration of 1 mg/mL in 1X PBS for 30 minutes, or until completely dissociated. Forced pipetting was also used to aid the degradation of the polymer matrix. The cell suspension solution was centrifuged at 300 g for 5 minutes with the brake off and

resuspended in Accumax (Innovative Cell Technologies, Inc., San Diego, CA) for 15 minutes to yield single-cells. Cells were re-centrifuged, washed with 1X PBS, centrifuged again, and resuspended in Zombie Green™ at a 1:1000 dilution in 1X PBS and incubated at 4 °C in the dark for 30 minutes. Cells were washed with 0.2 μm filtered blocking buffer (10% FBS and 0.5% BSA in 1X PBS), centrifuged, resuspended in blocking buffer, and incubated for 30 minutes at 4 °C in the dark. The Zenon™ Alexa Fluor™ 647-TE-7 or Zenon™ Alexa Fluor™ 647-MSIgG$_1$ extracellular staining solution was subsequently added and followed by another 30-minute incubation at 4 °C in the dark. Stained cells were washed with blocking buffer twice, resuspended in blocking buffer at a concentration of approximately 1×10^6 cells/mL, and finally passed through a 40 μm Flowmi™ Cell Strainer filter.

In the second method, fluorescent PC-3 Red-FLuc-GFP (PerkinElmer, Waltham, MA) cells (were encapsulated with BJ-5ta fibroblasts. Zombie NIR™ (BioLegend®, San Diego, CA) was utilized to positively label dead cells and cell debris. PC-3 Red-FLuc-GFP monoculture tissues were used as a positive control, whereas BJ-5ta monoculture tissues were used as a negative control. Bioengineered tumor tissues were dissociated at 37 °C utilizing collagenase type IV at a concentration of 1 mg/mL in 1X PBS for 30 minutes, or until completely dissociated. The cell suspension solution was centrifuged at 300 g for 5 minutes and resuspended in Accumax to yield single-cells. Cells were re-centrifuged, washed with 1X PBS, centrifuged again, and resuspended in Zombie NIR™ at a 1:100 dilution in 1X PBS and incubated at 4 °C in the dark for 30 minutes. Cell were washed with 1X PBS, centrifuged, resuspended in 1X PBS at a concentration of approximately 1×10^6 cells/mL, and finally passed through a 40 μm Flowmi™ Cell Strainer filter.

The stained cell population was quantified utilizing an Accuri™ C6 (BD Biosciences, Franklin Lakes, NJ) personal flow cytometer according to manufacturer instructions. The analysis was stopped after the incidence of 20,000 events within gating that excluded positively labeled Zombie Green™ or Zombie NIR™ cells, as well as size-excluded small debris and PF particles. Results were analyzed, and event gating was performed utilizing FlowJo® (FlowJo, LLC, Ashland, OR) software.

2.2.9. Matrix Metalloproteinase Secretion Quantification

Serum-free conditioned media was utilized to quantify the levels of MMP-2 and MMP-9 secreted by the bioengineered tumor tissues. To generate the serum-free conditioned media, PC-3 monoculture and fibroblast coculture bioengineered tumor tissues were washed three times with 1X PBS to remove all traces of FBS from the original media and subsequently cultured in PC-3 starvation media (F-12K culture media supplemented with 1% (v/v) Pen-Strep) for 72 hours. Similarly, LNCaP monoculture and fibroblast coculture bioengineered tumor tissues were washed three times with 1X PBS and then cultured in LNCaP starvation media (RPMI-1640 culture media supplemented with 1% (v/v) Pen-Strep) for 72 hours. The conditioned media was then removed, centrifuged for 5 minutes at 400 g, and stored in cryovials at -80 °C until utilized for analysis.

Fluorometric assay experimentation to detect the presence of MMPs in the conditioned media was performed in collaboration with Dr. Tareq Anani and Dr. Allan David (Department of Chemical Engineering, Auburn University). The specific fluorogenic resonance energy transfer (FRET) peptide substrate, 390 MMP FRET substrate III (Mca-PLA-Nva-Dpa-AR-NH2) (CAT#: AS-27090, AnaSpec, Inc., Fremont, CA) was employed to positively indicate MMP-2, -7, -9, or -13 activity. Conditioned media samples

were analyzed in the presence of 4-Aminophenylmercuric acetate (APMA) to activate pro-MMP, as well as without APMA to detect naturally active MMP activity.

To begin, APMA powder was dissolved in dimethyl sulfoxide (DMSO) at a concentration of 10 mg/mL, or at a molarity of 28.43 mM. This solution was then further diluted to a molarity of 3 mM through the addition of buffer (50 mM TRIS hydrochloride (TRIS-HCL) (AMRESCO, Inc., Solon, OH), pH 7.5, 150 mM sodium chloride (NaCl) (AMRESCO, Inc., Solon, OH), 10 mM calcium chloride ($CaCl_2$) (AMRESCO, Inc., Solon, OH), and 0.05% Brij-35 (Spectrum Chemical, New Brunswick, NJ)). Conditioned media samples were mixed at a 1:1 ratio with buffer (50mM TRIS-HCL, pH 7.5, 150 mM NaCl, 10mM $CaCl_2$, and 0.05% Brij-35) in duplicates; 3 mM APMA pro-MMP activating solution was added to one replicate of each of the *in vitro* samples. Standard samples were run as positive controls and were comprised of recombinant, human pro-MMP-2 (CAT#: AS-72005, AnaSpec, Inc., Fremont, CA) at 10 μg/mL with fresh PC-3 or LNCaP starvation media mixed at a 1:1 ratio with buffer, as previously defined, with 3mM APMA solution. Final molarities of 0.027, 0.067, 0.13, 0.27, 0.6, and 1.23 nM MMP-2 were employed to generate standard curves. Negative controls were comprised of duplicates of fresh PC-3 or LNCaP starvation media mixed at a 1:1 ratio with buffer, as previously defined, with half containing 3 mM APMA solution.

In vitro samples, positive control standards, and negative controls were loaded onto a 96-well plate, covered with aluminum foil to reduce evaporation as much as possible, and incubated at 37 °C for 2 hours. Immediately before the incubation period ended, the 7.5 μM 390 MMP FRET peptide Substrate III solution was prepared by mixing fresh PC-3 or LNCaP starvation media with 3 mM 390 MMP FRET peptide Substrate III in DMSO.

At the end of the 2-hour incubation period, the peptide was added to the wells and the fluorescence signal was measured with a plate reader at Ex/Em 325/393 nm for 2.5 hours at intervals of 3 minutes. Subsequent fluorescence signal values were corrected utilizing the appropriate negative control to negate background fluorescence.

2.2.10. Mechanical Stiffness Quantification

The mechanical stiffness of the bioengineered tumor tissues was quantified on days 1, 8, 15, 22, and 29 post-encapsulation via parallel plate compression testing under physiological conditions through the use of a MicroSquisher (CellScale, Waterloo, ON, CA) apparatus according to manufacturer instructions. Samples were loaded onto a stage at the front of a fluid bath test chamber filled with 1X PBS and held at 37 ºC. A 558.8 μm diameter tungsten wire microcantilever beam fitted with a compression platen was affixed to the vertical piezo motor driven actuator at a 90º angle and positioned at the top of the sample. Bioengineered tumor tissues were compressed to a minimum 15% deformation at a maximum compression rate of 10 μm/s for three cycles. The force applied to the sample was calculated via deflection of the microcantilever beam with a typical force resolution of 34.52 μN; tissue displacement was tracked with the MicroSquisher system camera and analyzed utilizing ImageJ software. Force versus displacement data was gathered and exported to a custom Microsoft Excel macro to create a compressive stress (σ) versus strain (ε) curve; the linear portion slope of which yielded the Young's modulus of the sample. All samples were tested in triplicates.

$$Deflection = \frac{Force \times (Beam\ Length)^3}{3 \times Beam\ Modulus \times Beam\ Area\ Moment\ of\ Inertia} \qquad 2$$

$$Beam\ Area\ Moment\ of\ Inertia = \frac{\pi \times radius^4}{4} \qquad 3$$

$$\sigma_{compressive} = \frac{Force}{Compression\ Area} \qquad\qquad 4$$

$$\varepsilon_{compressive} = \frac{\Delta\ Tissue\ Height}{Initial\ Tissue\ Height} \qquad\qquad 5$$

$$Young's\ modulus = \frac{\sigma_{compressive}}{\varepsilon_{compressive}} \qquad\qquad 6$$

2.2.11. Statistical Analysis

Statistical analysis was performed utilizing Minitab 18 Statistical Software (Minitab Inc., State College, PA). One-way analysis of variance (ANOVA) with Tukey's family error rate of 0.5% was used to evaluate the statistical significance between multiple groups. If the variance was unequal between groups, the Games-Howell post-hoc test was subsequently performed. All values presented are mean ± standard deviation (SD).

2.3. Results and Discussion

2.3.1. Cell Viability, Colonization, and Migration in 3D Culture

PC-3 metastatic prostate cancer cells were successfully encapsulated in PF hydrogels at a concentration of 20×10^6 cells/mL in coculture with BJ-5ta stromal fibroblasts at cancer cell to fibroblast ratios of 5:1, 2:1, 1:1, 1:2, 1:5, as well as in single cell type monocultures. The bioengineered tumor tissues were maintained for a period of 29 days and temporal variations in encapsulated cell behavior were analyzed in weekly increments. To validate the PF hydrogel model as a viable scaffold for PC-3 and BJ-5ta cell adhesion, proliferation, colonization, and migration *in vitro*, multi-magnification phase contrast imaging and cell viability assays were performed. Figures 7 through 11 present 2X and 20X magnification phase contrast images on days 1, 15, and 29 post-encapsulation.

It can be seen that bioengineered tumor tissues with a higher number of PC-3 cancer cells presented increased colonization at, and migration to, the edge of the hydrogel with increasing culture time. This phenomenon can be attributed to the culture media gradient induced by the crosslinked matrix throughout the hydrogel, in which more nutrients are available near the circular edge of the bioengineered tumor tissues. Furthermore, tissues comprised of a 5:1 PC-3 to BJ-5ta cell ratio were characterized by increased degradation of the polymer matrix, as evidenced by the loss of structural integrity leading up to day 29 post-encapsulation in regions exhibiting more prominent cell colonization and proliferation. Conversely, as the encapsulated fibroblast cell ratio increases, increasingly limited cell migration was noted, and over time, a portion of cells appeared to evacuate the PF scaffold and adhere to the tissue culture flask surface.

As shown in Figure 12, quantification of changes in cell colony area over time verified the observation of an increased range of colony sizes in tissues with higher numbers of PC-3 cancer cells, however, the average colony size in these tissues peaked around day 15 post-encapsulation. Interestingly, the 1:1 cancer cell to fibroblast cell ratio bioengineered tumor tissues demonstrated little to no change in colony area over time. As expected, a narrow range of cell colony areas was noted at all time points, in addition to a decrease in colony size over increasing culture time in BJ-5ta monoculture hydrogels. This is likely due to the inherent nature of fibroblasts to elongate along the surface upon which they are cultured. As a result, they do not colonize in the same sense that cancer cells do.
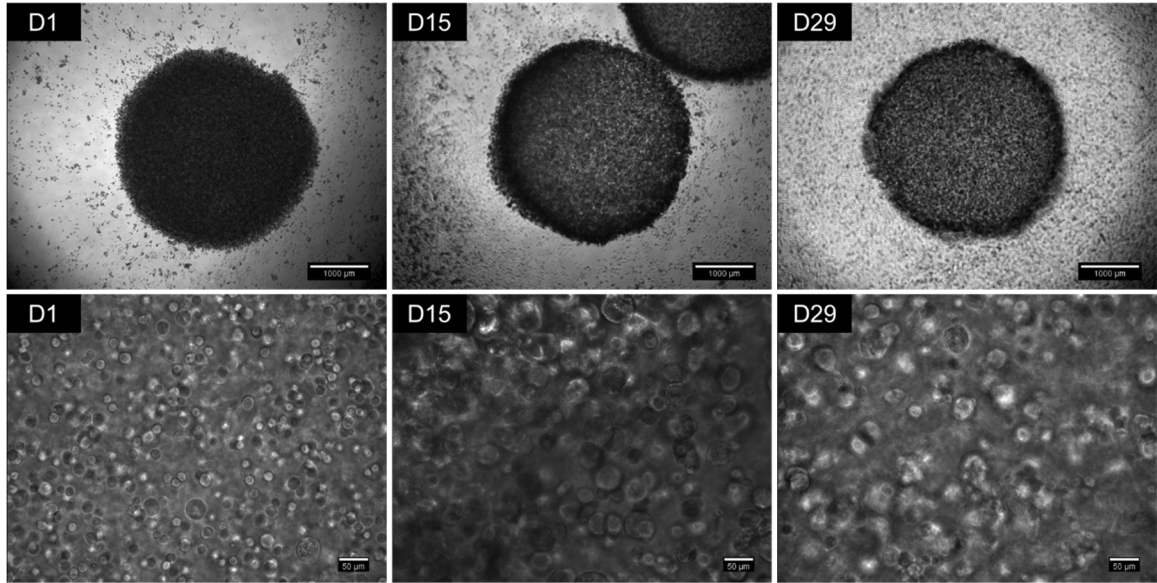
Figure 7: Phase contrast images of PC-3 monoculture bioengineered tumor tissues over 29 days of culture. *Cells are shown to proliferate, migrate, and colonize throughout the PF matrix in 2X images (top row) with a slight preference to the edge of the hydrogel, as evidenced by the formation of a dark ring of larger colonies encircling the tissue at later time points. Furthermore, 20X images (bottom row) illustrate an increase in colony size from day 1 to day 15 post-encapsulation. (2X scale bars = 1000 μm, 20X scale bars = 50 μm)*
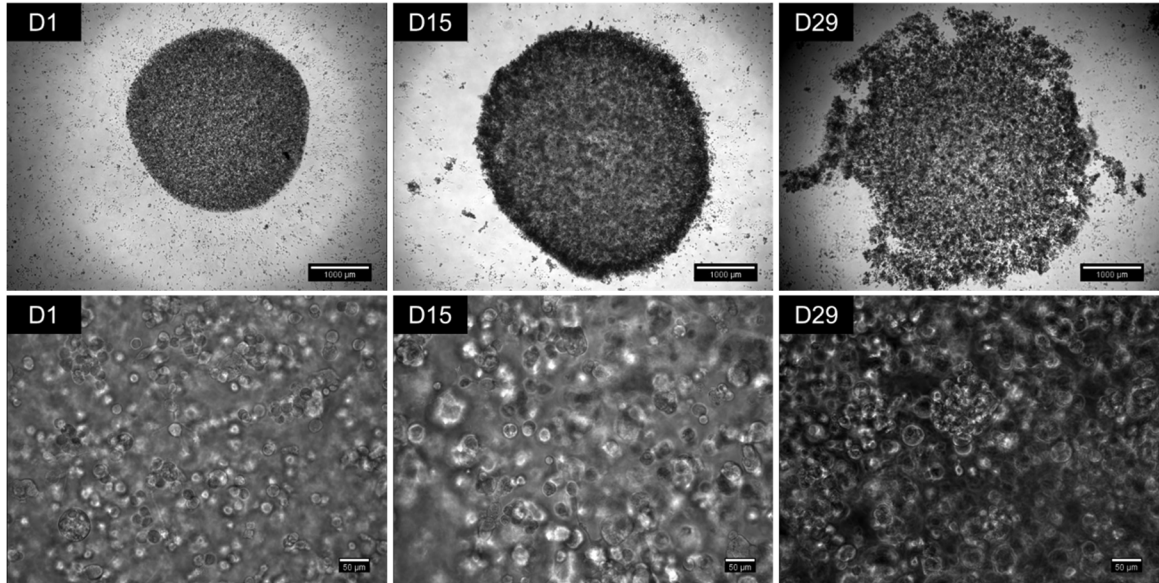
Figure 8: Phase contrast images of 5:1 PC-3 to BJ-5ta cell ratio coculture bioengineered tumor tissues over 29 days of culture. *Cells are shown to proliferate, migrate, and colonize throughout the PF matrix in 2X images (top row) with a slight preference to the edge of the hydrogel, as evidenced by the formation of a dark ring of larger colonies encircling the tissue on day 15. Increased degradation of the PF scaffold is noted on day 29, likely as a result of larger and more proliferative colonies present at the edge of the tissue. Furthermore, 20X images (bottom row) illustrate an increase in colony size from day 1 to day 29 post-encapsulation. (2X scale bars = 1000 μm, 20X scale bars = 50 μm)*

Figure 9: Phase contrast images of 1:1 PC-3 to BJ-5ta cell ratio coculture bioengineered tumor tissues over 29 days of culture. *Cells are shown to proliferate in 2X images (top row) within the PF matrix with only a slight increase in colonization towards the edge of the hydrogel on day 15. Furthermore, 20X images (bottom row) illustrate similar cell colony sizes throughout long-term culture post-encapsulation. (2X scale bars = 1000 μm, 20X scale bars = 50 μm)*
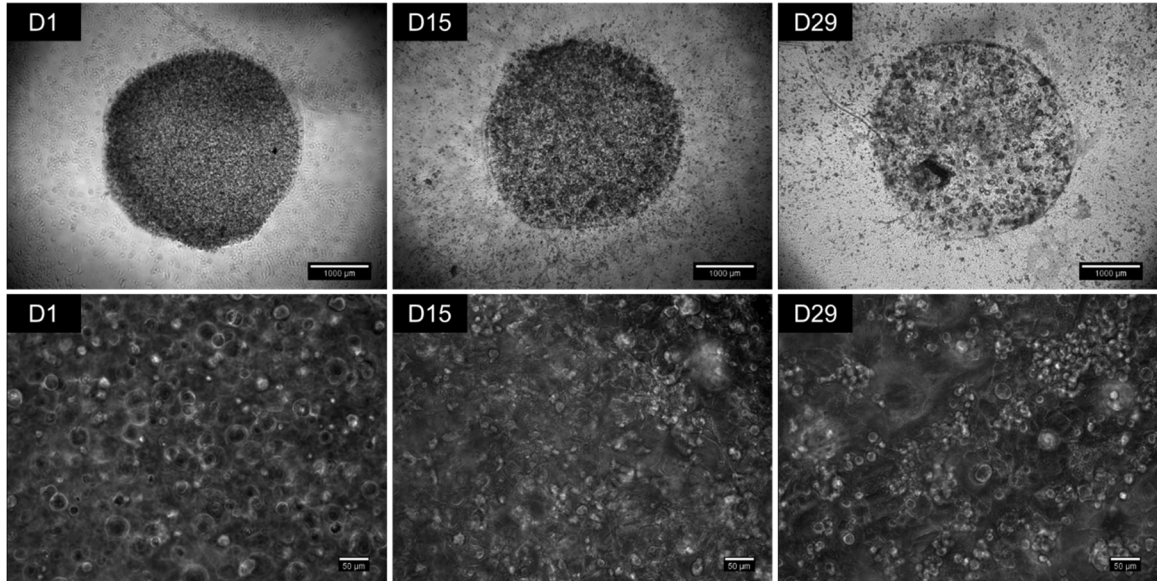
Figure 10: Phase contrast images of 1:5 PC-3 to BJ-5ta cell ratio coculture bioengineered tumor tissues over 29 days of culture. *Cells are shown to colonize in 2X images (top row) on day 15 post-encapsulation, however, become more isolated with increasing culture time. From these images it appears likely that the circular, dark colonies seen consist primarily of the PC-3 cells, which provides a reasonable explanation for their scarcity. Furthermore, 20X images (bottom row) illustrate visible elongation of fibroblast cells on both days 15 and 29 post encapsulation. (2X scale bars = 1000 μm, 20X scale bars = 50 μm)*
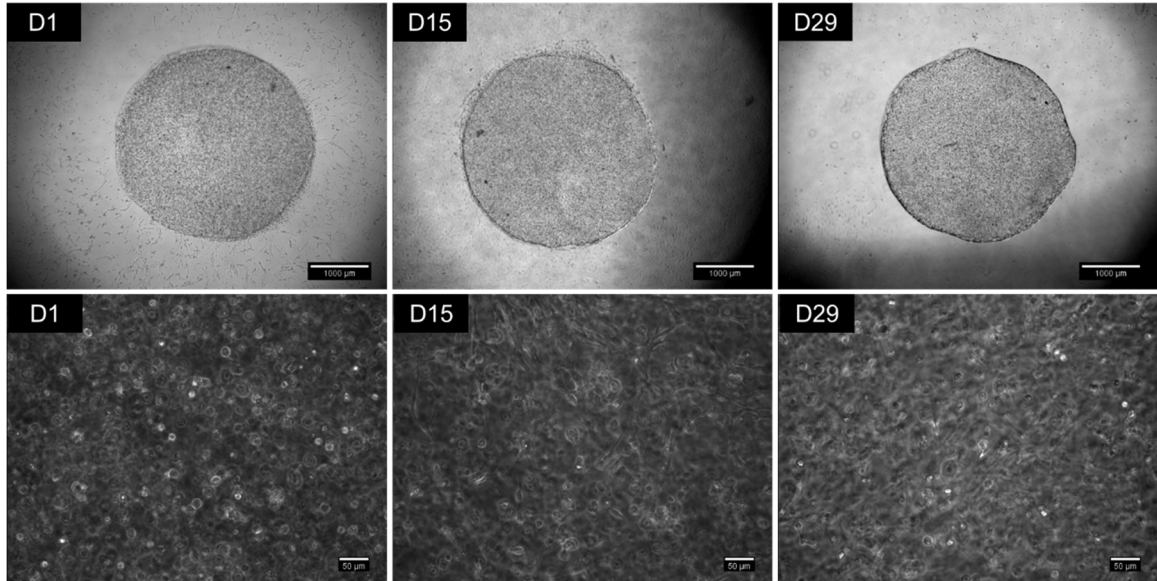
Figure 11: Phase contrast images of BJ-5ta monoculture bioengineered tumor tissues over 29 days of culture. *2X images (top row) present little to no change in the appearance or colonization within the PF matrix over increasing culture time. However, 20X images (bottom row) illustrate the adhesion to and elongation of fibroblasts along the biomaterial scaffold on day 15 post-encapsulation. Some elongation is also shown on day 29, however, the fibroblast networks appear to have diminished between the two final time points. (2X scale bars = 1000 μm, 20X scale bars = 50 μm)*
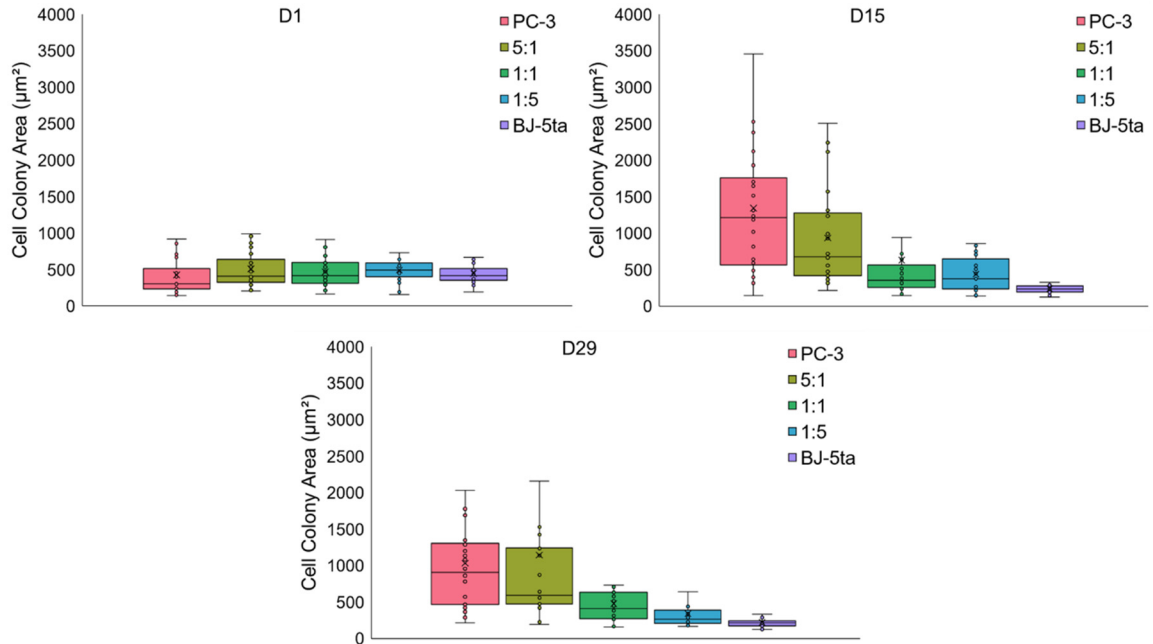
Figure 12: The range of colony areas observed in bioengineered tumor tissues over time. *Bioengineered tumor tissues with a larger number of encapsulated PC-3 cells demonstrated the widest range of colony sizes, in addition to the largest colony sizes. The 1:1 ratio hydrogels were not found to yield significant changes in colony size over time. As expected, BJ-5ta monoculture tissues presented the smallest colony sizes and decreased over time. Box and whisker plots illustrate the distribution of collected values, emphasizing the mean, median, upper and lower quartiles, and highest and lowest observations. (n = 25 colonies per bioengineered tumor tissue type per time point)*

To further investigate encapsulated cell behavior on a macroscale, changes in bioengineered tumor tissue area over time were quantified and are displayed in Figure 13. Only slight changes were noted for each tissue type, however, as expected PC-3 monoculture tissues increased over time due to cell colony outgrowths, 5:1 cancer cell to

fibroblast ratio coculture tissues increased until day 15 and decreased leading to day 29 due to increased degradation of the polymer matrix, and finally BJ-5ta monoculture tissues slightly decreased over time and presented the narrowest size distribution. Overall, the most significant changes in the bioengineered tumor tissue structure occurred on a cellular level as the encapsulated cells remodel their microenvironment over time, form important cell-cell junctions, and produce an extracellular matrix.
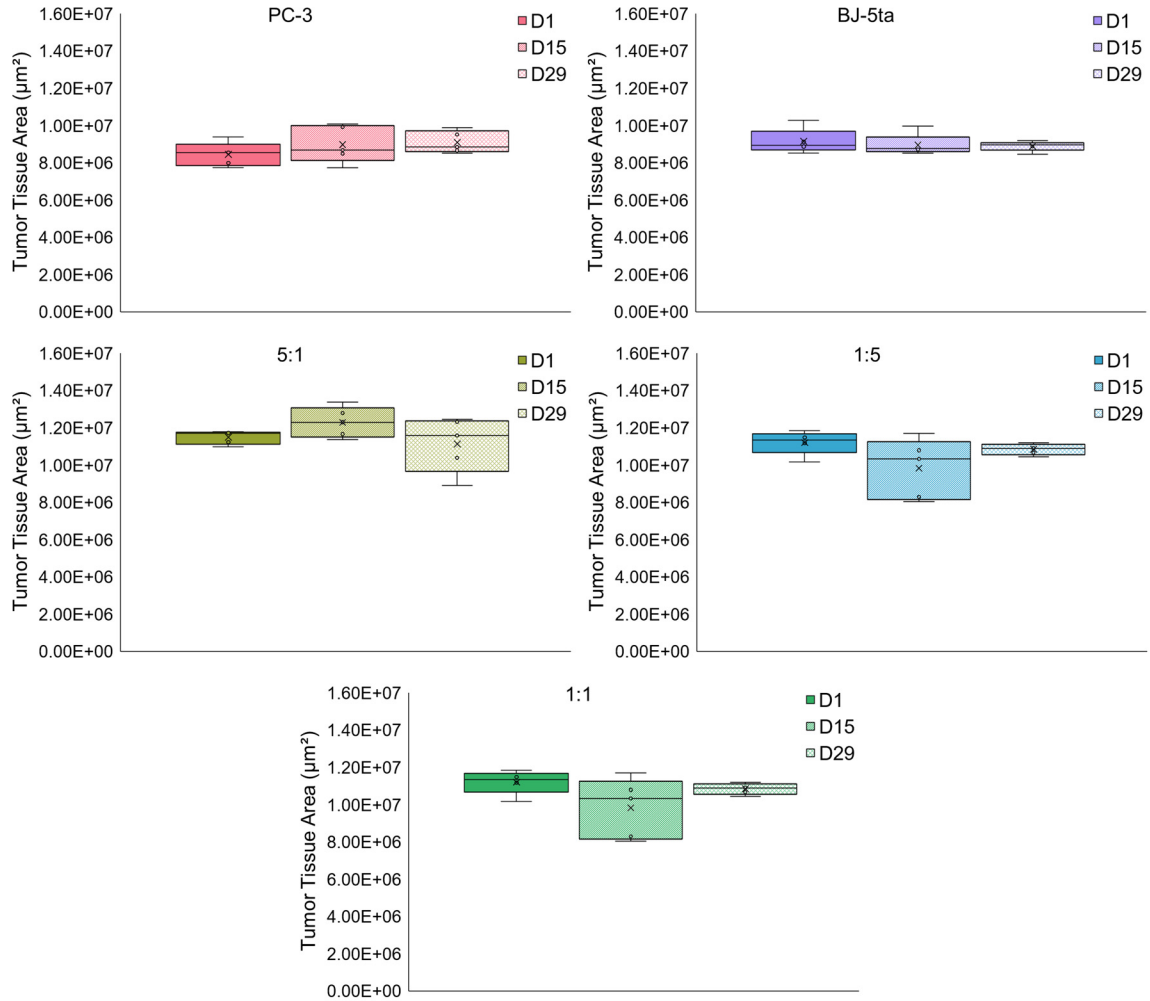
Figure 13: Variations in bioengineered tumor tissue area over time in all mono- and cocultures. *As expected, no extreme variations are noted, regardless of encapsulated cell type and ratio. Box and whisker plots illustrate the distribution of collected values, emphasizing the mean, median, upper and lower quartiles, and highest and lowest observations. (n = 5 hydrogels per time point per bioengineered tumor tissue type)*

Cellular viability was also assessed to determine if the PC-3 and BJ-5ta cells were able to not only survive the encapsulation process, but also remain viable within the PF matrix over time. Figures 14 through 17 present fluorescence microscopy images on days 1 and 15 post-encapsulation. Calcein-AM is shown in green and positively labels live cells, Ethidium homodimer-1 is shown in red and positively labels dead cells, and finally H33342 is shown in blue and positively labels intranuclear double stranded DNA. Limited cell death is observed in all cell ratios at all time points, with no locational variations or non-uniform viability. However, it is noted that cell death does appear to increase with increasing number of fibroblasts, thus indicating that BJ-5ta fibroblasts may not survive within the bioengineered tumor tissues as well as PC-3 cancer cells do.

Quantification of cell viability, shown in Figure 18, revealed that over 75% of cells remain viable within the bioengineered tumor tissues regardless of encapsulated cell ratio or culture duration. This result confirms that PF is an appropriate scaffold for the 3D *in vitro* coculture of PC-3 and BJ-5ta cells, in regard to cell viability. It was confirmed that on day 1 post-encapsulation that hydrogels with a higher number of PC-3 prostate cancer cells did present a higher overall percentage of live cells. Interestingly, the 1:5 cancer cell to fibroblast ratio bioengineered tumor tissues were the only hydrogels to present a higher overall viability on day 15 compared to day 1.
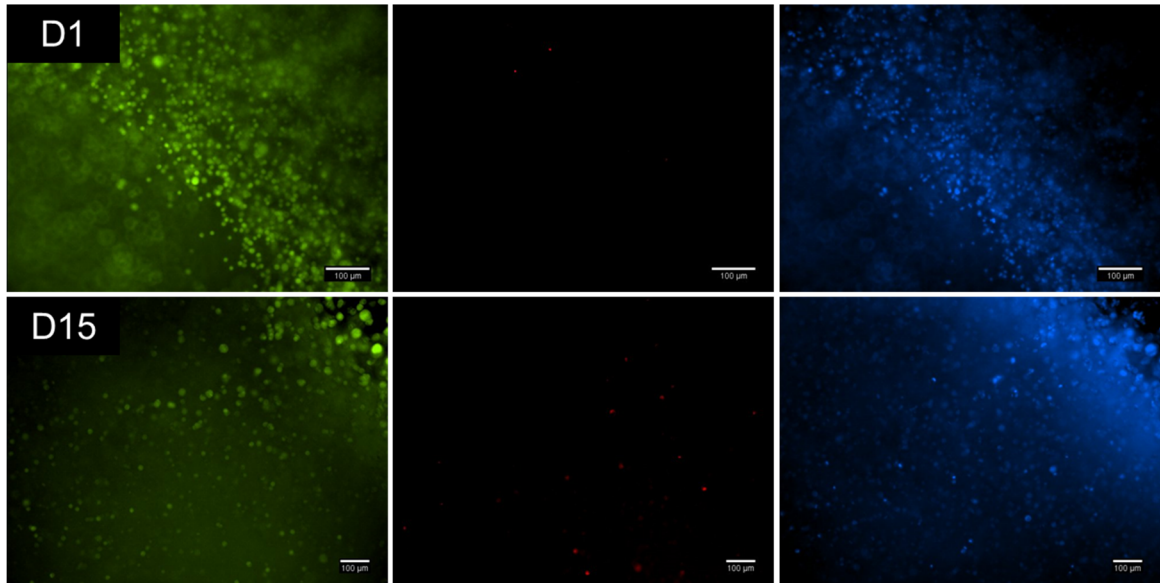
Figure 14: Fluorescence microscopy images illustrating cell viability in PC-3 monoculture bioengineered tumor tissues on days 1 and 15 post-encapsulation. *Extremely limited cell death was observed at both time points. It is important to note that the hydrogels were situated at an angle during imaging, so only a small number of cells can be in focus at one time, thus resulting in the "blurry" regions of the images shown above. Live cells are shown in green, dead cells are shown in red, and intranuclear double stranded DNA is shown in blue; images were taken at 10X magnification. (10X scale bars = 100 μm)*
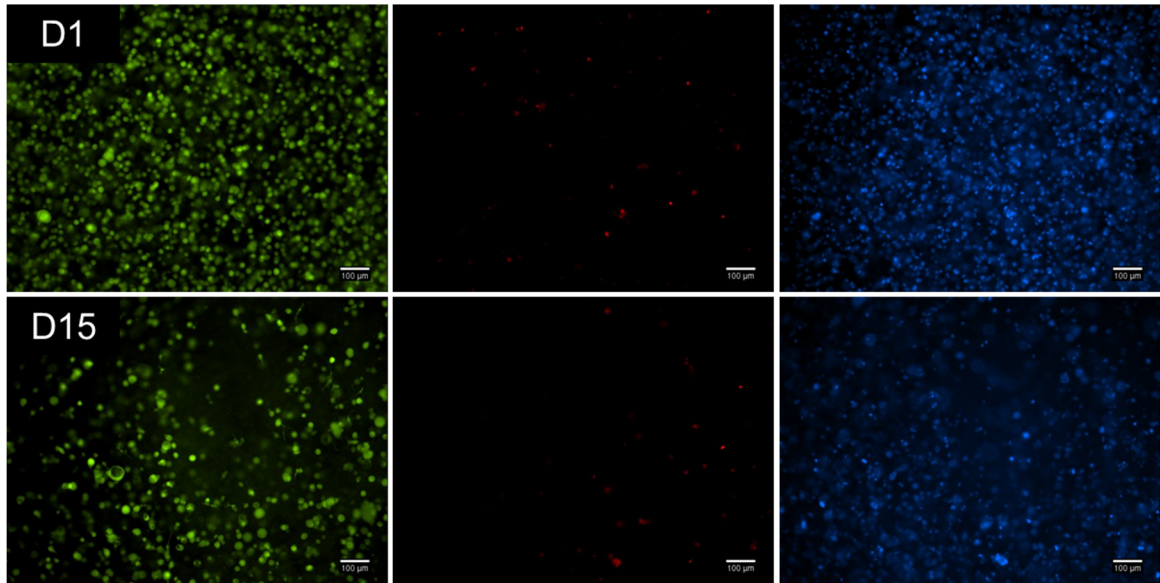
Figure 15: Fluorescence microscopy images illustrating cell viability in 5:1 PC-3 to BJ-5ta bioengineered tumor tissues on days 1 and 15 post-encapsulation. *Very limited cell death was observed at both time points. Live cells are shown in green, dead cells are shown in red, and intranuclear double stranded DNA is shown in blue; images were taken at 10X magnification. (10X scale bars = 100 μm)*
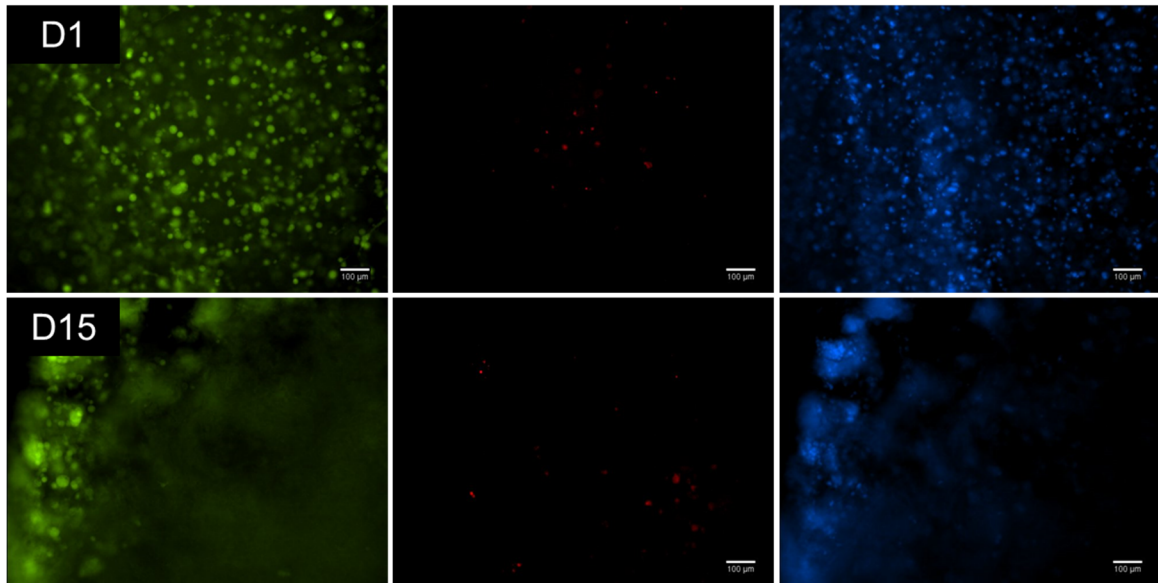
Figure 16: Fluorescence microscopy images illustrating cell viability in 1:1 PC-3 to BJ-5ta bioengineered tumor tissues on days 1 and 15 post-encapsulation. *Limited cell death was observed at both time points. It is important to note that the day 15 hydrogel was situated at an angle during imaging, so only a small number of cells can be in focus at one time, thus resulting in the "blurry" regions of the images shown above. Live cells are shown in green, dead cells are shown in red, and intranuclear double stranded DNA is shown in blue; images were taken at 10X magnification. (10X scale bars = 100 μm)*
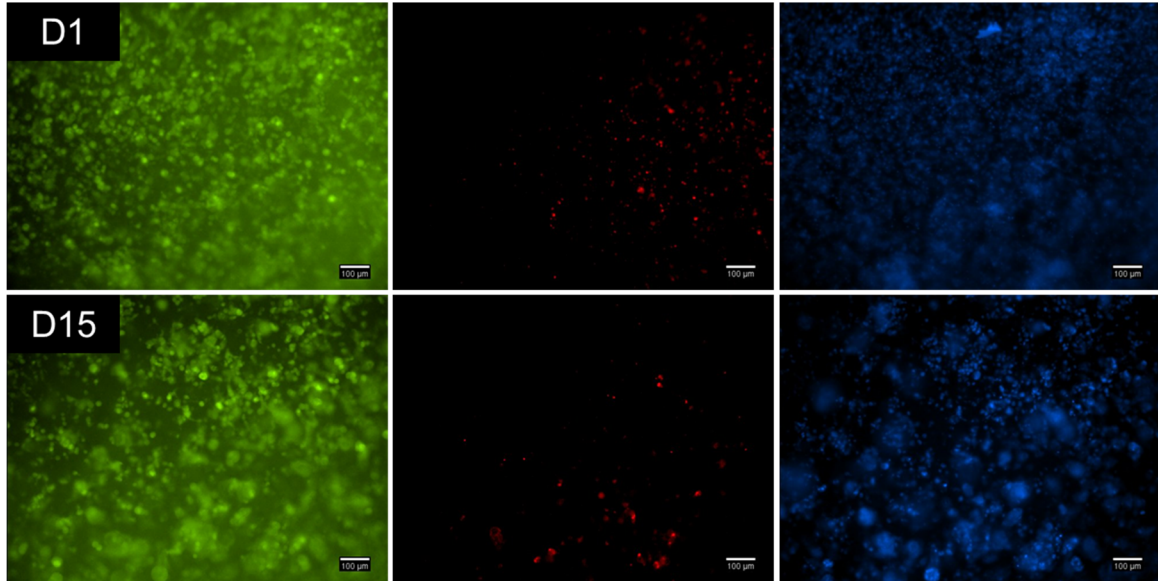
Figure 17: Fluorescence microscopy images illustrating cell viability in 1:5 PC-3 to BJ-5ta bioengineered tumor tissues on days 1 and 15 post-encapsulation. *A larger amount of cell death was noted at both time points in the 1:5 ratio hydrogels than observed in other cell ratio hydrogels, however, the large majority of the cells remained viable. It is important to note that the fluorescence signal from the Calcein-AM stain was also not as strong as shown in Figures 14 through 16, and thus some background fluorescence from Eosin Y was inevitable on the live stain images. Live cells are shown in green, dead cells are shown in red, and intranuclear double stranded DNA is shown in blue; images were taken at 10X magnification. (10X scale bars = 100 μm)*
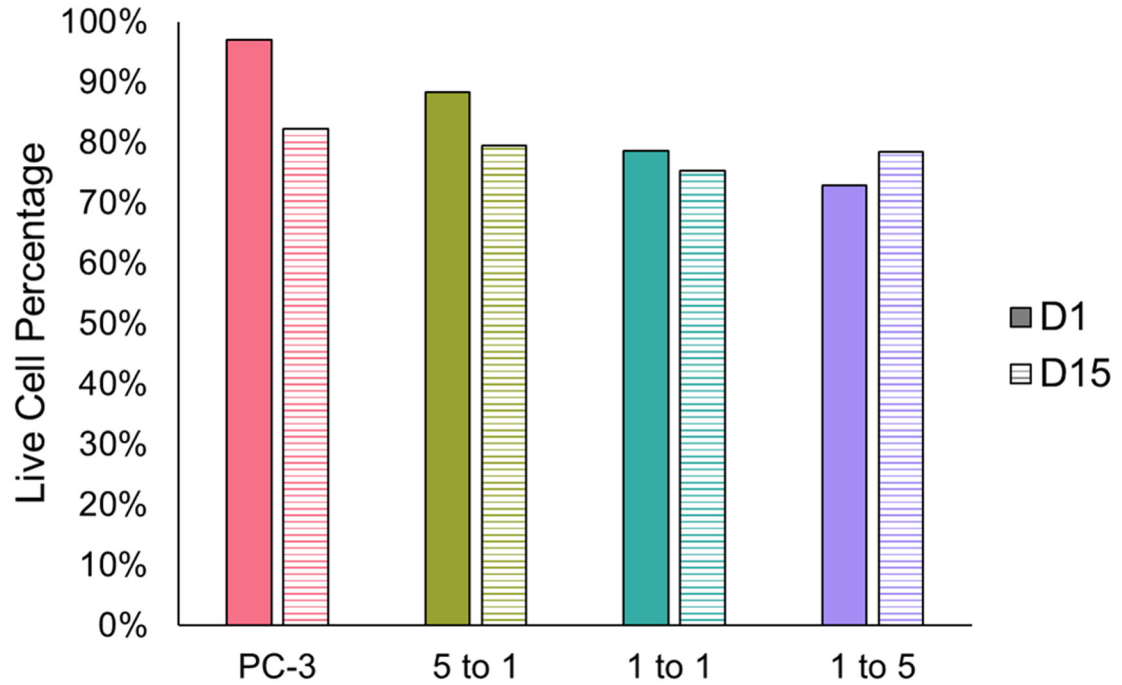
Figure 18: Quantification of cell viability within PC-3 and BJ-5ta coculture bioengineered tumor tissues on days 1 and 15 post-encapsulation. *The percentage of live cells remained greater than 75% within PC-3 monoculture and 5:1, 1:1, and 1:5 PC-3 to BJ-5ta coculture bioengineered tumor tissues, regardless of time point. Hydrogels comprised of a larger number of PC-3 cells were shown to have greater cell viability immediately following the encapsulation process than do those with a larger number of BJ-5ta cells.*

2.3.2. Cell Morphology in 3D Culture

To characterize the encapsulated cell morphology within the bioengineered tumor tissue PF matrix, immunostaining and confocal microscopy experiments were performed. Phalloidin was utilized to visualize f-actin filaments in the cytoskeleton and is shown in red, H33342 was utilized to visualize intranuclear double stranded DNA and is shown in blue, and finally TE-7 was utilized to positively label fibroblasts and is shown in green. Figure 19 presents the resultant 10X magnification images for PC-3 monoculture, and 5:1, 1:1, and 1:5 PC-3 to BJ-5ta coculture bioengineered tumor tissues on day 15 post-encapsulation.

PC-3 cells and cell colonies were found to range in size yet are shown to demonstrate appropriate circular morphology, in addition to uniform distribution throughout the PF bioengineered tumor tissue. As expected, there appeared to be a large amount of intranuclear DNA present (stained in blue) relative to f-actin filaments (stained in red) due to the near-triploid characteristic of PC-3 cells.

As fibroblasts were introduced to the model in a 5:1 cancer cell to fibroblast ratio, cells and cell colonies were shown to remain mostly circular in shape, however, did not form large colonies similar to the PC-3 monoculture hydrogel. This is consistent with the quantification and range of colony sizes collected from phase contrast imaging, as presented in Figure 12. BJ-5ta fibroblasts were shown to be uniformly distributed throughout the 5:1 ratio hydrogel, however, no noticeable elongation or significant interaction with PC-3 cells was observed.

Surprisingly, the 1:1 PC-3 to BJ-5ta cell ratio bioengineered tumor tissue presented larger, yet still circular, PC-3 cell colonies than the 5:1 ratio, contrary to what was observed

through phase contrast imaging. Again, BJ-5ta fibroblasts were shown to be evenly distributed throughout the tumor tissues. However, unlike the 5:1 ratio hydrogel, the fibroblasts began to exhibit an elongated morphology, in addition to slight interaction with the PC-3 cell colonies. It is important to note that the cells and cell colonies in the 1:1 cell ratio bioengineered tumor tissues appeared to be fairly isolated with acellular regions of PF matrix existing between colonies.

Conversely, the 1:5 PC-3 to BJ-5ta bioengineered tumor tissues were observed to exhibit significant cancer cell-fibroblast interaction with extensive networks of elongated fibroblasts and circular cancer cell colonies. Both cell types were found to be evenly distributed throughout the PF matrix, and as expected, f-actin filaments appeared to be present in an equal or larger quantity than the intranuclear DNA.

Image analysis was utilized to quantify the roundness of the cell colonies present in each of the bioengineered tumor tissue types. As shown in Figure 20, values were further evaluated through the implementation of a Python function to generate violin plots illustrating the range and frequency of roundness observed, where a value of 1 indicates a perfectly circular colony. As expected, bioengineered tumor tissues with a larger number of PC-3 cancer cells exhibited a larger number of round colonies with a narrower distribution. Consequently, those comprised of an increased ratio of fibroblasts yielded a wide range of roundness values.
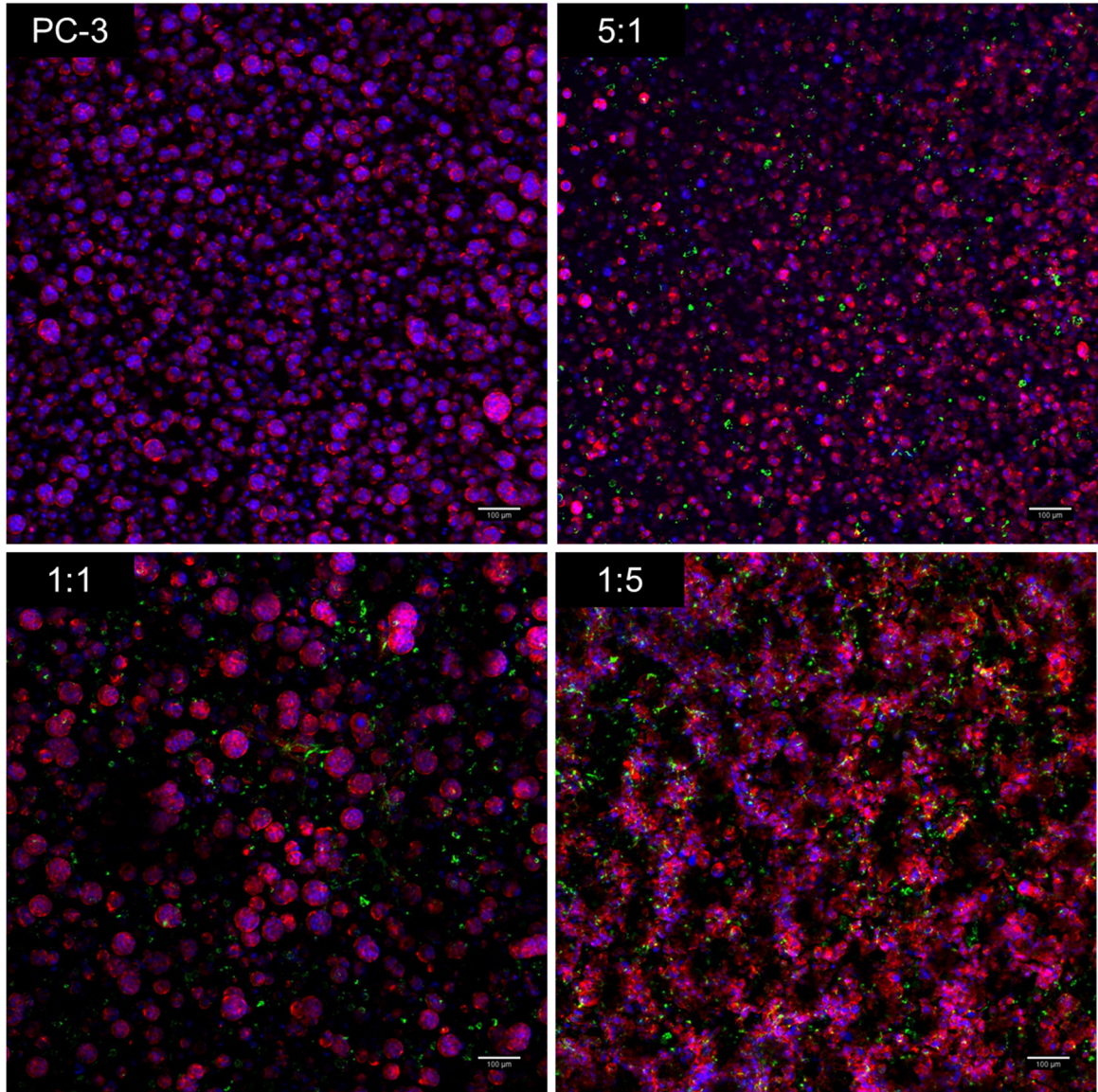
Figure 19: Confocal microscopy images of immunostained bioengineered tumor tissues on day 15 post-encapsulation. *Confocal images portrayed the effect of the encapsulated cell type ratio on 3D cell morphology, distribution, and interaction in vitro. BJ-5ta fibroblasts are illustrated in green, f-actin filaments are illustrated in red, and intranuclear double stranded DNA is illustrated in blue. (10X scale bars = 100 μm)*
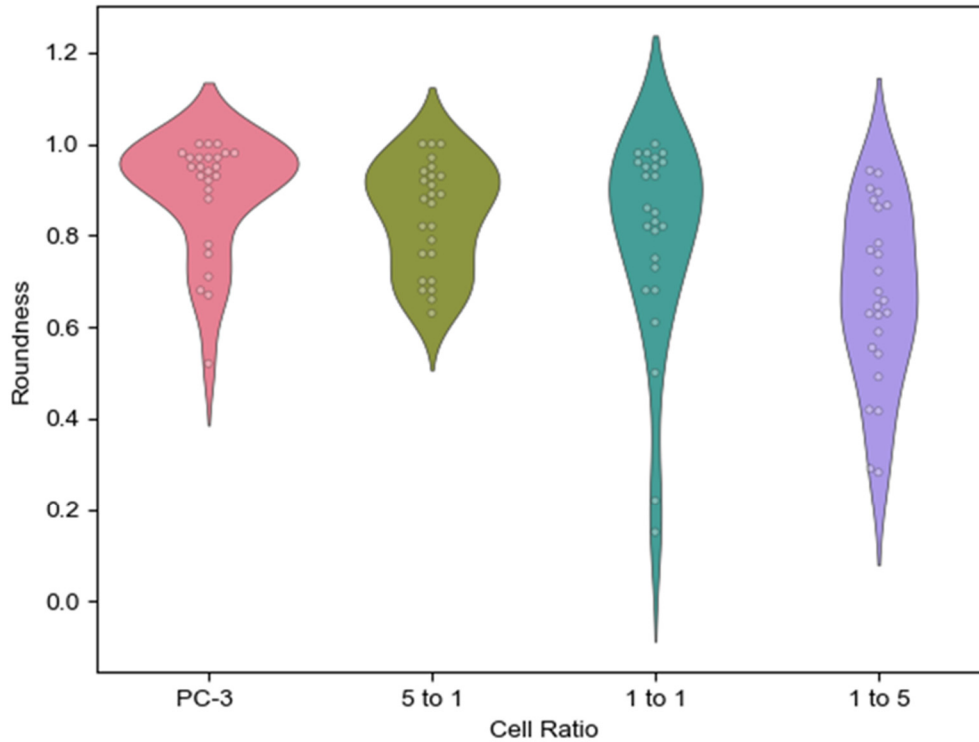
Figure 20: The range and frequency of colony roundness observed within bioengineered tumor tissues. *Bioengineered tumor tissues comprised of a larger number of PC-3 prostate cancer cells yielded more round colonies, whereas, those with an increased number of BJ-5ta fibroblasts produced a wider range of slightly or severely elongated colonies. Violin plots illustrate the both the range and frequency of the multimodal roundness data collected. (n = 25 colonies per bioengineered tumor tissue type; Roundness = 1 indicates a perfectly circular morphology)*

Through analysis of confocal microscopy images, it was found that not only does cell morphology differ between bioengineered tumor tissues of varying encapsulated cell types and ratios, but also spatially within a single hydrogel. As illustrated in Figure 21, BJ-5ta fibroblasts were found to substantially elongate along the linear top surface of the

bioengineered tumor tissue, while PC-3 prostate cancer cells maintained a circular morphology. As expected, little to no elongation was observed near the center of the hydrogel as the PF scaffold is not patterned, and thus is not known to provide a strictly linear matrix for the cells to adhere to.
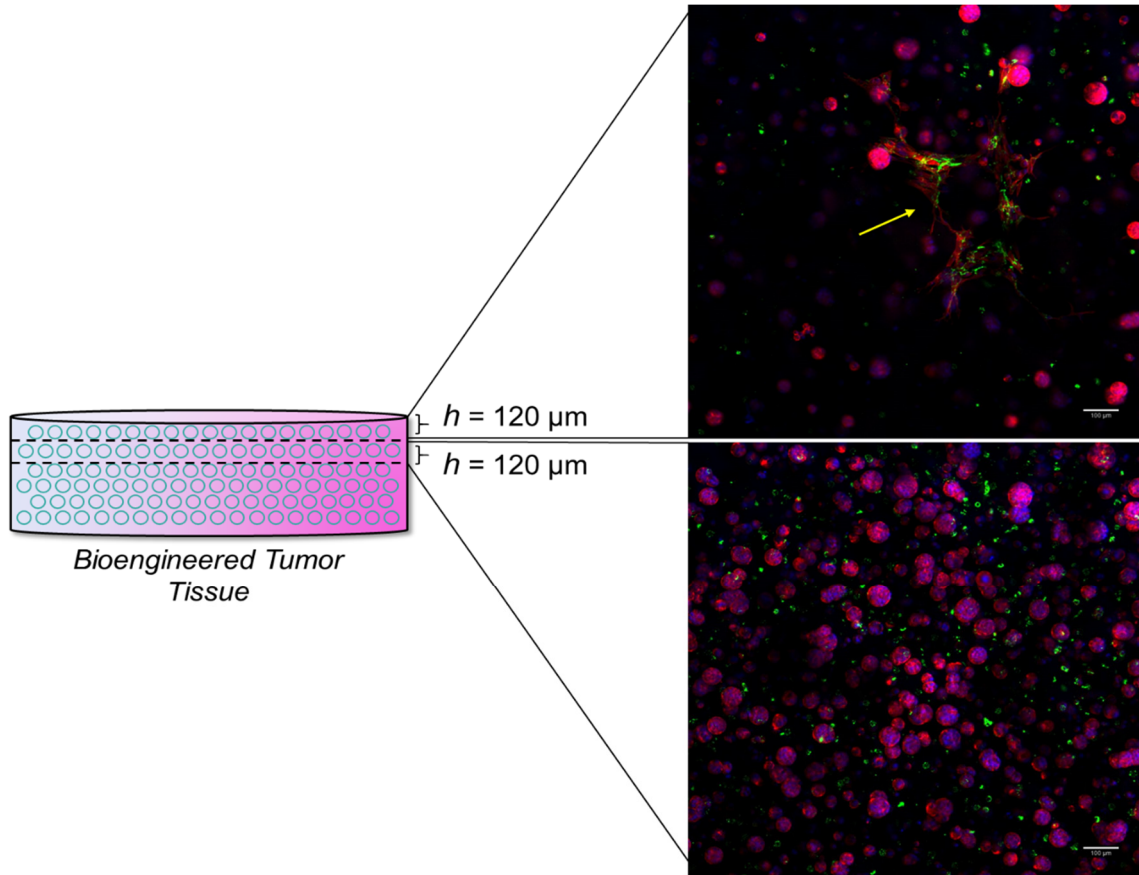
Figure 21: Spatial heterogeneity of encapsulated cell morphology in bioengineered tumor tissues. *Fibroblasts were found to elongate only along the linear top of the hydrogel (yellow arrow), while cancer cells maintained a circular morphology. BJ-5ta fibroblasts are illustrated in green, f-actin filaments are illustrated in red, and intranuclear double stranded DNA is illustrated in blue. (10X scale bars = 100 μm)*

2.3.3. Temporal Variations in Encapsulated Cell Populations

To quantify variations in the encapsulated cell population over increasing culture time, as well as to verify the initial cell ratio, flow cytometry experiments were performed. The anti-fibroblast marker, TE-7, was employed to positively label BJ-5ta fibroblasts, while PC-3 cancer cells were left unstained. This decision was largely due to the difficulty in finding an immunolabel that would positively mark the cancer cells, while simultaneously refraining from labeling the fibroblast cells. It is important to note that the TE-7 antibody was not found to positively label all fibroblasts; as a result, cell populations are presented as TE-7 positive populations, which are all fibroblasts, and TE-7 negative populations, which are possibly a mixture of primarily cancer cells with some fibroblasts. Zombie Green™ was also employed to positively label dead cells and cell debris to ensure that the reported cell percentage included only live cells. This label presented the advantage of fluorescing at the same wavelength as the Eosin Y utilized during the encapsulation process, and thus any hydrogel fragments remaining after enzymatic dissociation of the bioengineered tumor tissues did not affect the reported cell population percentages.

As presented in Figure 22, the 5:1 PC-3 to BJ-5ta cell ratio bioengineered tumor tissues presented a cell ratio very close to the intended proportion with a very small standard deviation on day 1 post-encapsulation. Surprisingly, as culture time progressed, fibroblasts were found to proliferate at a higher rate than the prostate cancer cells, as evidenced by the approximately equal percentage of TE-7 positive cells and TE-7 negative cells on day 15. This trend, however, was not maintained leading up to day 29 of coculture.
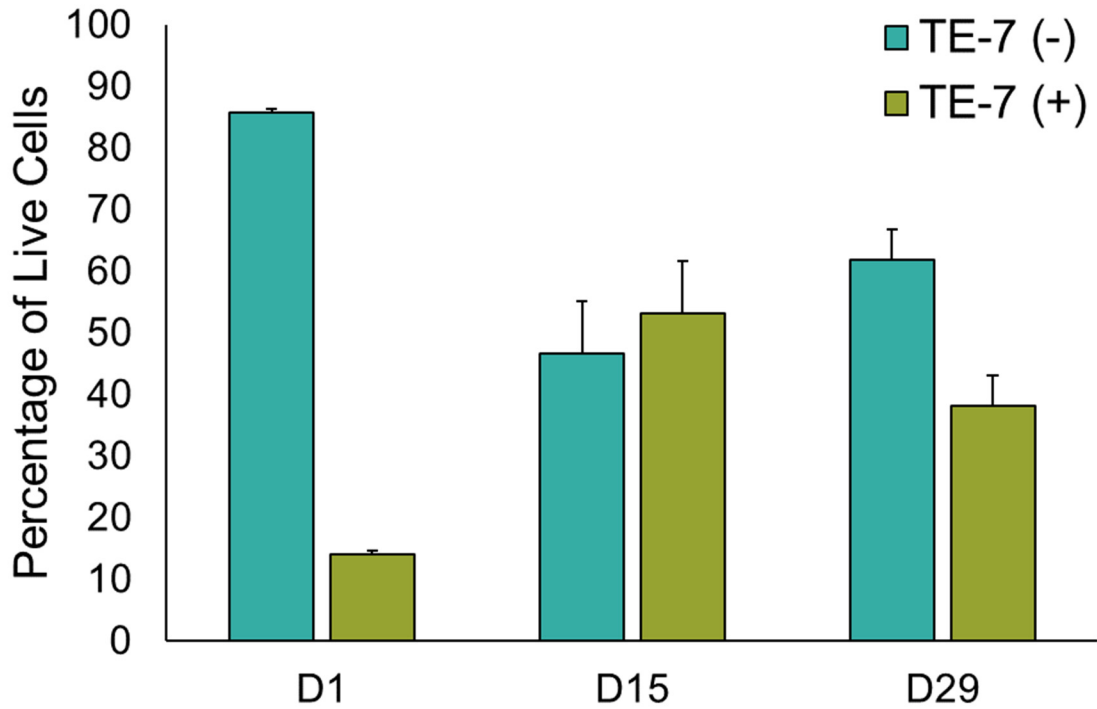
Figure 22: Quantification of temporal variations in the encapsulated cell population within 5:1 PC-3 to BJ-5ta bioengineered tumor tissues. *The encapsulated cell population quantified on day 1 post-encapsulation was found to be very close to the intended cell ratio and presented a very small standard deviation between samples. Fibroblasts were found to proliferate at a higher rate than prostate cancer cells leading up to day 15, however, did not maintain this as culture time progressed. (Error bars represented a population based standard deviation; n = 2 repetitions with 5 bioengineered tumor tissues per repetition)*

To better understand how the initial cancer cell to fibroblast ratio during encapsulation affected the final cell population percentages at the end of long-term coculture, 5:1, 2:1, 1:1, and 1:2 cell ratio bioengineered tumor tissues were subjected to flow cytometry. As expected, none of the samples investigated appeared to maintain their

initial encapsulated cell ratio over 29 days in coculture, as shown in Figure 23. Surprisingly, a very sharp decrease was noted between the 5:1 PC-3 to BJ-5ta fibroblast ratio hydrogels and the 2:1 ratio hydrogels. However, comparatively, there was not a large difference between those bioengineered tumor tissues encapsulated at 2:1, 1:1, and 1:2 cancer cell to fibroblast ratios. It is important to note once more that a portion of the TE-7 negative cell population may include BJ-5ta fibroblast cells that were not positively labelled.
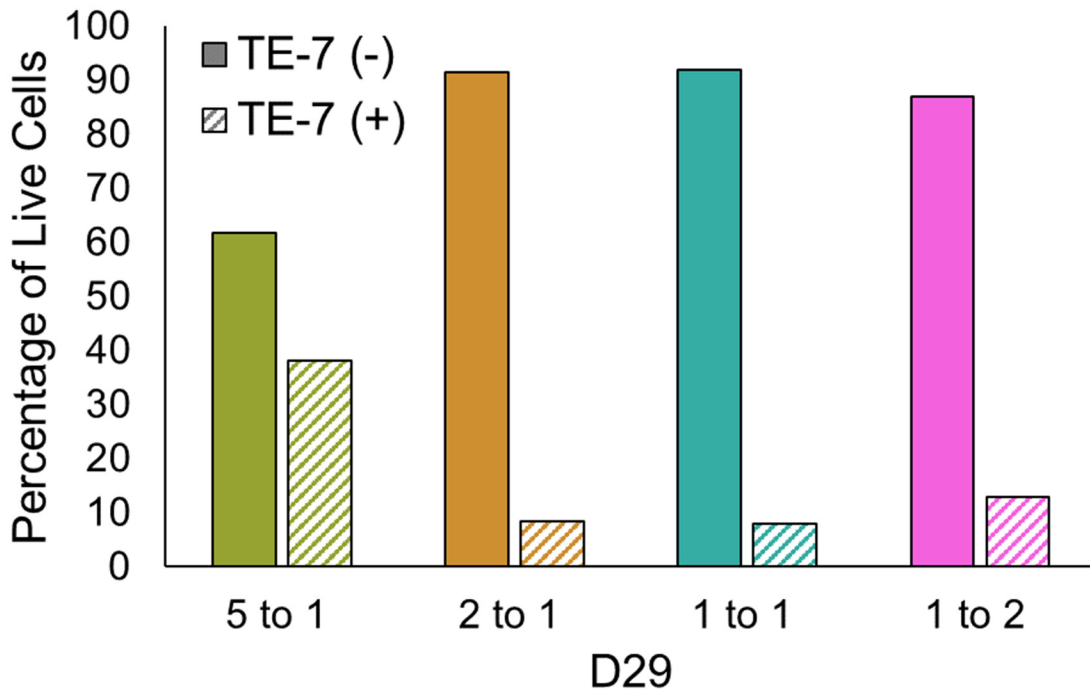
Figure 23: The effect of the encapsulated cell type ratio on live cell population percentages after 29 days in coculture. *Bioengineered tumor tissues did not appear to maintain their initially encapsulated cell population proportions over long-term culture. (5 hydrogels dissociated per each hydrogel type)*

2.3.4. Variations in Mechanical Stiffness in Response to Fibroblast Presence in Coculture

To further characterize the PF hydrogel based bioengineered tumor tissue model, in support of developing a viable *in vitro* 3D cell culture platform, hydrogels were subjected to parallel plate compression testing to quantify changes in mechanical stiffness as a result of the modulation of culture duration and encapsulated cell type. As shown in Figure 24, both PC-3 monoculture and 5:1 PC-3 to BJ-5ta coculture bioengineered tumor tissues were found to present a decrease in their respective Young's moduli over increasing culture time. Notably, PC-3 monoculture hydrogels demonstrated a significant decrease from all other time points in mechanical stiffness on day 29 post-encapsulation. Conversely, 5:1 PC-3 to BJ-5ta coculture hydrogels demonstrated a significant decrease on day 15 post-encapsulation, however, the mechanical stiffness did not continue to reduce significantly throughout the remaining culture time.

The maximum Young's modulus value achievable by PC-3 monoculture PF tissues was found to be approximately 1300 Pa. Surprisingly, the maximum Young's modulus value achievable by 5:1 PC-3 to BJ-5ta coculture PF tissues was found to be much lower at approximately 300 Pa. While the encapsulated cells are at a high enough concentration to produce some effect on the overall tissue mechanical stiffness, it is important to note that two different batches of synthesized PF with slightly different protein concentrations were employed in bioengineered tumor tissue fabrication. From this, in addition to the observation that the day 1 values differed significantly between the mono- and coculture hydrogels, it can be determined that the batch of PF utilized can significantly affect the

mechanical stiffness of the bioengineered tumor tissues. Moving forward, it is highly imperative to utilize the same batch throughout the duration of a round of experiments.
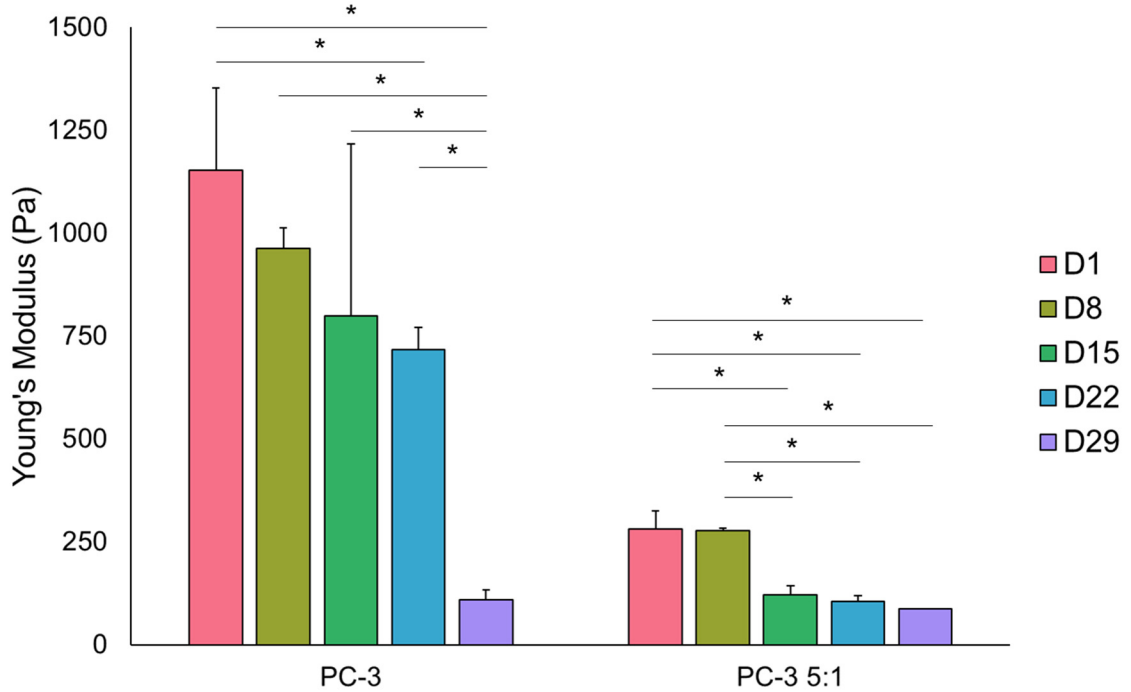
Figure 24: Variations in the Young's modulus of bioengineered tumor tissues in response to modulations in encapsulated cell type and culture duration. *The mechanical stiffness of bioengineered tumor tissues is found to significantly decrease over time regardless of cell type, however, this reduction occurs at an earlier time point in PC-3 and BJ-5ta coculture hydrogels than in PC-3 monoculture hydrogels. (Error bars represent a population based standard deviation, n = 3 hydrogels per time point per encapsulation cell type with 3 repetitions per hydrogel. (*) indicates statistical significance with p ≤ 0.05)*

2.3.5. Impact of Cancer Cell to Fibroblast Ratio on Matrix

Metalloproteinase Secretion in 3D Culture

Thus far, perhaps the most notable observations of modulated PC-3 cell behavior as a result of coculture with BJ-5ta fibroblasts have been the loss of structural integrity by day 29 within the 5:1 cancer cell to fibroblast coculture hydrogels, as evidenced by phase contrast imaging (Figure 8), in addition to the higher rate of reduction in mechanical stiffness, as evidenced by parallel plate compression testing (Figure 24). As a result of this noted overall increase in PF polymer matrix degradation in the presence of PC-3 and BJ-5ta coculture, it was hypothesized that cell signaling pathways initiated through the close contact of cancer and stromal cell types yielded upregulated enzymatic production. More specifically, upregulation of the MMP-2 or MMP-9 gelatinases. To investigate this theorized phenomenon further, a fluorometric assay utilizing the 390 MMP FRET peptide substrate was performed to quantify the levels of MMP-2 and MMP-9 present in conditioned media samples.

To begin, preliminary experiments were completed to determine if the FBS utilized to supplement culture media, or the culture media itself, contained active or pro-MMP-2. Similar investigations also served to find the optimal buffer to conditioned media ratio and optimal suspension solution for the 390 MMP FRET peptide substrate. It was determined that MMP was present in FBS containing media yet was not present in starvation media. As a result, all conditioned media samples were generated through the use of PC-3 starvation media containing only antibiotic supplements. Furthermore, it was found that an optimal signal was produced when the 390 MMP FRET peptide substrate was suspended

in 100% PC-3 starvation media and the conditioned media sample was loaded at a 1:1 ratio with buffer, as defined in *Section 2.2.9*.

Standard samples containing known amounts of pro-MMP-2 suspended in PC-3 starvation media and buffer, in the presence of APMA, were analyzed and the initial rate of fluorescence was employed to generate the standard curve shown in Figure 25. It was determined that this fluorometric assay was not sensitive enough to detect quantities of active MMP at concentrations below 0.13 nM. It is also important to note that conditioned media samples were analyzed both with and without the presence of the activator, APMA, to determine if MMP-2 or MMP-9 present was active or in pro- protein precursor formation.
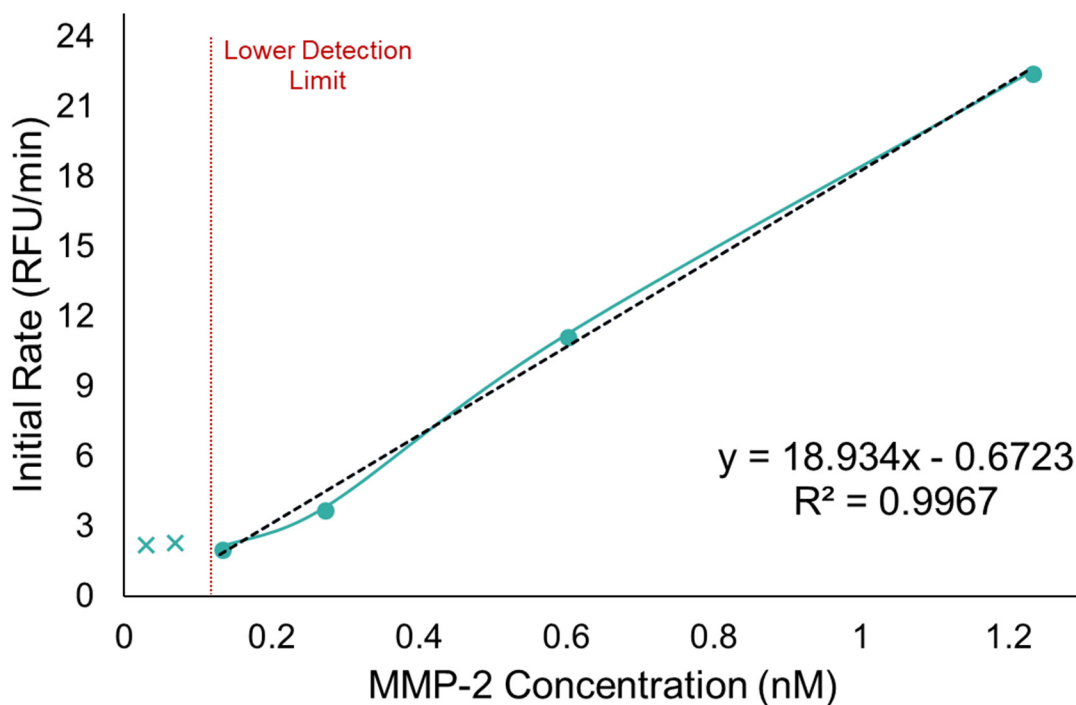
Figure 25: The standard curve for MMP-2 detection in PC-3 starvation media. *The lower detection limit was found to be 0.13 nM. (The linear trendline and corresponding R^2 value are displayed for further quantification of MMP present in experimental samples)*

Surprisingly, neither active nor pro- MMP-2 or MMP-9 were found to be present at quantities above the lower detection limit in PC-3 monoculture or PC-3 and BJ-5ta fibroblast coculture conditioned media samples, regardless of encapsulated cell ratio (PC-3, 5:1, 1:1, 1:5) or culture duration (day 1, 8, 15, 22, or 29). A slight increase in fluorescence was noted in some samples and is shown in Table 1, however, it remained below the detectable and quantifiable limit of this assay. BJ-5ta monoculture bioengineered tumor tissues were found to secrete small amounts of MMP-2 or MMP-9 at early time points. However, as shown in Figure 26, the gelatinases present were in pro- protein precursor formation as they required the APMA activator to generate an increase in fluorescence over time.
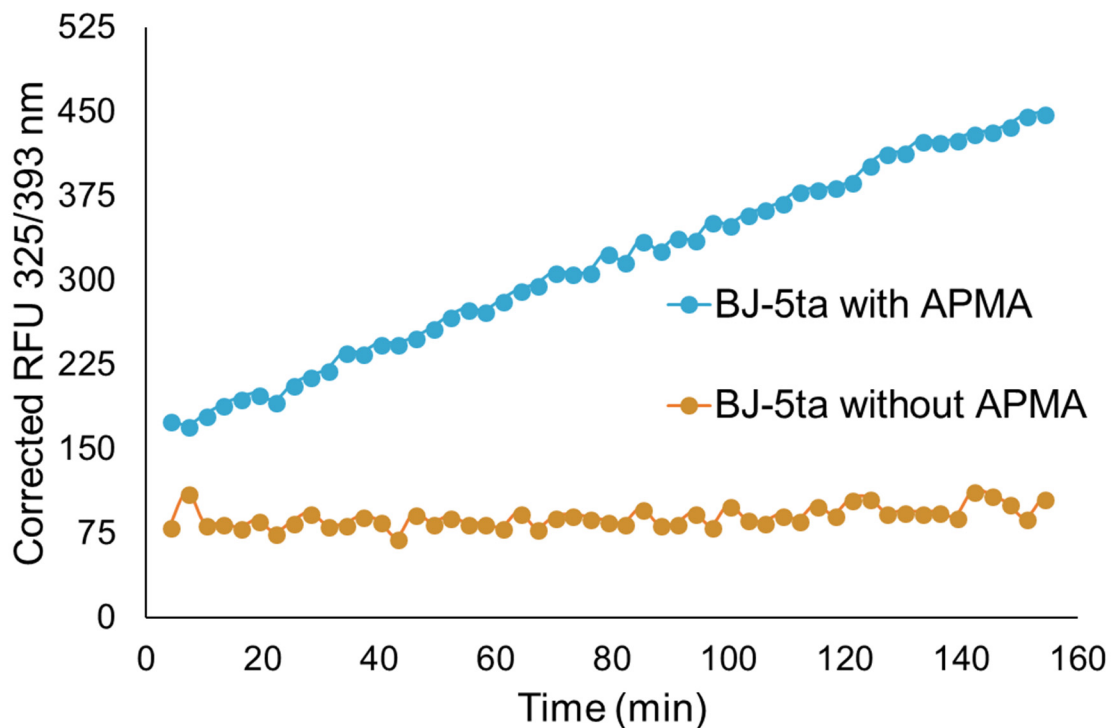
Figure 26: Increase in fluorescence over time due to cleavage of the 390 MMP FRET peptide substrate by pro-gelatinase enzymes secreted by BJ-5ta monoculture bioengineered tumor tissues.

The standard curve equation displayed in Figure 25 was implemented to quantify the concentration of pro-MMP-2 or pro-MMP-9 secreted by BJ-5ta monoculture bioengineered tumor tissues, and the resultant value is displayed in Table 1. To verify that the increase in fluorescence was a result of cleavage of the 390 MMP FRET peptide substrate, the experiment was run again in the presence of the known broad spectrum MMP inhibitor, Ilomastat (GM6001, Galardin), at a concentration of 3.218 μM. As expected, no change in fluorescence was observed, thus indicating MMP inhibition and further validating gelatinase excretion by the samples included in Table 1.

Table 1: The quantified concentration of gelatinases secreted by PC-3 and BJ-5ta bioengineered tumor tissues.

Bioengineered Tumor Tissue Sample	MMP-2 Concentration (nM)
BJ-5ta Monoculture D1	**0.147**
BJ-5ta Monoculture D8	**0.136**
1:5 PC-3/BJ5ta Coculture D1	**0.101**
PC-3 Monoculture D22	**0.075**

While it has become evident that the MMP-2 or MMP-9 gelatinases were not likely responsible for the increase in polymer matrix degradation observed in PC-3 and BJ-5ta monoculture bioengineered tumor tissues, it is likely that another proteinase is the cause. Fibrinogen is known to be cleaved by several other enzymes, including the MMP-3 and MMP-10 stromelysins, the MMP-7 matrilysin, the MMP-12 metalloelastase, plasmin, and thrombin.[107] Moving forward, additional fluorometric assays can be performed utilizing peptide substrates specific to the above listed enzymes. Additionally, bicinchoninic acid

(BCA) assays can be performed to quantify to total protein concentration in conditioned media samples.

2.3.6. Comparison of PC-3 and LNCaP Prostate Cancer Cell Lines

As previously mentioned, the PC-3 cell line represents a highly aggressive, metastatic form of prostate cancer, however, that level of aggression is not always observed *in vivo*. To further evaluate the validity of PF based hydrogels as a biomimetic *in vitro* bioengineered tumor tissue model, the more indolent LNCaP prostate cancer cells were encapsulated at a concentration of 20×10^6 cells/mL, with and without BJ-5ta fibroblasts at a 5:1 cancer to stromal cell ratio. Similar to the PC-3 encapsulations, LNCaP bioengineered tumor tissues were maintained for a period of 29 days and subjected to a myriad of experiments at weekly increments to evaluate cell behavior within the polymer matrix.

Multi-magnification phase contrast imaging was once again performed to monitor cell colonization and migration within the PF scaffold over increasing culture time both at a macrotissue and cellular level. Figures 27 and 28 illustrate limited cell colonization over increasing culture time both with and without the presence of fibroblasts, however, cancer cells within the LNCaP monoculture hydrogel were shown to preferentially migrate to and proliferate around the edge of the biomaterial. Furthermore, between days 1 and 15 post-encapsulation, small, circular, cell-laden fragments of the PF matrix were found to break away from the LNCaP monoculture tissues.

As shown in Figure 29, quantification of changes in cell colony area overtime verified the observation of a narrow colony size distribution, with limited areal growth over time.

67
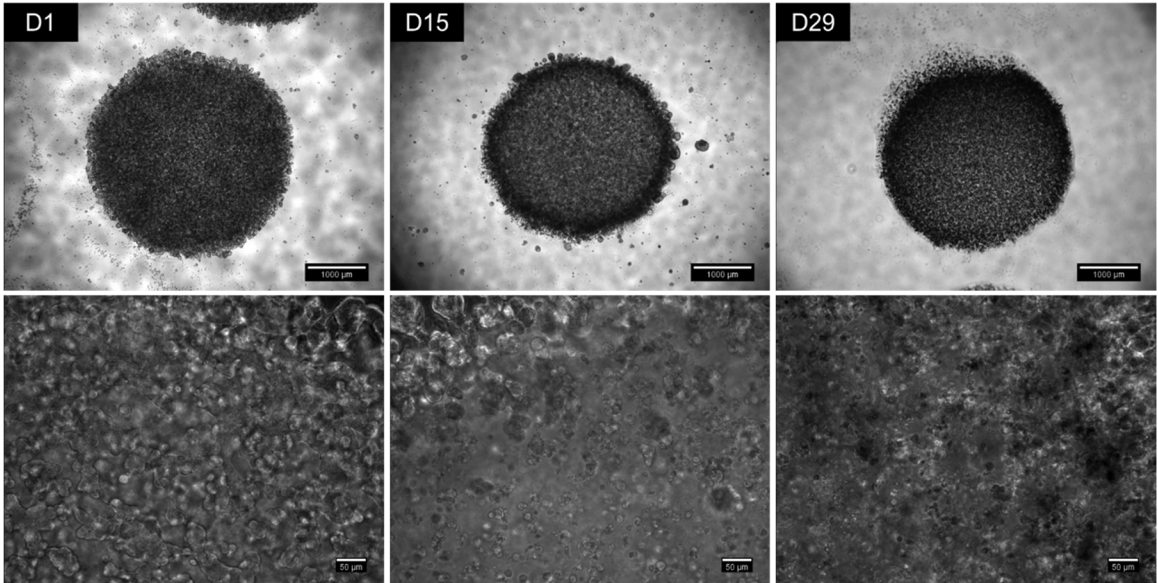
Figure 27: Phase contrast images of LNCaP monoculture bioengineered tumor tissues over 29 days of culture. *Cells are shown in 2X images (top row) to preferentially migrate to and proliferate at the edge of the hydrogel on day 15 post-encapsulation. Furthermore, cell-laden PF polymer matrix fragments were found to break away from the bioengineered tumor tissue between days 1 and 15. Finally, 20X images (bottom row) illustrate little to no increase in colony size over 29 days in culture. (2X scale bars = 1000 μm, 20X scale bars = 50 μm)*
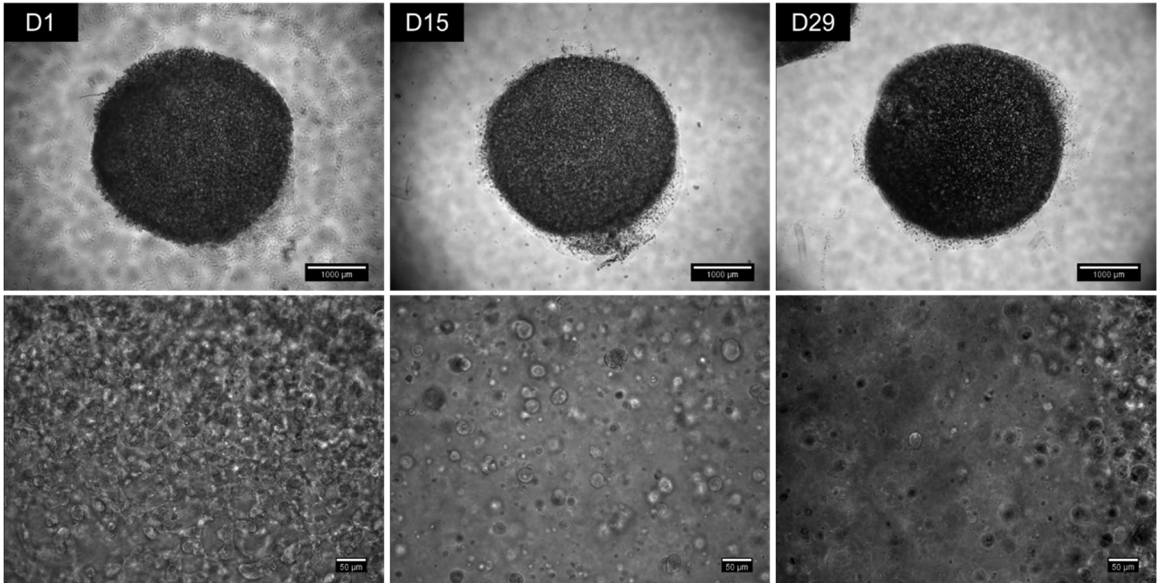
Figure 28: Phase contrast images of 5:1 LNCaP to BJ-5ta cell ratio coculture bioengineered tumor tissues over 29 days of culture. *2X images (top row) present little to no change in the appearance or colonization within the PF matrix over increasing culture time. Furthermore, 20X images (bottom row) illustrate a significant lack of cells or cell colonies in the center of the bioengineered tumor tissue. (2X scale bars = 1000 μm, 20X scale bars = 50 μm)*
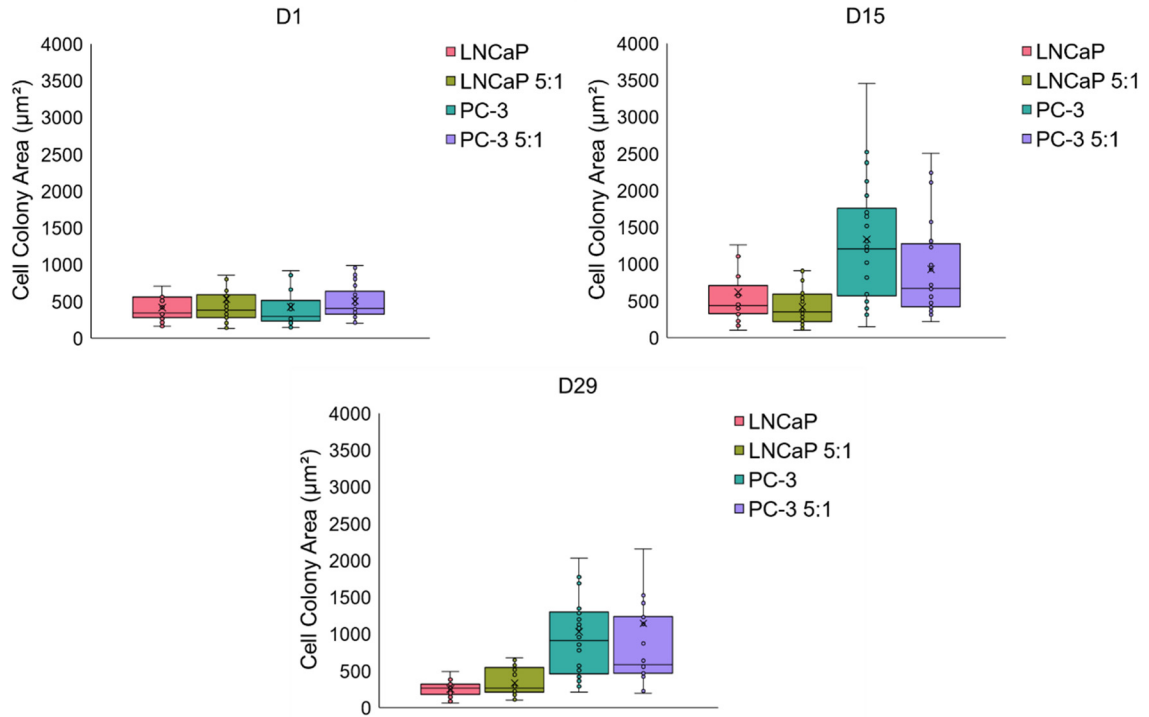
Figure 29: The range of colony areas observed in LNCaP bioengineered tumor tissues over time, as compared to that of PC-3 bioengineered tumor tissues. *As observed through phase contrast imaging, LNCaP monoculture hydrogels present only a slight increase in colony area between days 1 and 15 post-encapsulation, while LNCaP and BJ-5ta coculture colonies remain fairly constant over time. This was observed in stark contrast to PC-3 colonization with and without the presence of fibroblasts. Box and whisker plots illustrate the distribution of collected values, emphasizing the mean, median, upper and lower quartiles, and highest and lowest observations. (n = 25 colonies per bioengineered tumor tissue type per time point)*

To further investigate encapsulated cell behavior on a macroscale, changes in bioengineered tumor tissue area over time were quantified and are displayed in Figure 30. As expected, the LNCaP monoculture bioengineered tumor tissues were found to very slightly decrease in area over increasing culture time, likely due to the fragmentation of PF scaffold around the edge of the hydrogel. Furthermore, 5:1 LNCaP to BJ-5ta coculture tissues were not observed to undergo areal changes over time. Overall, the encapsulated LNCaP and BJ-5ta cells do not appear to remodel their microenvironment over time, which may be indicative of a biomaterial to cell type conflict.
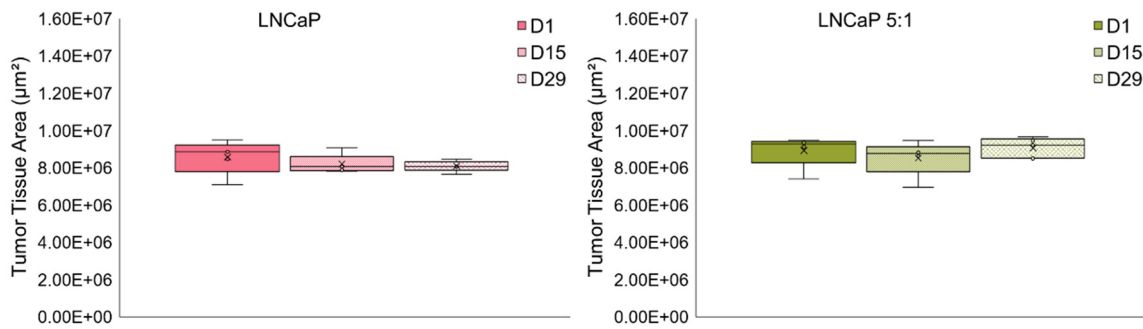
Figure 30: Variations in bioengineered tumor tissue area over time in LNCaP monoculture and coculture with BJ-5ta fibroblasts. *No extreme variations are noted, however, a slight decrease in LNCaP monoculture hydrogel area is observed over time, in addition to area distribution narrowing. Box and whisker plots illustrate the distribution of collected values, emphasizing the mean, median, upper and lower quartiles, and highest and lowest observations. (n = 5 hydrogels per time point per bioengineered tumor tissue type)*

Cellular viability was also assessed to determine if the LNCaP and BJ-5ta cells were able to not only survive the encapsulation process, but also remain viable within the PF matrix over time. Figures 31 and 32 present fluorescence microscopy images on days 1 and 15 post encapsulation. Calcein-AM is shown in green and positively labels live cells, Ethidium homodimer-1 is shown in red and positively labels dead cells, and finally H33342 is shown in blue and positively labels intranuclear double stranded DNA. Limited cell death is observed on day 1 post-encapsulation in both monoculture and coculture hydrogels, with no locational variations or non-uniform viability. However, a large increase in cell death appeared to have occurred between days 1 and 15 in the LNCaP monoculture bioengineered tumor tissues.

Quantification of cell viability, shown in Figure 33, surprisingly revealed that over 80% of encapsulated cells remained viable throughout 15 days of coculture with no drastic decrease in the percentage of live cells. From this result, it can be concluded that the increase in dead cells observed on day 15 in LNCaP monoculture tissues was accompanied by an equal increase in the number of live cells, thus maintaining the initial viability percentage.
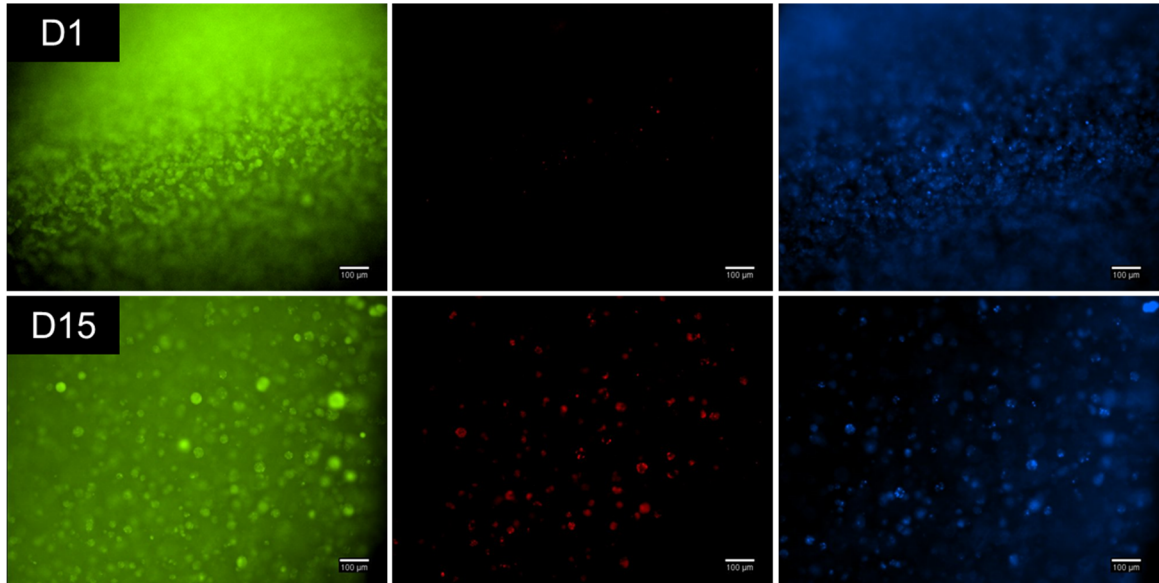
Figure 31: Fluorescence microscopy images illustrating cell viability in LNCaP monoculture bioengineered tumor tissues on days 1 and 15 post encapsulation. *Extremely limited cell death was observed post-encapsulation, however, an increase in cell death was observed by day 15. It is important to note that the hydrogels were situated at an angle during imaging, so only a small number of cells can be in focus at one time, thus resulting in the "blurry" regions of the images shown above. Live cells are shown in green, dead cells are shown in red, and intranuclear double stranded DNA is shown in blue; images were taken at 10X magnification. (10X scale bars = 100 μm)*
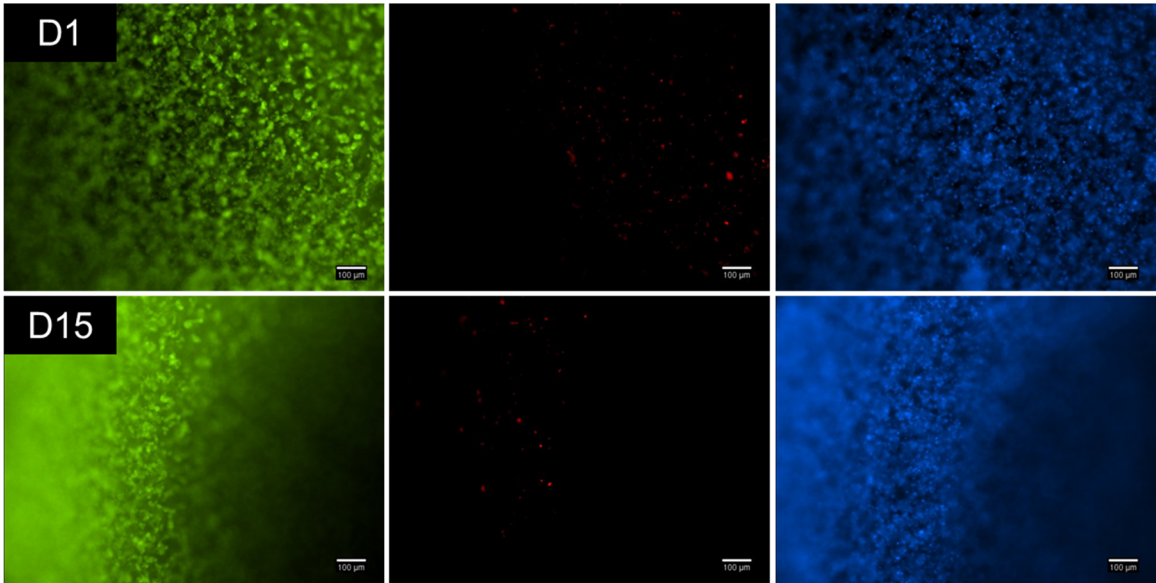
Figure 32: Fluorescence microscopy images illustrating cell viability in 5:1 LNCaP to BJ-5ta bioengineered tumor tissues on days 1 and 15 post-encapsulation. *Limited cell death was observed at both time points. It is important to note that the hydrogels were situated at an angle during imaging, so only a small number of cells can be in focus at one time, thus resulting in the "blurry" regions of the images shown above. Live cells are shown in green, dead cells are shown in red, and intranuclear double stranded DNA is shown in blue; images were taken at 10X magnification. (10X scale bars = 100 μm)*
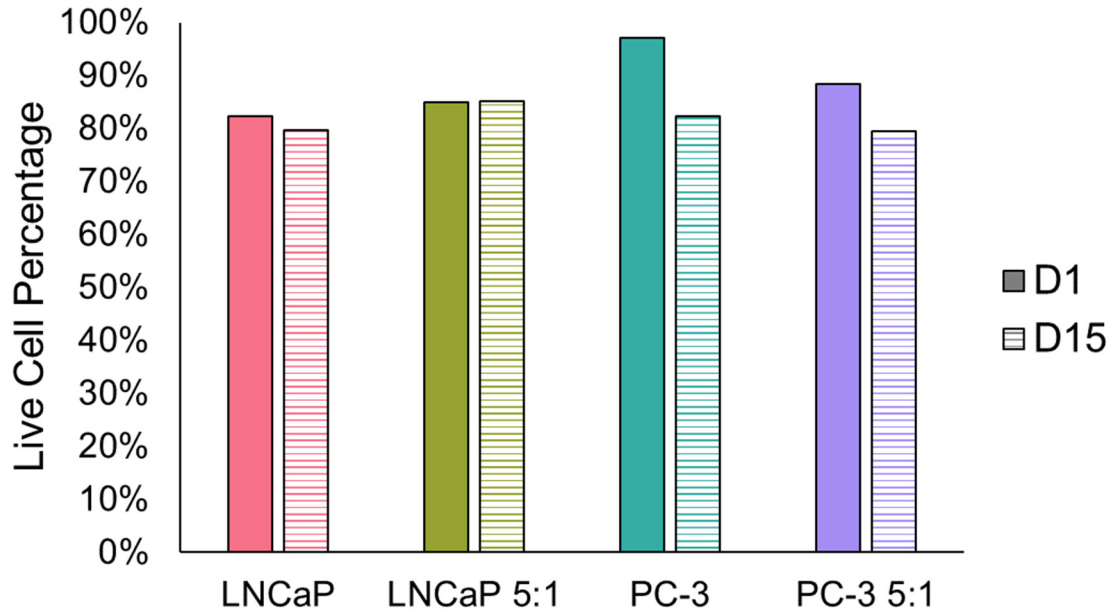
Figure 33: Quantification of cell viability within LNCaP monoculture and coculture bioengineered tumor tissues on days 1 and 15 post-encapsulation. *The percentage of live cells remained greater than 80% within LNCaP monoculture and BJ-5ta coculture hydrogels, regardless of time point. Unlike the PC-3 bioengineered tumor tissues, cell viability was not found to exhibit a large decrease between days 1 and 15.*

To characterize the encapsulated cell morphology within the bioengineered tumor tissue PF matrix, staining and confocal microscopy experiments were performed. Phalloidin was utilized to visualize f-actin filaments in the cytoskeleton and is shown in red and H33342 was utilized to visualize intranuclear double stranded DNA and is shown in blue. Figure 34 presents the resultant 10X magnification images for LNCaP monoculture and 5:1 LNCaP to BJ-5ta coculture hydrogels on day 15 post-encapsulation.

LNCaP monoculture bioengineered tumor tissues were observed to have well-distributed, large, circular cell colonies. Conversely, when in the presence of BJ-5ta fibroblasts, cells were not shown to colonize yet were still evenly distributed throughout the tissue. Furthermore, the presence of f-actin filaments appeared to be limited, as evidenced by the presence of positively stained nuclei without an encircling positive phalloidin stain. This information further contributes to the conclusion that the coculture of BJ-5ta fibroblasts and LNCaP cancer cells does not benefit either cell type.

Image analysis was utilized to quantify the roundness of the cell colonies present in each of the LNCaP bioengineered tumor tissue types. As shown in Figure 35, values were further evaluated through the implementation of a Python function to generate violin plots illustrating the range and frequency of roundness observed, where a value of 1 indicates a perfectly circular colony. As expected, LNCaP bioengineered tumor tissues present near circular colonies, similar to PC-3 bioengineered tumor tissues.
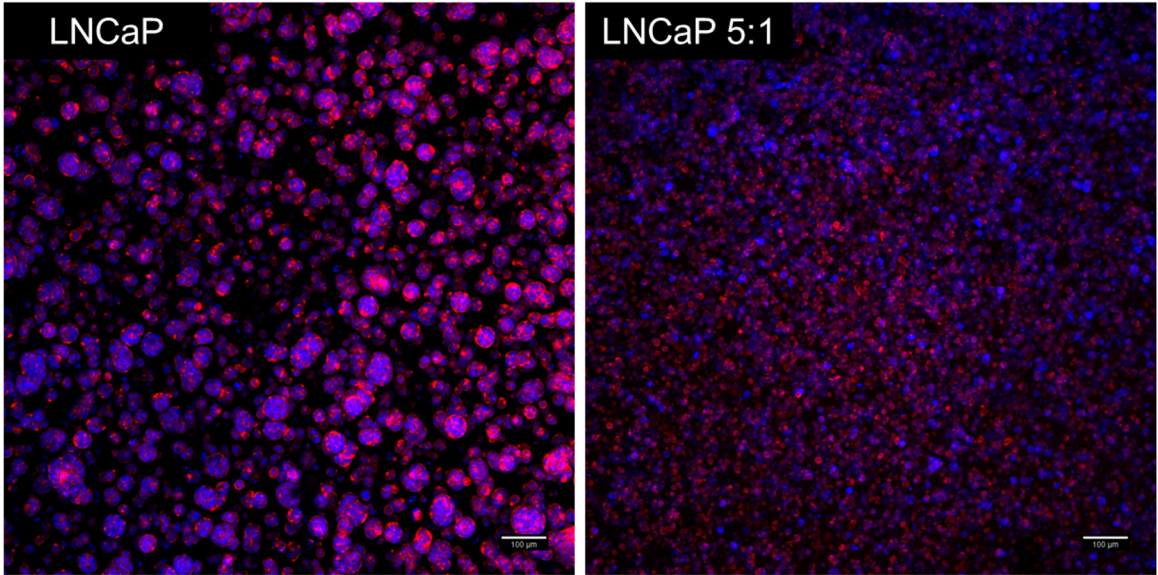
Figure 34: Confocal microscopy images of immunostained LNCaP bioengineered tumor tissues on day 15 post-encapsulation. *Confocal images portrayed the effect of the encapsulated cell type on 3D cell morphology, distribution, and interaction in vitro. F-actin filaments are illustrated in red and intranuclear double stranded DNA is illustrated in blue. (10X scale bars = 100 μm)*
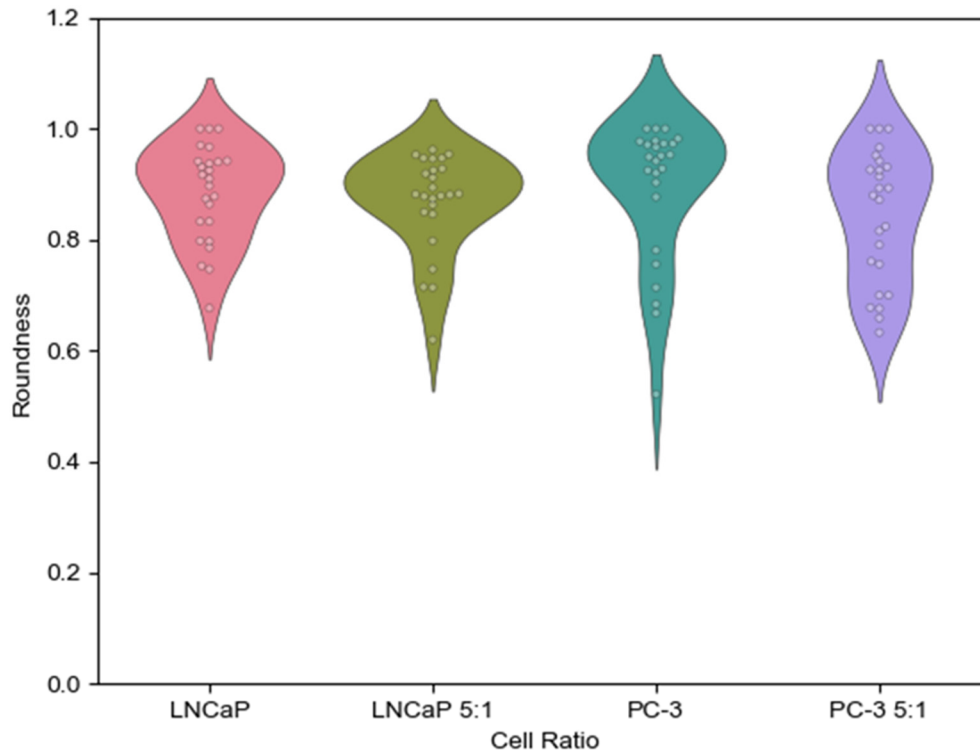
Figure 35: The range and frequency of colony roundness observed within LNCaP bioengineered tumor tissues as composed to that of PC-3 bioengineered tumor tissues. *LNCaP hydrogels both with and without coculture with BJ-5ta fibroblasts presented more round colonies than did PC-3 mono- and coculture bioengineered tumor tissues. Violin plots illustrate the both the range and frequency of the multimodal roundness data collected. (n = 25 colonies per bioengineered tumor tissue type; Roundness = 1 indicates a perfectly circular morphology)*

Similar to the PC-3 hydrogels, LNCaP bioengineered tumor tissues were subjected to parallel plate compression testing to quantify changes in mechanical stiffness as a result of the modulation of culture duration and presence of BJ-5ta fibroblasts. As shown in Figure 36, the Young's modulus was found to slightly vary with increased culture time. However, upon completion of statistical analysis, it was found that the aforementioned modulations do not yield statistical differences as a result of increasing culture time.
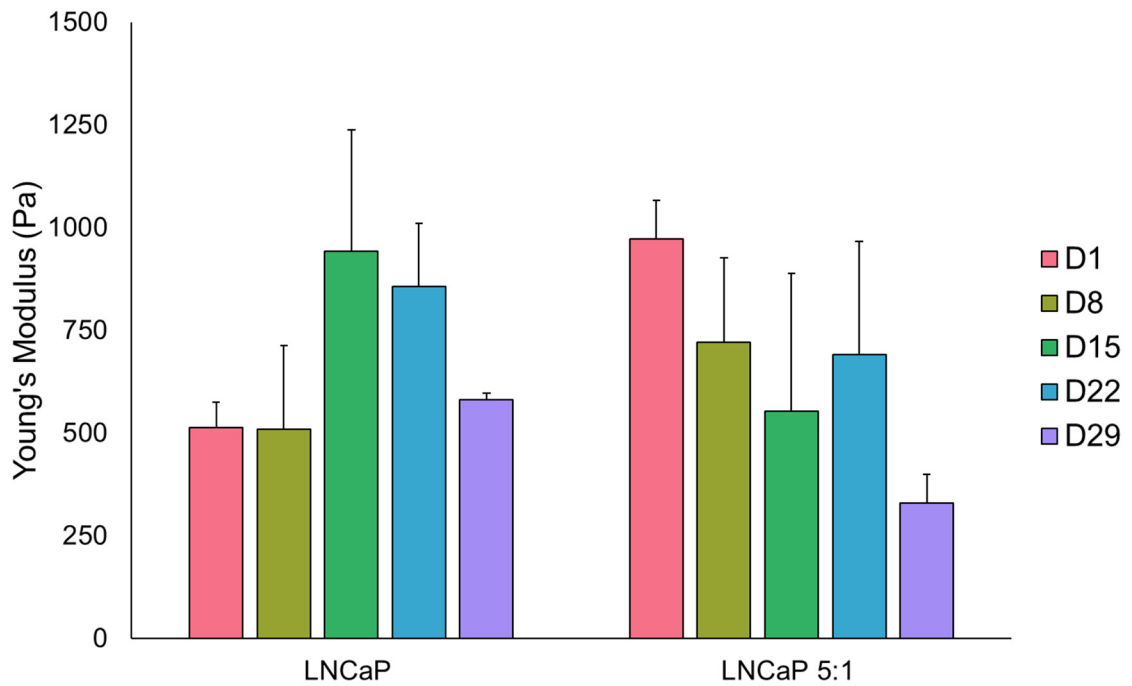
Figure 36: Variations in the Young's modulus of LNCaP bioengineered tumor tissues in response to modulations in encapsulated cell type and culture duration. *The mechanical stiffness was not found to statistically vary over time, regardless of cell type. (Error bars represent a population based standard deviation, n = 3 hydrogels per time point per encapsulation cell type with 3 repetitions per hydrogel. (*) indicates statistical significance with p ≤ 0.05)*

To further characterize the effect of BJ-5ta fibroblast coculture with LNCaP prostate cancer cells, serum-free conditioned media samples were subjected to the same MMP quantification fluorometric assay as the previously analyzed PC-3 serum-free conditioned media samples. However, it is important to note that the starvation media utilized during experimentation was specific to LNCaP cells.

Standard samples containing known amounts of pro-MMP-2 suspended in LNCaP starvation media and buffer, in the presence of APMA, were analyzed and the initial rate of fluorescence was employed to generate the standard curve shown in Figure 37. It was determined that this fluorometric assay was able to detect quantities of active MMP at concentrations at or above 0.027 nM. This increased sensitivity compared to that of the PC-3 starvation media standard curve shown in Figure 25 may indicate that PC-3 starvation media components could possibly inhibit some MMP activity. It is also important to note that conditioned media samples were analyzed both with and without the presence of the activator, APMA, to determine if MMP-2 or MMP-9 present was active or in pro- protein precursor formation. Surprisingly, active MMP-2 or MMP-9 activity was detected in the 5:1 LNCaP to BJ-5ta cell ratio conditioned media samples on day 1 post-encapsulation, as shown in Figure 38.

The standard curve equation displayed in Figure 37 was implemented to quantify the concentration of MMP-2 or MMP-9 secreted by LNCaP and BJ-5ta coculture bioengineered tumor tissues, and the resultant value is displayed in Table 2. To verify that the increase in fluorescence was a result of cleavage of the 390 MMP FRET peptide substrate, the experiment was run again in the presence of the known broad spectrum MMP inhibitor, Ilomastat (GM6001, Galardin), at a concentration of 3.218 μM. Interestingly, a

change in fluorescence was still observed; this result can potentially be explained by two responses. First, it is possible that Ilomastat can only inhibit APMA-activated MMP activity. Secondly, and more likely, MMP is not responsible for the increase in fluorescence. A slight increase in fluorescence was noted in some other samples, however it remained below the detectable and quantifiable limit of this assay.
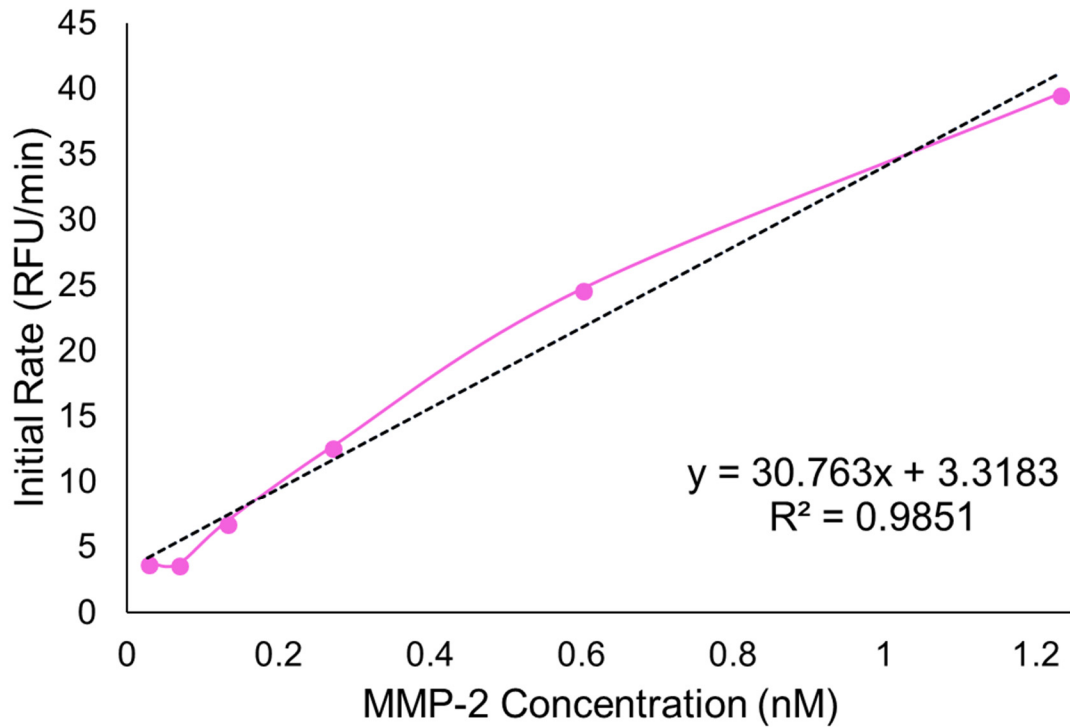
Figure 37: The standard curve for MMP-2 detection in LNCaP starvation media. *The lower detection limit was found to be 0.027 nM. (The linear trendline and corresponding R^2 value is displayed for further quantification of MMP present in experimental samples)*
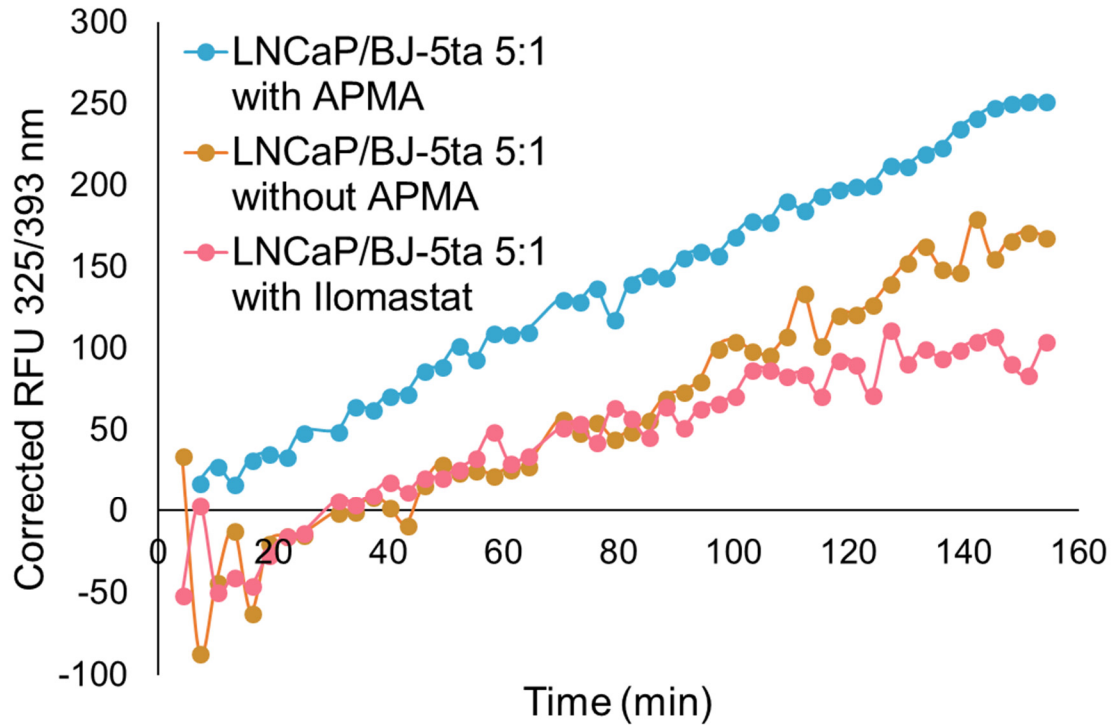
Figure 38: Increase in fluorescence over time due to cleavage of the 390 MMP FRET peptide substrate by proteinases secreted by LNCaP and BJ-5ta coculture bioengineered tumor tissues.

Table 2: The quantified concentration of proteinases secreted by LNCaP and BJ-5ta coculture bioengineered tumor tissues.

Bioengineered Tumor Tissue Sample	Potential MMP-2 Concentration (nM)
LNCaP/BJ-5ta D1 without APMA	**0.0266**

2.4. Conclusions

Overall, the PF biomaterial matrix proved to be an appropriate scaffold for cell-mediated remodeling of the immediate microenvironment, including cell adhesion and cell-mediated enzymatic degradation of fibrinogen, for PC-3, BJ-5ta, and LNCaP cells. Furthermore, all bioengineered tumor tissue remodeling appeared to occur at a cellular level, as expected. Regardless of cell type or cell ratio, encapsulated cells not only survived the encapsulation process, but also maintained greater than 75% cell viability on day 15 of long-term culture.

PC-3 and LNCaP prostate cancer cells consistently exhibited a near-perfectly circular cell morphology, however, colony size was found to decrease with an increasing presence of BJ-5ta fibroblasts. Simultaneously, BJ-5ta cells presented a constricted morphology in the bioengineered tumor tissues comprised of a higher proportion of cancer cells yet were found to elongate and form intricate stromal networks when in an equal or greater ratio with PC-3 cells. Furthermore, locational variations in cell morphology with respect to the z-axis were noted within the cell-laden hydrogels. BJ-5ta cells significantly elongated along the linear top surface of the PF matrix, while those encapsulated within the center of the bioengineered tumor tissue experienced elongation restriction due to the densely, non-patterned crosslinked matrix.

Investigation into changes in encapsulated cell population with respect to modulations in culture duration or initial cell type ratio revealed that the bioengineered tumor tissues do not maintain the preliminary cell ratio over 29 days in coculture.

Surprisingly, BJ-5ta fibroblasts proliferated at a higher rate than PC-3 cancer cells between days 1 and 15 post-encapsulation, however, this trend did not continue beyond day 15.

Quantification of the bioengineered tumor tissue mechanical stiffness through parallel plate compression testing using the MicroSquisher revealed a significant decrease in the Young's modulus at an earlier time point in the PC-3 and BJ-5ta coculture hydrogels than in PC-3 monoculture hydrogels. From this observation, it was hypothesized that the close interaction of cancer and stromal cells types initiated an upregulation in proteinase production, thus leading to an increased rate of degradation of the PF matrix. LNCaP monoculture and BJ-5ta coculture bioengineered tumor tissues, however, did not exhibit a significant change in mechanical stiffness over long-term culture.

Examination in to gelatinase secretion by bioengineered tumor tissues through the implementation of a fluorometric assay surprisingly revealed that the LNCaP and BJ-5ta coculture hydrogels were the only encapsulation type to secrete active proteinases into serum-free culture media at early time points. BJ-5ta monoculture hydrogels were found to secrete inactive pro-MMP-2 on days 1 and 8 post-encapsulation. It is important to note that a change in fluorescence was noted for some PC-3 monoculture and coculture samples, however, the fluctuation remained below the lower detection limit of this assay. From these results it is likely that the PF matrix degradation observed through phase contrast imaging and mechanical stiffness quantification is a result of upregulation in another proteinase such as the MMP-3 and MMP-10 stromelysins, MMP-12 metalloelastase, plasmin, or thrombin. It is recommended that further experimentation be performed to accurately characterize the proteinase cadre present in conditioned media through additional fluorometric or BCA assays.

In conclusion, the implementation of a PF matrix scaffold in the 3D culture of prostate cancer cells with supporting stromal fibroblasts demonstrated significant potential to serve as a valid model for the *in vitro* recapitulation of the native TME. Overall, encapsulated cells were found to exhibit a higher degree of *in vivo* biomimicry than conventional 2D cancer cell culture. As a result, it is likely that the bioengineered tumor tissues reported in this section would be able to more accurately predict anti-cancer therapeutic behavior in the human body than current *in vitro* testing platforms.

Chapter 3.   Recapitulation of the Native Prostate Tumor Tissue Stiffness in

Tunable PEG-fibrinogen Based Hydrogels

3.1. Introduction

Throughout the tumorigenic process, locational heterogeneities in tumor tissue microarchitecture are found to develop as a result of aberrant angiogenesis and a subsequently induced oxygen and nutrient gradient within the 3D mass. This phenomenon consequentially modulates the biochemical and biophysical cues provided to the tumor and stromal cell cadre and additionally yields three distinct regions of heterogeneous cellular behavior and tissue stiffness. Those cells located in a hypoxic environment, far from vascular supply, are found to become necrotic and exhibit a lower ECM stiffness, whereas those receiving an adequate amount of oxygen and nutrients are aggressively proliferative, resulting in a stiffer microenvironment. Cells in existence between these two extreme regions, are found to exhibit a quiescent state in which they are neither dead nor actively dividing.[108] While these zones do not consistently correlate to a precise geometric region within a 3D tumor tissue, necrotic regions are typically found at the core of the mass, proliferative regions are typically found at the periphery of the mass, and finally, quiescent regions are typically found in between, at the midpoint.

To accurately recapitulate the TME *in vitro*, tissue engineered tumor models must acquire the ability to modulate the mechanical properties of the biomaterial scaffold to

mimic a range of stiffnesses observed *in vivo*. Strong correlations have been found to exist between cell culture platform stiffness and acquired chemoresistance and varied drug response, thus significantly impacting the model's ability to accurately predict anti-cancer therapeutic efficacy in the human body.[39] Furthermore, variations in matrix stiffness have also been found to induce changes in cell lineage, gene expression, and intracellular signaling pathways, as well as to initiate the epithelial-mesenchymal transition.[109-112] Overall, it is imperative that *in vitro* tumor models begin to augment their biomimicry of the microarchitecture found in native cancer tissues.

To further increase the physiological relevancy of the PF based bioengineered PC-3 and BJ-5ta coculture prostate tumor tissues presented in *Chapter 2*, this study aims to stiffen the biomaterial scaffold and modulate the mechanical properties of the hydrogel through the addition of excess poly(ethylene glycol) diacrylate during the encapsulation process. As previously shown, the incorporation of 1% (w/v) and 2% (w/v) excess PEGDA was found to significantly increase the Young's modulus of acellular hydrogels, while simultaneously decreasing the diffusion coefficient into the 3D biomaterial.[97] Resultant changes in encapsulated cell behavior due to modulation of the scaffold composition are monitored and reported. Furthermore, this study aims to provide an *in vivo-in vitro* tissue stiffness comparison through the quantification of the range of stiffnesses observed in *in vivo* PC-3 tumors, as compared to the stiffness range achievable by *in vitro* bioengineered PC-3 tumor tissues. Overall, these findings can be utilized to further validate the ability of the PF based bioengineered prostate tumor tissue model to accurately recapitulate the native tumor microenvironment.
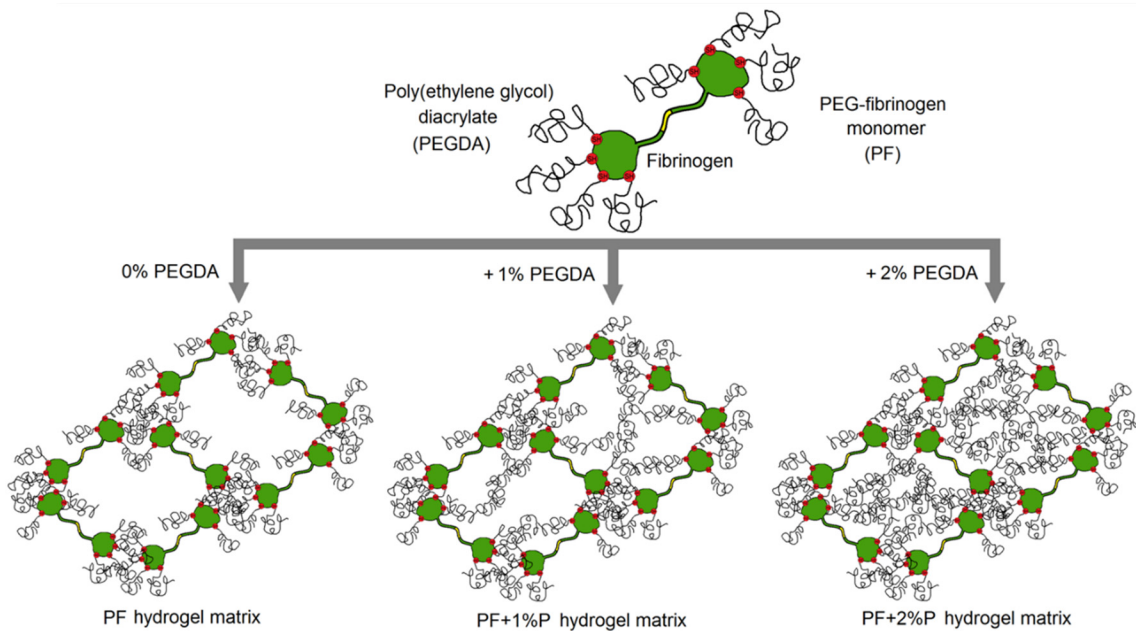
Figure 39: PEG-fibrinogen hydrogel assembly in the presence of 1% and 2% excess PEG diacrylate. *The mechanical properties of PF biomaterial scaffolds can be modulated through the addition of excess PEGDA. (Reprinted with permission from Pradhan et al. 2016)*

3.2. Materials and Methods

All chemicals were acquired from Sigma-Aldrich (St. Louis, MO) unless stated otherwise.

3.2.1. PEGDA Synthesis and Characterization

PEGDA was synthesized according to established protocols.[106] 10kDA molecular weight PEG was reacted with acryloyl chloride (1:4 molar ratio) in anhydrous dichloromethane with triethylamine (1:2 molar ratio) under argon overnight at 25 ºC. The

resultant PEGDA was purified through phase separation with 2M potassium carbonate. The organic phase, containing PEGDA, was dried using anhydrous magnesium sulfate and subsequently filtered. Finally, the synthesized PEGDA was precipitated utilizing diethyl ether, again filtered, and dried overnight under vacuum at 25 ºC. ^{1}H NMR was performed to characterize the degree of acrylation achieved during synthesis. PEGDA was stored at -20 ºC.

3.2.2. PEG-fibrinogen Synthesis and Characterization

PF was synthesized according to established protocols.[70] Bovine fibrinogen was dissolved in an 8M urea solution in 10mM PBS at a final concentration of 7 mg/mL. TCEP-HCl was added to the solution at a TCEP to fibrinogen cysteine molar ratio of 1.5:1. The final solution pH was adjusted to 8.0. Synthesized PEGDA was also dissolved and subsequently centrifuged in an 8M urea in 10mM PBS buffer solution at a final concentration of 280 mg/mL. The PEGDA solution was slowly added to the fibrinogen solution, and the consequent reaction was allowed to proceed under dark conditions for 3 hours at 25 ºC. The reaction solution was next diluted with an equal volume of the urea-PBS buffer solution and precipitated through the addition of acetone at a 4:1 volumetric ratio of acetone to reaction solution. The precipitate product was separated from the liquid phase via centrifugation, weighed, and re-dissolved in the urea-PBS buffer at a final concentration of 2.2 mL buffer per gram of precipitate. The product solution was then dialyzed against 1L sterile PBS three times over a period of 24 hours under dark conditions at 4 ºC. The final PF product was aliquoted into sterile microcentrifuge tubes and stored at -80 ºC. A standard Pierce™ BCA Protein Assay Kit (Thermo Fisher Scientific, Rockford, IL) was utilized to characterize the protein concentration of the synthesized PF.

3.2.3. *In Vivo* Tumor Sample Preparation

In vivo PC-3 PCa tumors were generated in collaboration with Dr. Robert D. Arnold (Department of Drug Discovery and Development, Auburn University) by subcutaneously injecting PC-3 cells suspended in sterile Matrigel into the flank of partially immunocompromised, athymic nude mice. Two separate groups of PCa tumors were produced for the *in vivo/in vitro* comparison study: group 1 (G1) mice were injected with 1×10^6 cells/mL, whereas group 2 (G2) mice were injected with 2×10^6 cells/mL. Tumor growth was measured weekly by palpating the tumor mass and measuring the dimensions with calipers to estimate the volume. Tumors were excised from the host animal at diverse sizes ranging from approximately 300 mm³ – 1500 mm³ to ensure adequate intertumoral heterogeneity was assessed in regard to the native mechanical stiffness of the tumor tissue.

Upon excision, tumors were sliced into approximately 2 mm thick sections and labelled as core, midpoint, or periphery, depending on their original geometric location within the tumor mass. A 3 mm diameter biopsy punch was then utilized to yield disc-shaped samples that mimic the geometry of the bioengineered tumor tissues. A total of five G1 and ten G2 tumors were harvested; each tumor was sectioned to yield up to three samples from each of the three geometric locations, depending on the original tumor size. *In vivo* prostate tumor tissue samples were placed in 1X PBS and immediately analyzed utilizing the MicroSquisher apparatus.

$$Approximate\ Volume_{tumor} = \frac{\pi}{6} \times (L_{tumor} \times W_{tumor} \times H_{tumor}) \qquad 7$$
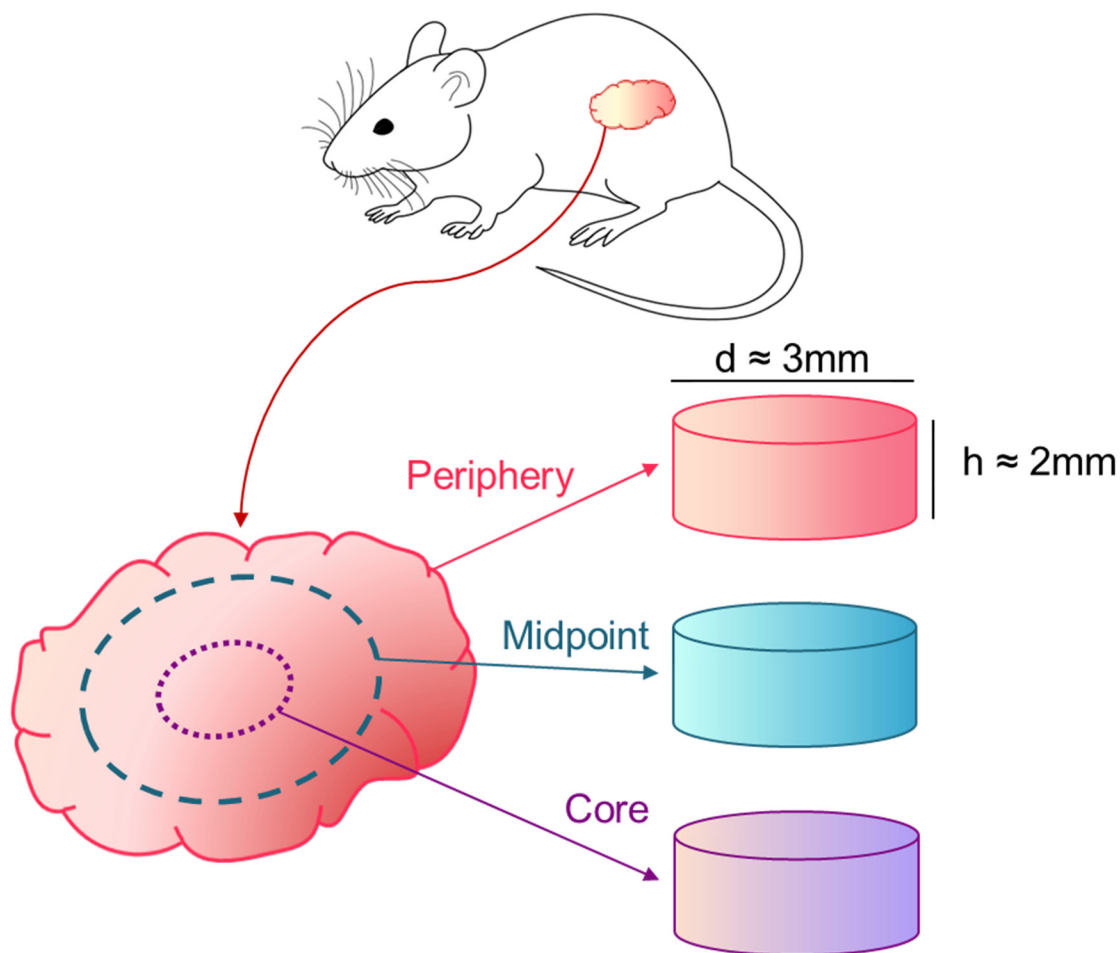
Figure 40: *In vivo* **PC-3 tumor excision and subsequent sample preparation.** *PC-3 tumors are excised from the host animal and subsequently sectioned into samples similar in geometry to the in vitro bioengineered tumor tissues, from three geometric regions of the original tumor mass.*

3.2.4. Cell Culture and Maintenance

PC-3 human prostatic adenocarcinoma cells were kindly provided by Dr. Allan David (Department of Chemical Engineering, Auburn University). PC-3 cells were cultured in F-12K culture media (Corning®, Corning, NY) supplemented with 10% FBS (Atlanta Biologicals, Flowery Branch, GA) and 1% (v/v) Pen-Strep (GE Healthcare Bio-Sciences, Pittsburgh, PA). BJ-5ta normal human foreskin hTERT immortalized fibroblasts

were acquired from ATCC (Manassas, VA) and were cultured in 4 parts of DMEM (Lonza, Walkersville, MD) containing 4 mM L-glutamine, 4.5 g/L glucose and 1.5 g/L sodium bicarbonate, and 1 part of Medium 199 supplemented with 0.01 mg/mL hygromycin B (MilliporeSigma, Burlington, MA), and 10% FBS.

All cells were maintained within plasma-treated polystyrene tissue-culture flasks stored in a humidified atmosphere with 5% CO_2 and a constant temperature of 37 ºC; culture media was renewed twice weekly. Cells adherently cultured in 2D were enzymatically dissociated from the tissue-culture flask surface in preparation for passaging or 3D culture utilizing 0.25% trypsin/2.21 mM EDTA (Corning®, Corning, NY).

3.2.5. Cell Encapsulation in PF Hydrogels with Excess PEGDA

Bioengineered tumor tissues were formed in cylindrical shaped PDMS molds, which were prefabricated for use in the encapsulation process. PDMS sheets were constructed utilizing the SYLGARD 184 Elastomer Kit (Thermo Fisher Scientific, Rockford, IL) and shaped utilizing a 4mm diameter biopsy punch. PDMS molds were firmly adhered to the bottom of a 6-well polystyrene plasma treated tissue-culture plate to prevent leakage of the cell-laden hydrogel precursor solution. The hydrogel precursor solution was prepared by adding 1.5% (v/v) TEOA, 37 mM NVP, and 0.1 mM Eosin Y as a photoinitiator to the synthesized PF in solution with 1X PBS. With the aim of modulating the mechanical stiffness of the bioengineered tumor tissues, excess synthesized PEGDA at a concentration of 250 mg/mL in solution with 1X PBS was added to the hydrogel precursor solution at volumetric ratios of 96:4 (1% w/v) and 92:8 (2% w/v).

To encapsulate cells within the hydrogel scaffold, cancer and stromal cells maintained in 2D tissue-culture flasks were enzymatically dissociated from the flask

surface as previously stated, counted utilizing a hemocytometer with 0.4% Trypan Blue (Lonza, Walkersville, MD), and resuspended in the hydrogel precursor solution at a concentration of 20×10^6 cells/mL at a ratio of 5:1 PC-3 cancer cells to BJ-5ta fibroblasts. A volume of 10 μL of the cell-laden hydrogel precursor solution was pipetted into each PDMS mold well and photocrosslinked via high-intensity visible light exposure (light intensity: 203 mW/cm^2) for 2 minutes. Upon crosslinking completion, the PDMS mold was carefully peeled back from the well plate surface, thus leaving behind disc-shaped, bioengineered tumor tissues. Appropriate culture media was added to the well plate, which was finally stored in a humidified atmosphere with 5% CO_2 and a constant temperature of 37 ºC; culture media was renewed twice weekly.

3.2.6. Image Acquisition and Analysis

Phase contrast images of the bioengineered tumor tissues were acquired at several levels of magnification (2X, 10X, 20X) utilizing an inverted Nikon Eclipse Ti microscope fitted with an Andor Luca S camera on culture days 1, 8, 15, 22, and 29, post-encapsulation. The resultant images were analyzed utilizing ImageJ software, version 1.52c, to quantify both whole hydrogel tissue and individual cell colony physical characteristics. ROI were delineated on the acquired phase contrast images utilizing the ImageJ software capabilities and the tissue or colony area and roundness were subsequently measured and exported to Microsoft Excel. Please refer to *Section 2.2.5.* for equations utilized in analysis.

3.2.7. Cell Viability Investigation

Encapsulated cell viability was assessed via fluorescent microscopy through the visualization and quantification of both live and dead cells within the bioengineered tumor tissues. Utilizing the LIVE/DEAD™ (Invitrogen, Carlsbad, CA) mammalian cell

93

cytotoxicity kit, live cells were positively labeled with green-fluorescent Calcein-AM, indicating intracellular esterase activity and an intact plasma membrane. Simultaneously, dead cells were positively labeled with red-fluorescent Ethidium Homodimer-1, indicating the loss of plasma membrane integrity. The H33342 fluorochrome (CAT#: 382065, MilliporeSigma, Burlington, MA) was also used to positively label DNA within all cellular nuclei. It is important to note that the photoinitiator utilized during the encapsulation process auto-fluoresces on the same wavelength as the Calcein-AM live cell stain and thus can interfere with image analysis.

Bioengineered tumor tissues were incubated in the LIVE/DEAD/H33342 stain on days 1 and 15 post-encapsulation for 30 minutes at 25 ºC, washed with 1X PBS, and imaged utilizing an inverted Nikon Eclipse Ti microscope fitted with an Andor Luca S camera. The live cell stain was visualized via the FITC filter, the dead cell stain was visualized via the TRITC filter, and the nuclei stain was visualized via the DAPI filter. The resultant z-stack images were analyzed with ImageJ software and cellular viability was quantified by manually counting the live and dead cells in each slice of the z-stack.

3.2.8. Immunostaining and Fluorescence Microscopy

The 3D cell morphology and population distribution of cancer and stromal cells within the bioengineered tumor tissues was visualized by immunostaining and confocal fluorescent microscopy on days 1, 15, and 29. Alexa Fluor™ 568 Phalloidin (CAT#: A12380, Thermo Fisher Scientific, Rockford, IL) at a 1:200 dilution in 1X PBS was utilized to positively label F-actin filaments. H33342 at a 1:200 dilution in 1X PBS was utilized to positively label intranuclear DNA. Finally, a Zenon™ Alexa Fluor™ 647 Mouse IgG$_1$ Labeling Kit (CAT#: Z25008, Thermo Fisher Scientific, Rockford, IL) was employed

with the anti-fibroblast monoclonal antibody clone TE-7 (CAT#: CBL271, MilliporeSigma, Burlington, MA) at a 1:100 dilution.

In preparation for staining, bioengineered tumor tissues were washed in 1X PBS and fixed overnight at 4 ºC with 4% PFA (Electron Microscopy Sciences, Hatfield, PA). Encapsulated cells were permeabilized with 0.5% Triton-X for 30 minutes and subsequently blocked via incubation in 0.2 μm filtered blocking buffer (10% FBS and 0.5% BSA in 1X PBS) for 1 hour at 25 ºC. Bioengineered tumor tissues were then labelled in a Phalloidin/Zenon™ Alexa Fluor™ 647-TE-7 staining solution for a minimum of 1 hour at 25 ºC, rinsed with 1X PBS, again labelled in a H33342 staining solution for a minimum of 1 hour at 25 ºC, and finally rinsed with 1X PBS.

Immunostained bioengineered tumor tissues were mounted on glass coverslips and imaged utilizing confocal microscopy (Nikon AI Confocal Scanning Laser Microscope). The Phalloidin stain was visualized via the TRITC filter, the H33342 stain was visualized via the DAPI filter, and finally the Zenon™ Alexa Fluor™ 647-TE-7 stain was visualized via the CY5HQ filter. Fluorescent images were analyzed utilizing ImageJ software and ROI were drawn to quantify the area, roundness, and major axis to minor axis aspect ratio of each of the cell colonies throughout the z-stacks; calculated values were then exported to Microsoft Excel. Please refer to *Section 2.2.5.* for equations utilized in analysis.

3.2.9. Mechanical Stiffness Quantification

The mechanical stiffness of the bioengineered tumor tissues on days 1, 8, 15, 22, and 29 post-encapsulation and the *in vivo* prostate tumor tissues post-excision was quantified via parallel plate compression testing under physiological conditions through the use of a MicroSquisher (CellScale, Waterloo, ON, CA) apparatus according to

manufacturer instructions. *In vitro* and *in vivo* samples were loaded onto a stage at the front of a fluid bath test chamber filled with 1X PBS and held at 37 ºC. A 558.8 μm diameter tungsten wire microcantilever beam fitted with a compression platen was affixed to the vertical piezo motor driven actuator at a 90º angle and positioned at the top of the sample. Tissues were compressed to a minimum 15% deformation at a maximum compression rate of 10 μm/s for three cycles. The force applied to the sample was calculated via deflection of the microcantilever beam with a typical force resolution of 34.52 μN; tissue displacement was tracked with the MicroSquisher system camera and analyzed utilizing ImageJ software. Force versus displacement data was gathered and exported to a custom Microsoft Excel macro to create a compressive stress (σ) versus strain (ε) curve; the linear portion slope of which yielded the Young's modulus of the sample. All tissue samples were tested in triplicates. Please refer to *Section 2.2.10.* for equations utilized in analysis.

3.2.10. Statistical Analysis

Statistical analysis was performed utilizing Minitab 18 Statistical Software (Minitab Inc., State College, PA). One-way ANOVA with Tukey's family error rate of 0.5% was used to evaluate the statistical significance between multiple groups. If the variance was unequal between groups, the Games-Howell post-hoc test was subsequently performed. All values presented are mean ± SD.

3.3. Results and Discussion

3.3.1. Impact of Matrix Stiffness on Encapsulated Cell Behavior

PC-3 metastatic prostate cancer cells were successfully encapsulated with BJ-5ta fibroblasts at a 5:1 cancer cell to fibroblast ratio and concentration of 20×10^6 cells/mL

in PF based hydrogels augmented with 0%, 1%, and 2% excess PEGDA. The bioengineered tumor tissues were maintained for a period of 29 days and temporal variations in encapsulated cell behavior were analyzed in weekly increments.

3.3.1.1. Cell Viability, Colonization, and Migration in 3D Culture

To ensure the modulation of polymer matrix composition did not negate the validity of the PF based bioengineered tumor tissues as a viable scaffold for PC-3 and BJ-5ta cell adhesion, proliferation, colonization, and migration, multi-magnification phase contrast imaging and cell viability assays were performed. Figures 41 through 43 present 2X and 20X magnification phase contrast images on days 1, 15, and 29 post-encapsulation. It can be seen that increasing the amount of excess PEGDA appeared to limit cell colony size yet maintain structural integrity at late culture time points. As expected, cell migration to the edge of the hydrogels appeared to also be limited, likely due to the increased crosslinking density observed with increased PEGDA percentage. Furthermore, cells were found to exhibit a slight preference for proliferation at the edge of the bioengineered tumor tissue, likely as a result of the decreased diffusion coefficient through the biomaterial matrix.

As shown in Figure 44, quantification of changes in cell colony area over time verified the observation of decreased cell colony size with increased excess PEGDA. As expected, cell colonies in PF hydrogels grew significantly over increased culture time, while those in PF+1%PEG hydrogels increased between days 15 and 29. This can potentially be attributed to an increase in delayed cell-mediated degradation of the

fibrinogen backbone at later time points. Cell colonies in PF+2%PEG bioengineered tumor tissues did not exhibit drastic changes over 29 days of coculture.
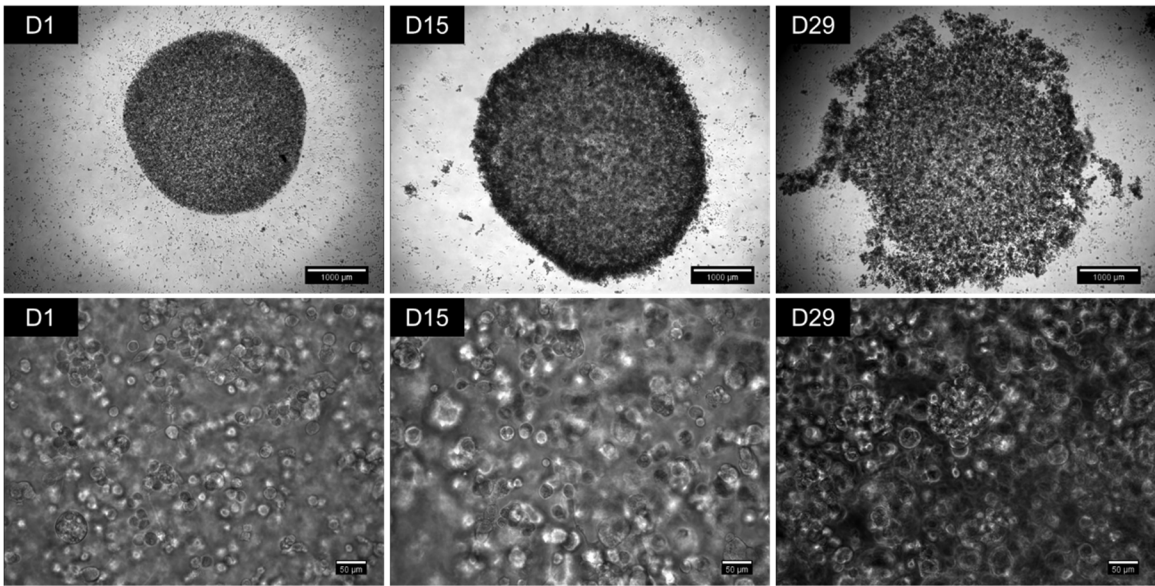
Figure 41: Phase contrast images of 5:1 PC-3 to BJ-5ta cell ratio coculture bioengineered tumor tissues in PF over 29 days of culture. *Cells are shown to proliferate, migrate, and colonize throughout the PF matrix in 2X images (top row) with a slight preference to the edge of the hydrogel, as evidenced by the formation of a dark ring of larger colonies encircling the tissue on day 15. Increased degradation of the PF scaffold is noted on day 29, likely as a result of larger and more proliferative colonies present at the edge of the tissue. Furthermore, 20X images (bottom row) illustrate an increase in colony size from day 1 to day 29 post-encapsulation. (2X scale bars = 1000 μm, 20X scale bars = 50 μm)*
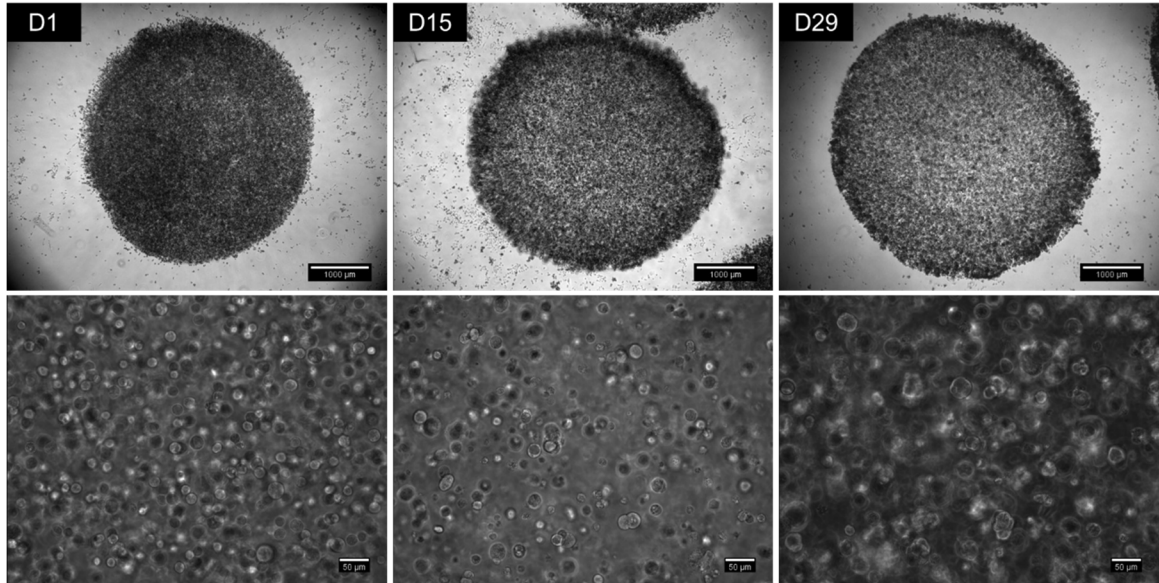
Figure 42: Phase contrast images of 5:1 PC-3 to BJ-5ta cell ratio coculture bioengineered tumor tissues in PF+1%PEG over 29 days of culture. *Cells are shown to proliferate, migrate, and colonize throughout the PF+1%PEG matrix in 2X images (top row) with a slight preference to the edge of the hydrogel between days 15 and 29. Furthermore, 20X images (bottom row) illustrate a slight increase in colony size from day 15 to 29 post-encapsulation. (2X scale bars = 1000 μm, 20X scale bars = 50 μm)*
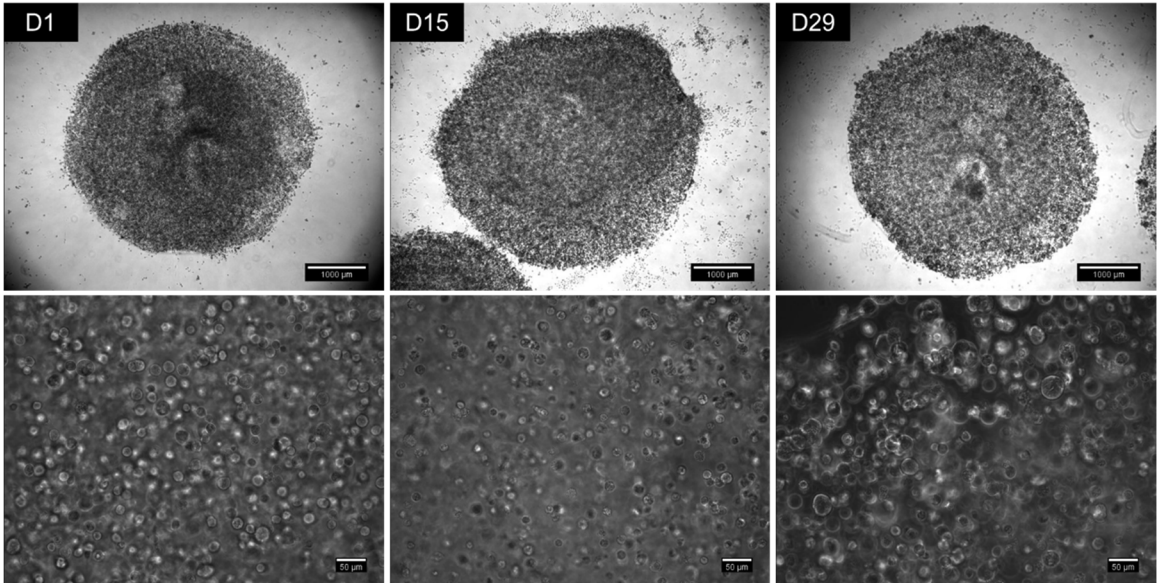
Figure 43: Phase contrast images of 5:1 PC-3 to BJ-5ta cell ratio coculture bioengineered tumor tissue sin PF+2%PEG over 29 days of culture. *Cells are shown to colonize over 29 days in culture in both 2X (top row) and 20X (bottom row) images. However, limited cell migration or locational proliferation is noted. This is likely due to hindered movement throughout the scaffold by increased crosslinking density. (2X scale bars = 1000 μm, 20X scale bars = 50 μm)*
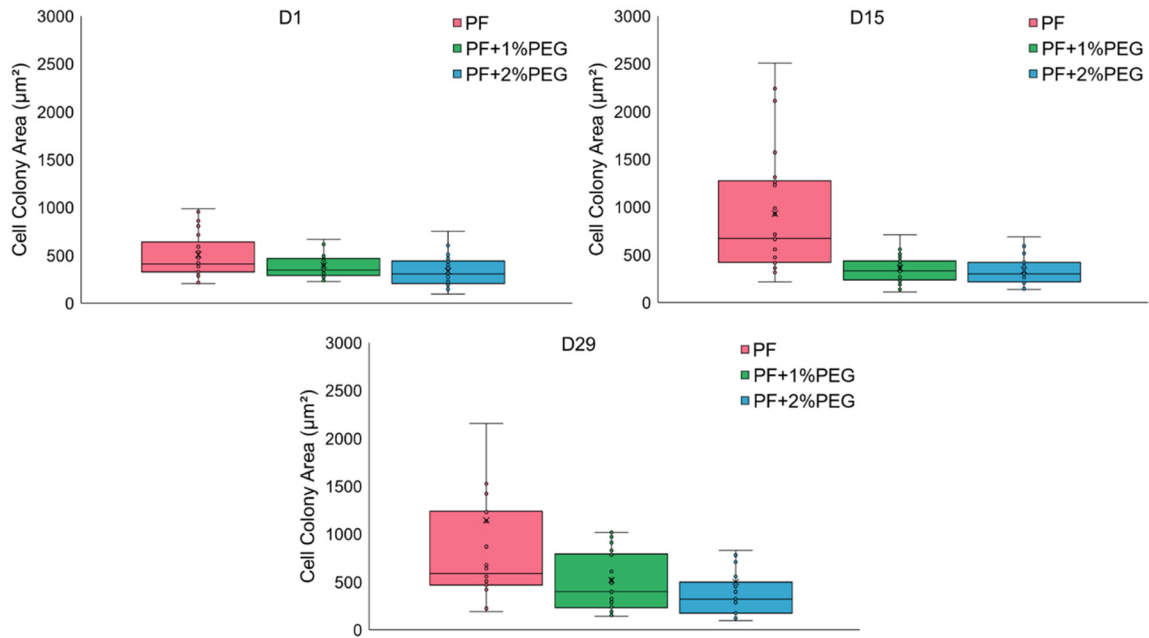
Figure 44: The range of colony areas observed in bioengineered tumor tissues with modulated polymer composition over time. *Cells encapsulated in a PF matrix are shown to exhibit a significant increase in colony area with increasing culture time. However, this increase is delayed in PF+1%PEG scaffolds, while cells adhered to PF+2%PEG scaffolds do not exhibit a drastic increase in colonization over 29 days. Box and whisker plots illustrate the distribution of collected values, emphasizing the mean, median, upper and lower quartiles, and highest and lowest observations. (n = 25 colonies per bioengineered tumor tissue type per time point)*

To further investigate encapsulated cell behavior on a macroscale, changes in bioengineered tumor tissue area over time were quantified and are displayed in Figure 45. As expected PF+2%PEG hydrogels did not exhibit a large change in whole tissue area over time due to limited degradation of the polymer matrix, however, surprisingly PF+1%PEG hydrogels presented a significant areal increase throughout 29 days in culture. This is likely

due to cell colony outgrowth around the edge of the engineered tissue. As previously stated, PF hydrogels increased until day 15 and decreased leading to day 29 due to increased cleavage of the fibrinogen biomaterial scaffold.
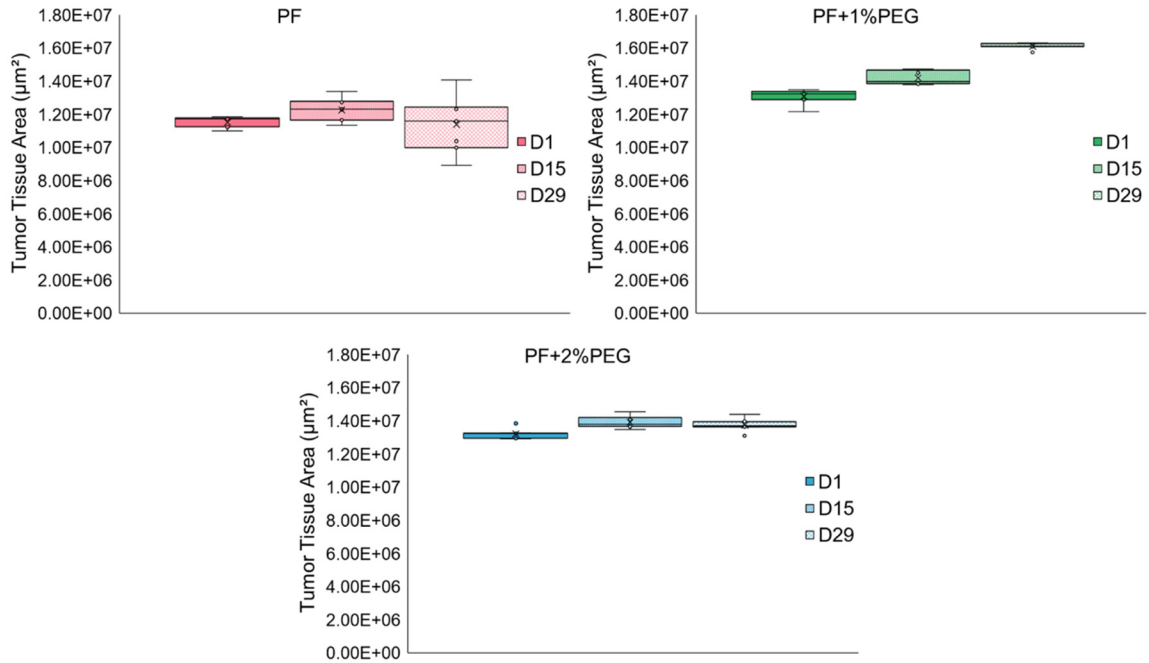
Figure 45: Variations in bioengineered tumor tissue area over time in all polymer compositions. *Surprisingly, a significant increase was observed in PF+1%PEG tissues. However, as expected, PF+2%PEG hydrogels presented a narrow distribution with little to no temporal variations. Finally, quantification of PF hydrogel tissue area illustrated an appropriate increase between days 1 and 15, followed by a slight decrease between days 15 and 29. Box and whisker plots illustrate the distribution of collected values, emphasizing the mean, median, upper and lower quartiles, and highest and lowest observations. (n = 5 hydrogels per time point per bioengineered tumor tissue type)*

Cellular viability was also assessed to determine the impact of modulated polymer composition on the ability of PC-3 and BJ-5ta cells to survive the encapsulation process and maintain high viability over 29 days of culture. Figures 46 through 48 present fluorescence microscopy images on days 1 and 15 post-encapsulation. Calcein-AM is shown in green and positively labels live cells, Ethidium homodimer-1 is shown in red and positively labels dead cells, and finally H33342 is shown in blue and positively labels intranuclear double stranded DNA. Cells were evenly distributed throughout the biomaterial scaffolds, and no locational variations in viability were noted. PF+2%PEG bioengineered tumor tissues appear to exhibit more cell death immediately following encapsulation, however, the presented image represents one slice of a z-stack image and illustrates cells at the center of the hydrogel. A slight increase in cell death was acceptable at this location due to the decreased diffusion of media and nutrients into the crosslinked network. Limited cell death is observed in PF and PF+1%PEG hydrogels.

Quantification of cell viability, shown in Figure 49, revealed a uniform cell viability on day 1, regardless of hydrogel composition. Surprisingly, PF bioengineered tumor tissues presented the largest decrease in viability on day 15 post-encapsulation. As expected, little to no change was observed in PF+2%PEG hydrogels, while a slight increase was noted in those comprised of PF+1%PEG. Overall, cell viability remained greater than 80% irrespective of culture duration or polymer composition. This result confirms that the addition of excess PEGDA does not negate the suitability of PF based scaffolds for 3D *in vitro* coculture of PC-3 and BJ-5ta cells, in regard to cell viability.
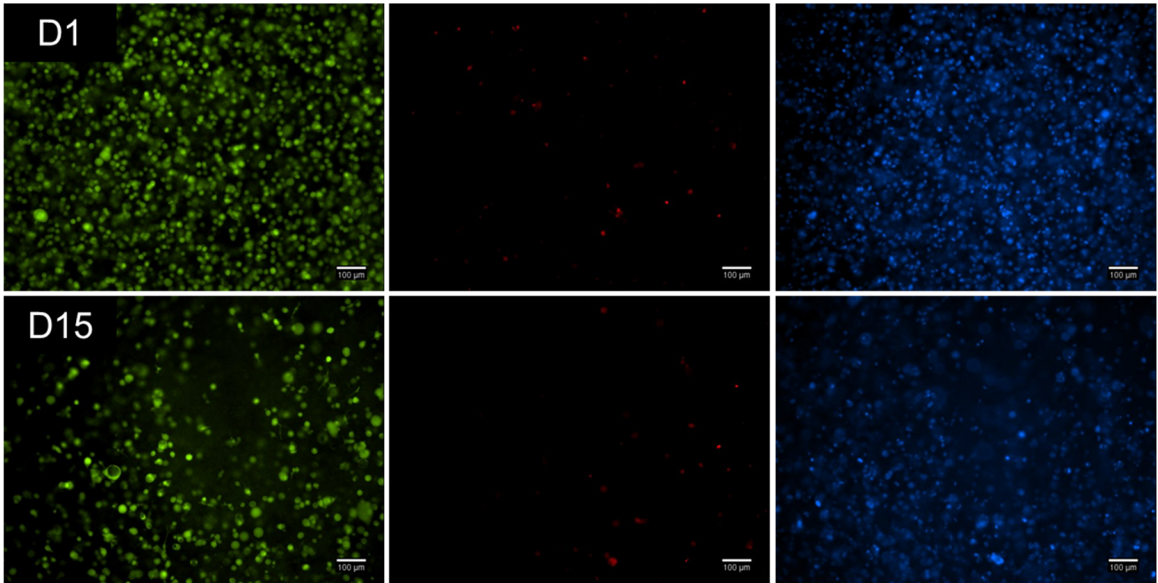
Figure 46: Fluorescence microscopy images illustrating cell viability in PC-3 and BJ-5ta coculture PF bioengineered tumor tissues on days 1 and 15 post-encapsulation.

Very limited cell death was observed at both time points. Live cells are shown in green, dead cells are shown in red, and intranuclear double stranded DNA is shown in blue; images were taken at 10X magnification. (10X scale bars = 100 μm)
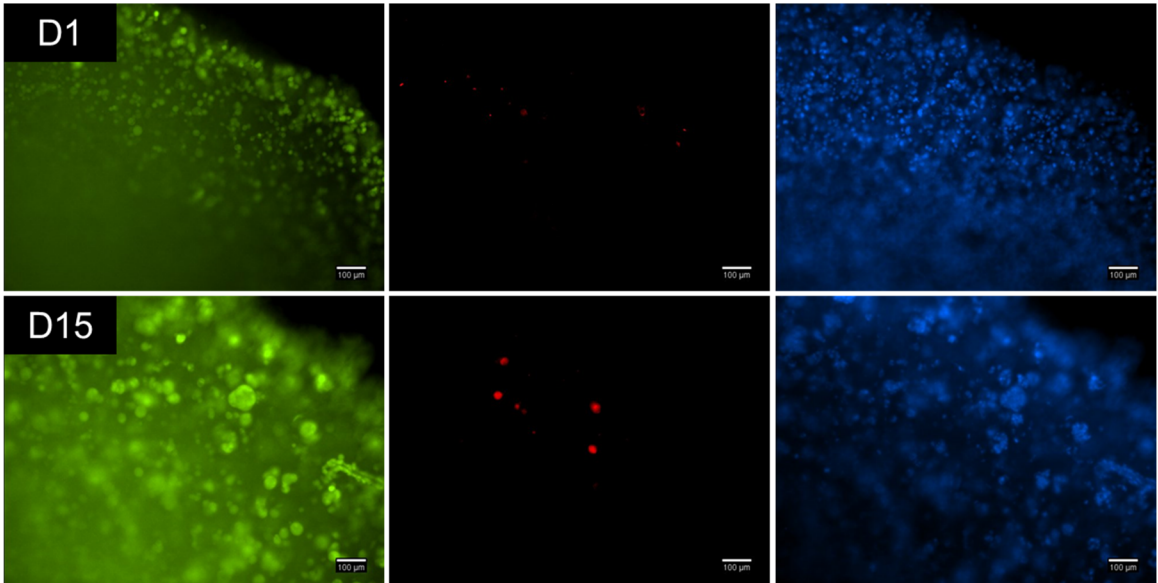
Figure 47: Fluorescence microscopy images illustrating cell viability in PC-3 and BJ-5ta coculture PF+1%PEG bioengineered tumor tissues on days 1 and 15 post-encapsulation. *Extremely limited cell death was observed at both time points. Live cells are shown in green, dead cells are shown in red, and intranuclear double stranded DNA is shown in blue; images were taken at 10X magnification. (10X scale bars = 100 μm)*
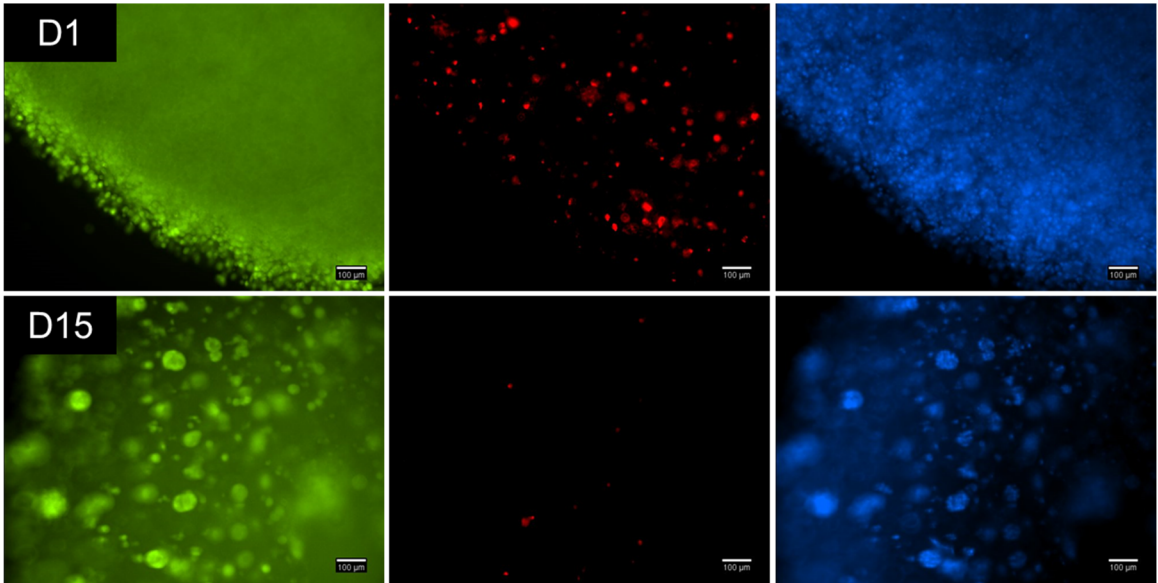
Figure 48: Fluorescence microscopy images illustrating cell viability in PC-3 and BJ-5ta coculture PF+2%PEG bioengineered tumor tissues on days 1 and 15 post-encapsulation. *A larger amount of cell death was noted on day 1 in the PF+2%PEG hydrogels than observed in other polymer compositions. However, this did not continue over 15 days in culture. Live cells are shown in green, dead cells are shown in red, and intranuclear double stranded DNA is shown in blue; images were taken at 10X magnification. (10X scale bars = 100 μm)*
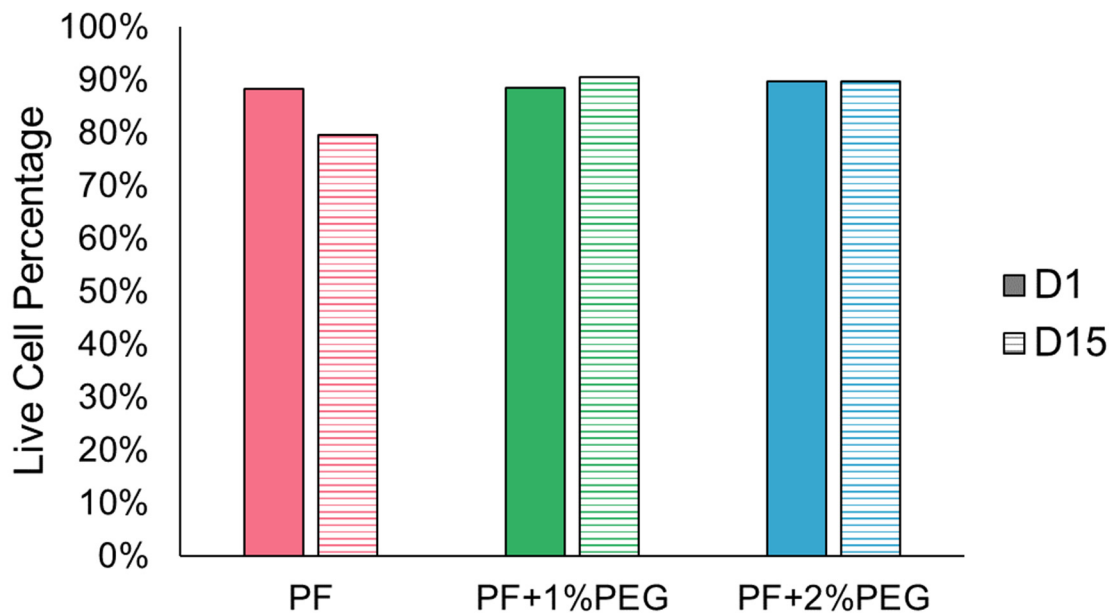
Figure 49: Quantification of cell viability within PC-3 and BJ-5ta coculture bioengineered tumor tissues with varying polymer compositions on days 1 and 15 post-encapsulation. *The percentage of live cells remained greater than 80% within the bioengineered tumor tissues, regardless of time point or amount of excess PEGDA. Surprisingly, stiffening the polymer matrix appears to slightly increase cell viability on day 15, as compared to PF hydrogels.*

3.3.1.2. Cell Morphology in 3D Culture

To characterize variations in the encapsulated cell morphology within the bioengineered tumor tissue matrix in response to the modulation of mechanical properties and diffusion into the hydrogel, immunostaining and confocal microscopy experiments were performed. Phalloidin was utilized to visualize f-actin filaments in the cytoskeleton and is shown in red, H33342 was utilized to visualize intranuclear double stranded DNA and is shown in blue, and finally TE-7 was utilized to positively label fibroblasts and is

shown in green. Figure 50 presents the resultant 10X magnification images for PF, PF+1%PEG, and PF+2%PEG bioengineered tumor tissues on day 15 post-encapsulation.
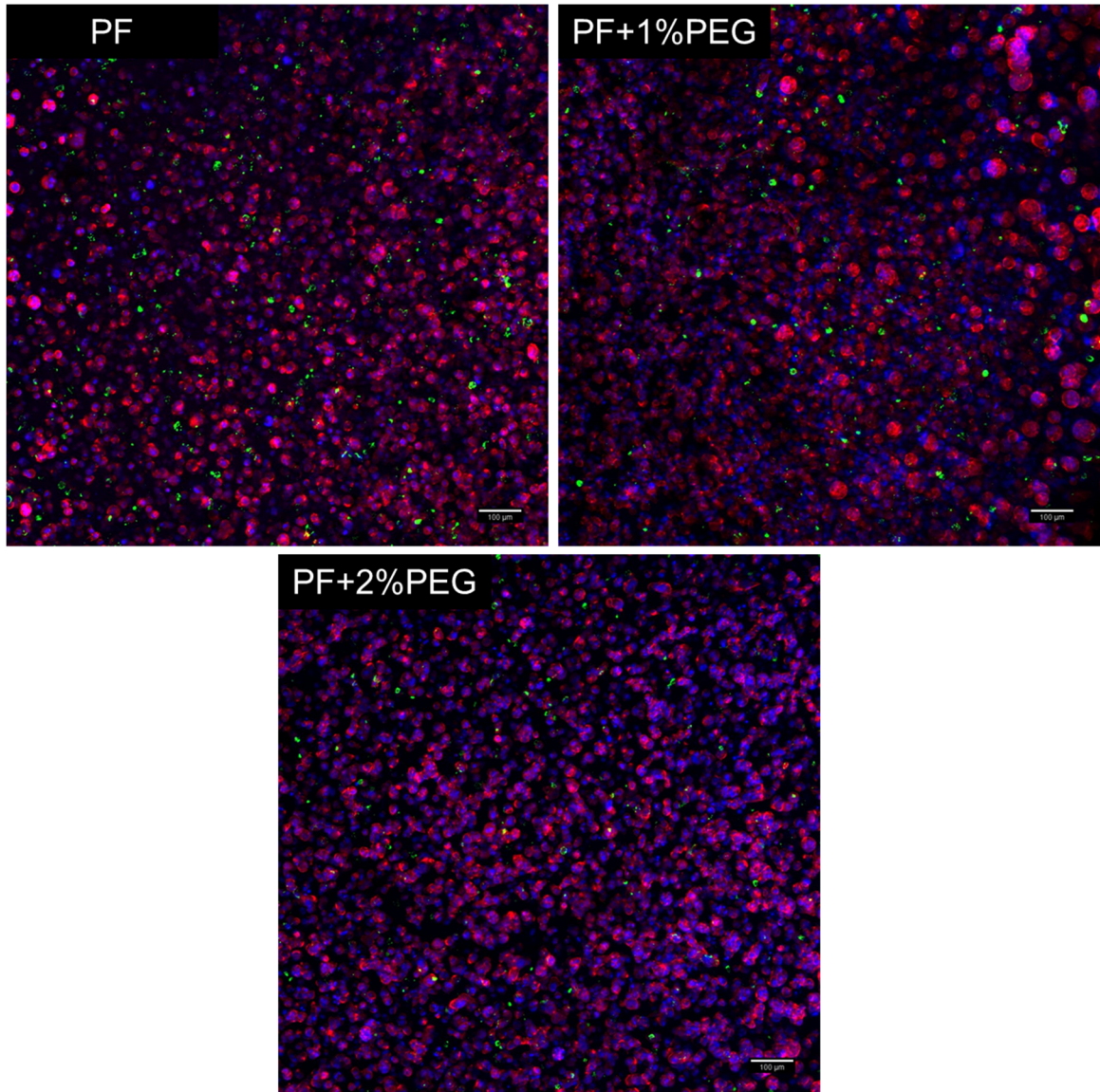
Figure 50: Confocal microscopy images of immunostained PF, PF+1%PEG, and PF+2%PEG bioengineered tumor tissues on day 15 post-encapsulation. *BJ-5ta fibroblasts are illustrated in green, f-actin filaments are illustrated in red, and intranuclear double stranded DNA is illustrated in blue. (10X scale bars = 100 μm)*

PC-3 prostate cancer cells and BJ-5ta fibroblasts were evenly distributed throughout the bioengineered tumor tissues, irrespective of polymer matrix composition. As expected, little to no fibroblast elongation was noted in either the PF, PF+1%PEG, or PF+2%PEG hydrogels. Surprisingly, cell colonies did not appear to differ significantly in size or shape, however, those encapsulated in PF+1%PEG demonstrated a wider range of colony areas. Notably, cells and cell colonies in PF+2%PEG appeared to exhibit a large amount of intranuclear DNA present (stained in blue) relative to f-actin filaments (stained in red) due to the near-triploid characteristic of PC-3 cells and limited elongation as a result of a more densely crosslinked scaffold.

Image analysis was utilized to quantify the roundness of cell colonies present in each of the bioengineered tumor tissue types. As shown in Figure 51, values were further evaluated through the implementation of a Python function to generate violin plots illustrating the range and frequency of roundness observed, where a value equal to 1 indicates a perfectly circular colony. As expected, a relatively narrow roundness distribution was noted in all three polymer compositions, however, surprisingly, colonies were found to be more round in PF+1%PEG and PF+2%PEG hydrogels. This is likely due to the limited ability of the cell colonies to spread through the surrounding matrix scaffold as a result of decreased pore size.
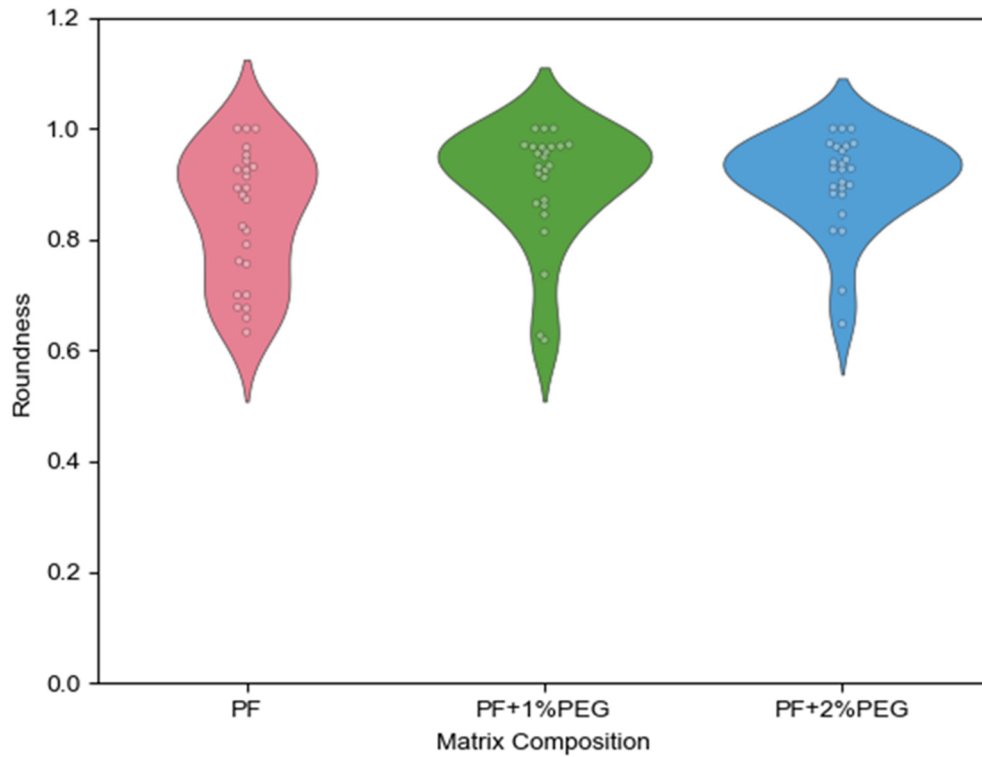
Figure 51: The range and frequency of colony roundness observed in PF, PF+1%PEG, and PF+2%PEG bioengineered tumor tissues. *Cells encapsulated in biomaterial matrices comprised of an increased percentage of PEGDA were found to exhibit more round cell colonies than those in PF. Violin plots illustrate the both the range and frequency of the multimodal roundness data collected. (n = 25 colonies per bioengineered tumor tissue type; Roundness = 1 indicates a perfectly circular morphology)*

3.3.2. Modulation of Mechanical Properties through Polymer Modifications

As previously reported, the addition of 1% (w/v) and 2% (w/v) excess PEGDA resulted in a significant increase in the Young's modulus of acellular PF hydrogels.[97] To ensure this trend was preserved in the presence of PC-3 prostate cancer cells and BJ-5ta fibroblasts, and to evaluate the effect of increased culture duration, bioengineered tumor tissues were subject to parallel plate compression testing. As shown in Figure 52, increasing amounts of excess PEGDA were shown to increase the Young's modulus of the hydrogel, regardless of culture time point. Days 8, 15, 22, and 29 post-encapsulation yielded PF+1%PEG and PF+2%PEG hydrogels with statistically different stiffnesses, as compared to PF hydrogels. On day 1 post-encapsulation, only the addition of 1% excess PEGDA resulted in a significantly stiffer polymer matrix. Non-uniform mixing of the cell-laden polymer precursor solution before pipetting it into the PDMS molds could serve as a potential explanation for the large variations observed between samples of the same polymer composition, as evidenced by large error shown in Figure 52.

To further characterize the range of stiffnesses achievable by the bioengineered PC-3 tumor tissues through modulation of excess PEGDA percentage and culture duration, Figure 53 illustrates a box and whisker plot illustrating the distribution of Young's moduli data. Overall, PF+2%PEG bioengineered tumor tissues exhibited a higher average Young's modulus than PF+1%PEG tissues, which in turn, exhibited a higher modulus than PF tissues. As expected, the widest range of achievable stiffness through variations in culture time was provided by the PF+2%PEG hydrogels, while the narrowest range was observed in PF hydrogels.
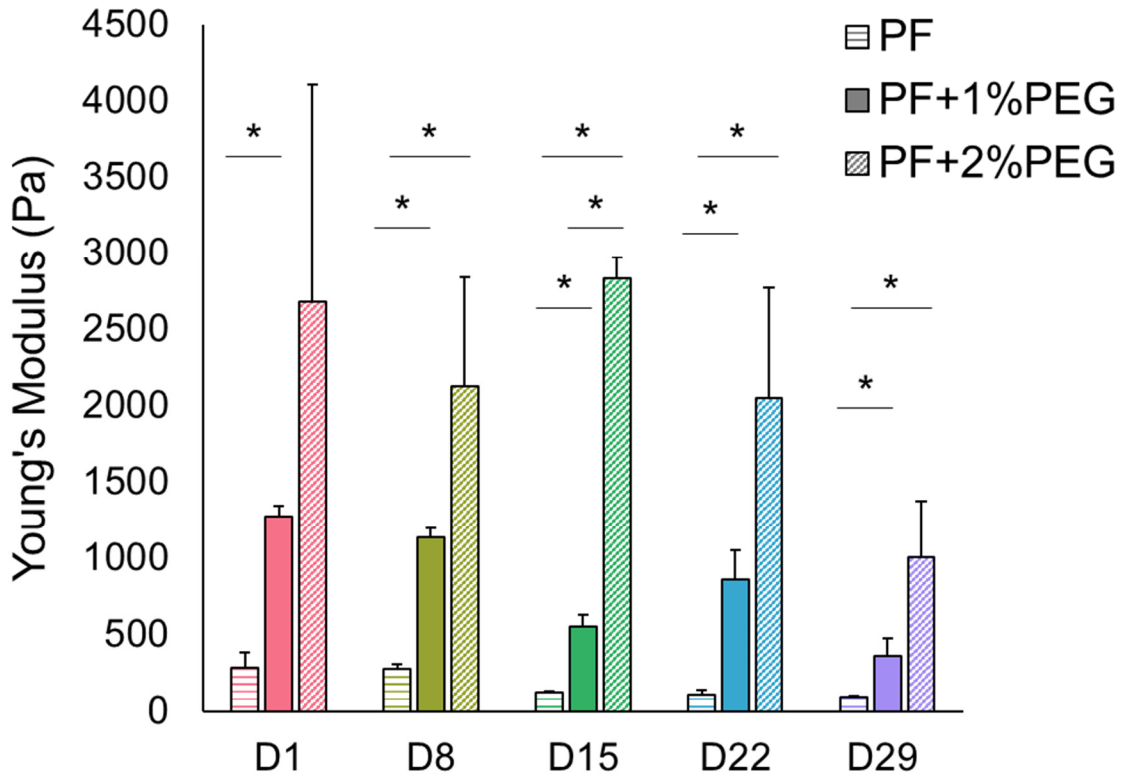
Figure 52: Variations in the Young's modulus of bioengineered tumor tissues in response to modulation of polymer scaffold composition and culture duration. *The mechanical stiffness of bioengineered tumor tissues is found to significantly increase through the addition of 1% and 2% PEGDA on days 8, 15, 22, and 29 post-encapsulation, as compared to PF. (Error bars represent a population based standard deviation, n = 3 hydrogels per time point per encapsulation cell type with 3 repetitions per hydrogel. (*) indicates statistical significance with p ≤ 0.05)*
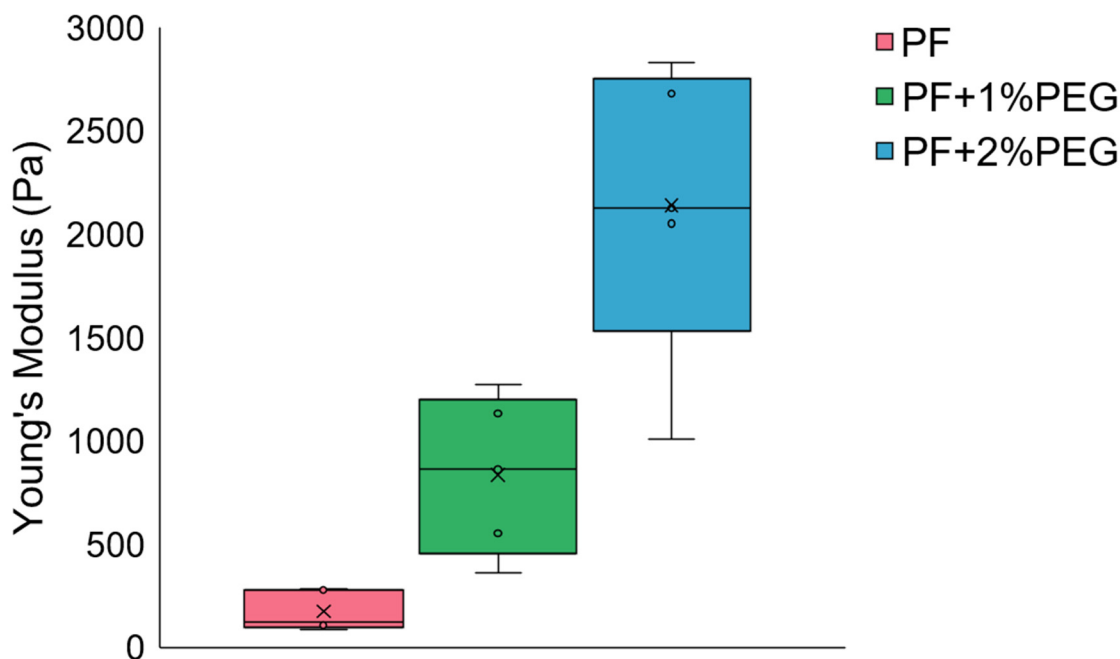
Figure 53: The range of stiffness achievable in *in vitro* bioengineered tumor tissues through the addition of excess PEGDA. *A wide range of stiffnesses ranging from approximately 50 Pa to 2800 Pa are achievable through polymer composition and culture duration modifications. Box and whisker plots illustrate the distribution of collected values, emphasizing the mean, median, upper and lower quartiles, and highest and lowest observations. (n = 15 hydrogels per bioengineered tumor tissue type)*

3.3.3. *In Vitro* Recapitulation of the *In Vivo* Tumor Microenvironment

To generate *in vivo* prostate tumor samples for the *in vivo-in vitro* stiffness comparison study, PC-3 cells suspended in Matrigel were subcutaneously injected into the flank of athymic nude mice. The resultant tumors, as shown in Figure 54, were excised at sizes ranging from approximately 300 mm^3 – 1500 mm^3 to ensure adequate intertumoral heterogeneity and were found to exhibit a myriad of tissue shapes. Table 3 provides

information regarding the time from implantation to excision and final tumor weight for both G1 and G2 tumors. G1 tumors were found to exhibit slightly less noticeable vascularization at the periphery of the tissue mass than G2 tumors. Furthermore, Mouse 42 was found to have a bloody and non-bloody region within the overall excised tumor. The mechanical stiffness was measured separately for each region. Interestingly, this characteristic was also confirmed through multispectral optoacoustic tomography (MSOT) imaging before tumor excision.

Table 3: Logistical information for all excised G1 and G2 PC-3 *in vivo* tumors.

Group Number	Mouse Number	Excision Date (DD/MM/YY)	Growth Duration (days)	Final Tumor Volume (mm^3)
1	6	06/30/17	54	1430.5
1	7	06/30/17	54	707.8
1	8	06/30/17	54	598.4
1	9	06/30/17	54	360.6
1	10	06/30/17	54	642.9
2	33	08/23/17	33	416.2
2	34	09/13/17	54	305.8
2	35	09/28/17	69	431.9
2	36	09/13/17	54	440.7
2	37	09/13/17	54	651.1
2	38	09/28/17	69	819.3
2	39	09/28/17	69	927.4
2	40	08/23/17	33	360.3
2	41	08/23/17	33	393.0
2	42	09/28/17	69	391.9
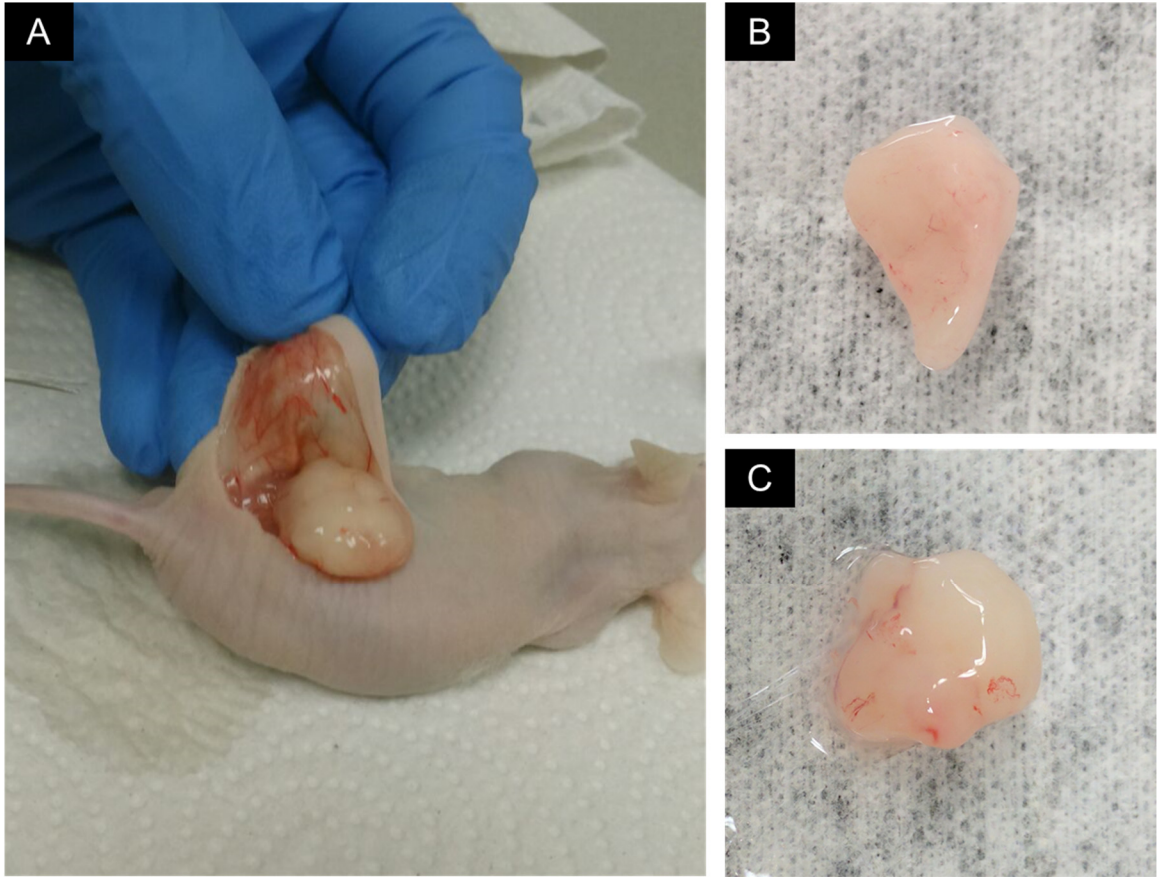
Figure 54: Images of *in vivo* PC-3 tumors excised from an athymic nude mouse. *(A) A G1 tumor is shown on the flank of an athymic nude mouse during the excision process. (B) and (C) Examples of the variety of shapes and sizes PC-3 tumors were found to exhibit post-excision.*

Upon excision, the PC-3 tumors were sectioned into samples from the geometric core, midpoint, and periphery, similar in geometry to the bioengineered tumor tissues. Depending on tumor size, approximately 3 samples from each location were analyzed per tumor resulting in an average total of 9 measurements. As shown in Figure 55, G1 tumor samples did not consistently follow the hypothesis that the geometric core would represent the necrotic core and yield the lowest Young's modulus, while the geometric periphery

would represent the proliferative region and yield the highest Young's modulus, and the geometric midpoint and quiescent zone would fall in the middle. The core stiffness was relatively uniform, whereas the midpoint and periphery were not. Furthermore, very large standard deviations were observed, thus confirming the extensive intratumoral spatial heterogeneity found *in vivo*.
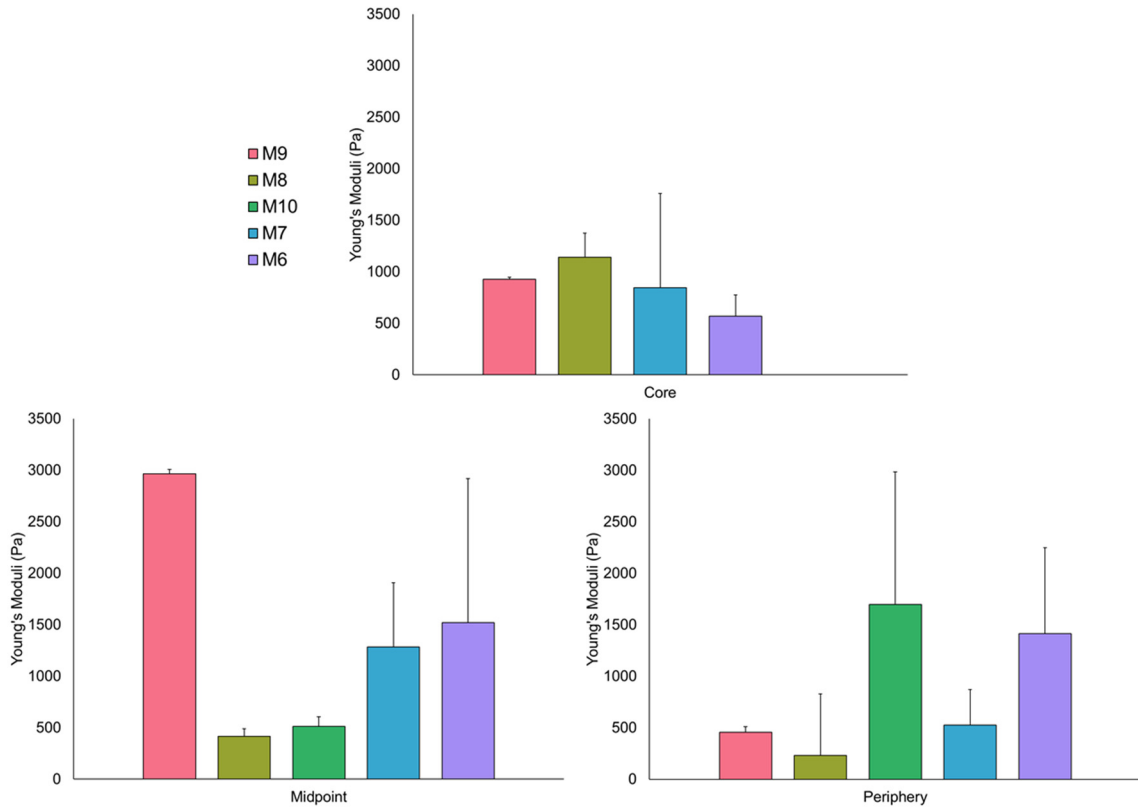
Figure 55: The Young's moduli of G1 *in vivo* tumor samples. *A wide range of mechanical stiffness was observed in the midpoint and periphery of G1 tumors, whereas the core presented more uniform values. Young's moduli values are presented by increasing final tumor volume from left to right. It is important to note that a core sample could not be collected from Mouse 10. (Error bars represent a population based standard deviation, n = 3 samples from each geometric location from each tumor)*
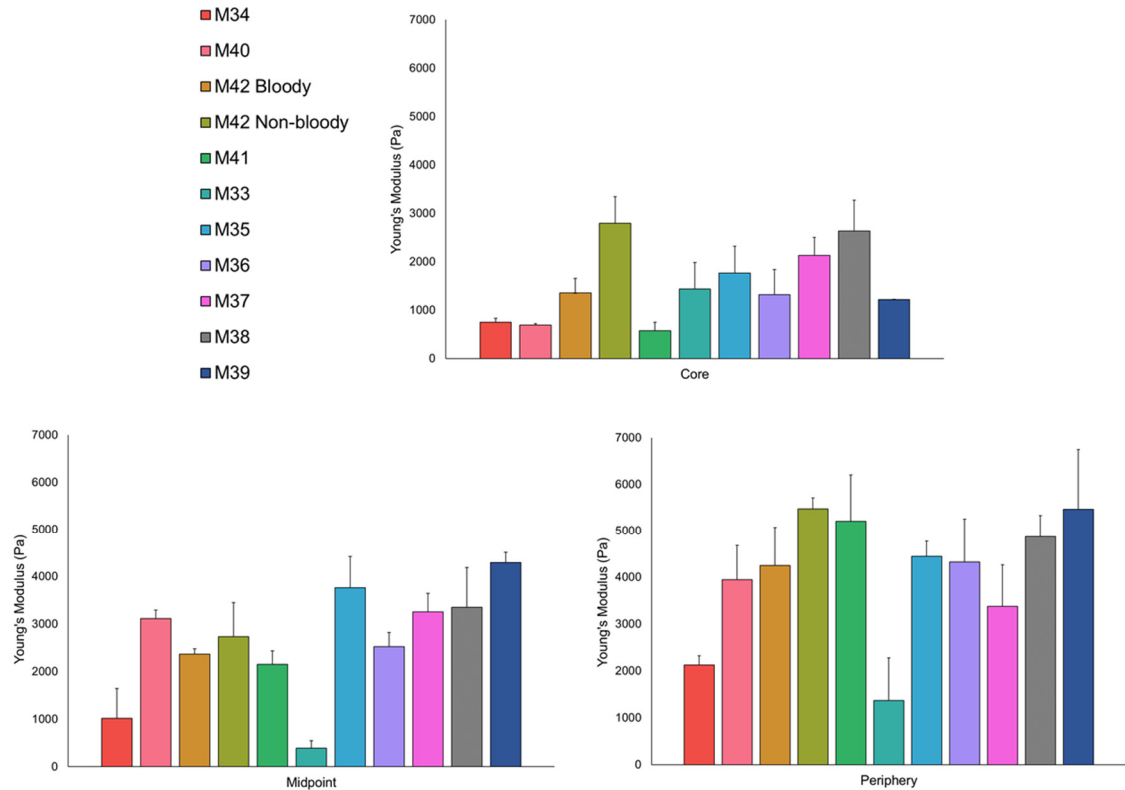
Figure 56: The Young's moduli of G2 *in vivo* tumor samples. *A wide range of mechanical stiffness was observed in the core, midpoint and periphery of G2 tumors. Young's moduli values are presented by increasing final tumor volume from left to right. It is important to note that tissue samples from Mouse 42 were continuously less stiff in the bloody region than the non-bloody region. (Error bars represent a population based standard deviation, n = 3 samples from each geometric location from each tumor)*

Overall, G2 tumors were found to more closely follow the hypothesized increase in mechanical stiffness following locational progression from the geometric core to the geometric midpoint to the geometric periphery. However, as shown in Figure 56, the Young's moduli were found to present a wide distribution, thus confirming intertumoral heterogeneity between mice. Surprisingly, smaller standard deviations were noted in G2

tumors than G1 tumors, thus indicating more homogenous microarchitectural environments within the three geometric regions.

Further evaluation of the G1 and G2 *in vivo* tumor mechanical stiffness revealed a more narrow Young' modulus distribution in G1 than in G2, as shown in Figure 57. Furthermore, G2 tumors were stiffer than G1 tumors at all three geometric locations. It is important to note that *in vitro* bioengineered tumor tissues must be able to mimic the full range of Young's moduli shown in Figures 55 through 57 to accurately recapitulate the native tumor microarchitecture.
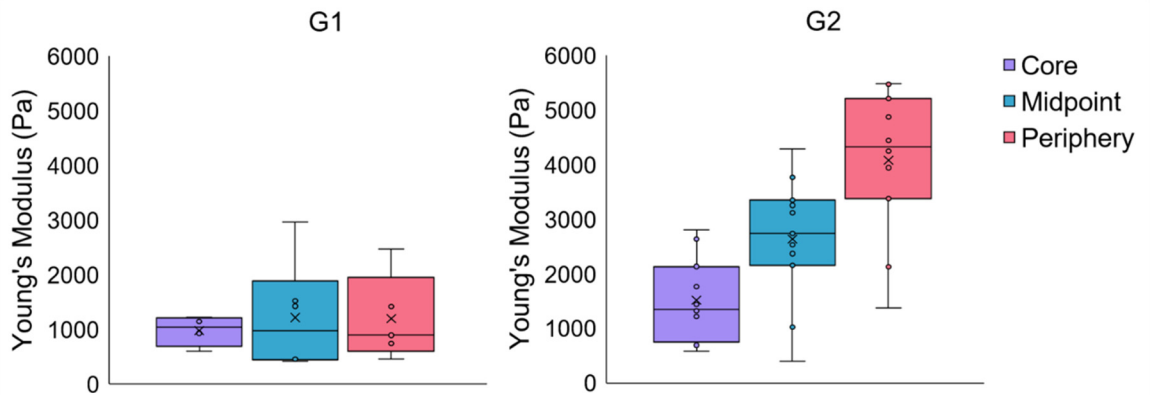
Figure 57: The range of Young's moduli observed in G1 and G2 *in vivo* PC-3 tumors. *Box and whisker plots illustrate the distribution of collected values, emphasizing the mean, median, upper and lower quartiles, and highest and lowest observations. (n = 15 samples per location in G1, n = 33 samples per location in G2)*

PC-3 and BJ-5ta coculture bioengineered tumor tissues comprised of PF, PF+1%PEG, and PF+2%PEG were shown to accurately recapitulate the range of stiffnesses quantified in G1 *in vivo* tumors, as illustrated in Figures 58 and 59. However, unfortunately, the G2 tumor stiffness exceeded the achievable range, as shown in Figure

59. Ongoing studies are currently being conducted to monitor encapsulated cell behavior and quantify the Young's modulus of PF+3%PEG bioengineered tumor tissues.
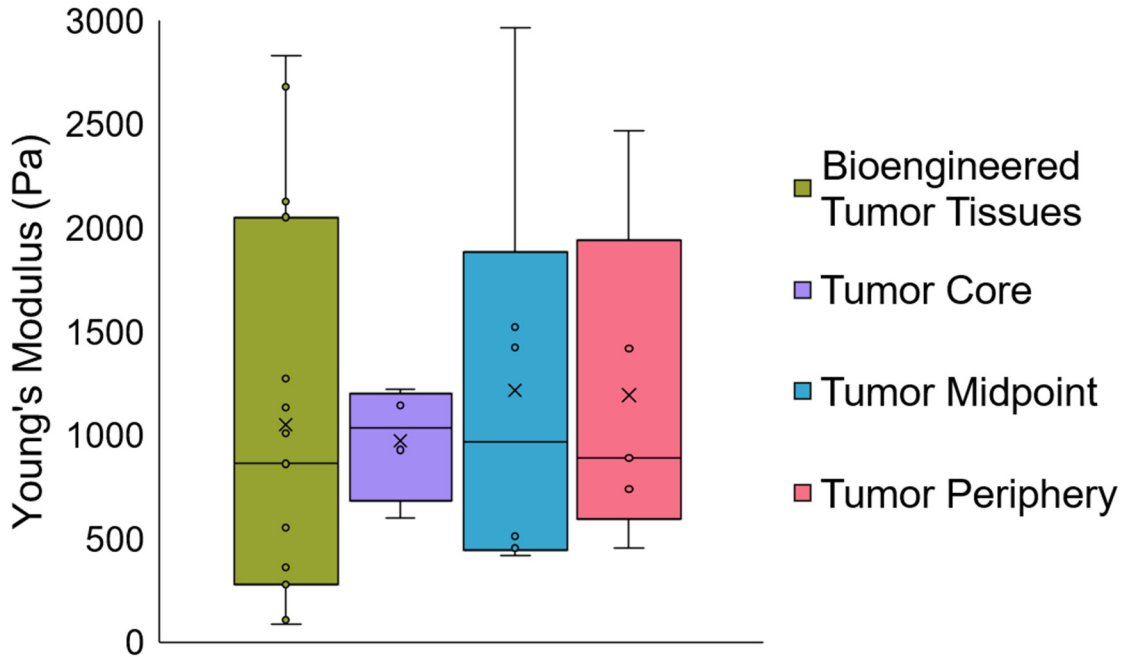
Figure 58: *In vitro* **bioengineered PC-3 and BJ-5ta tumor tissues are able to accurately recapitulate the G1** *in vivo* **tumor stiffness range.** *Box and whisker plots illustrate the distribution of collected values, emphasizing the mean, median, upper and lower quartiles, and highest and lowest observations. (n = 45 bioengineered tumor samples, n = 15 samples per tumor location)*
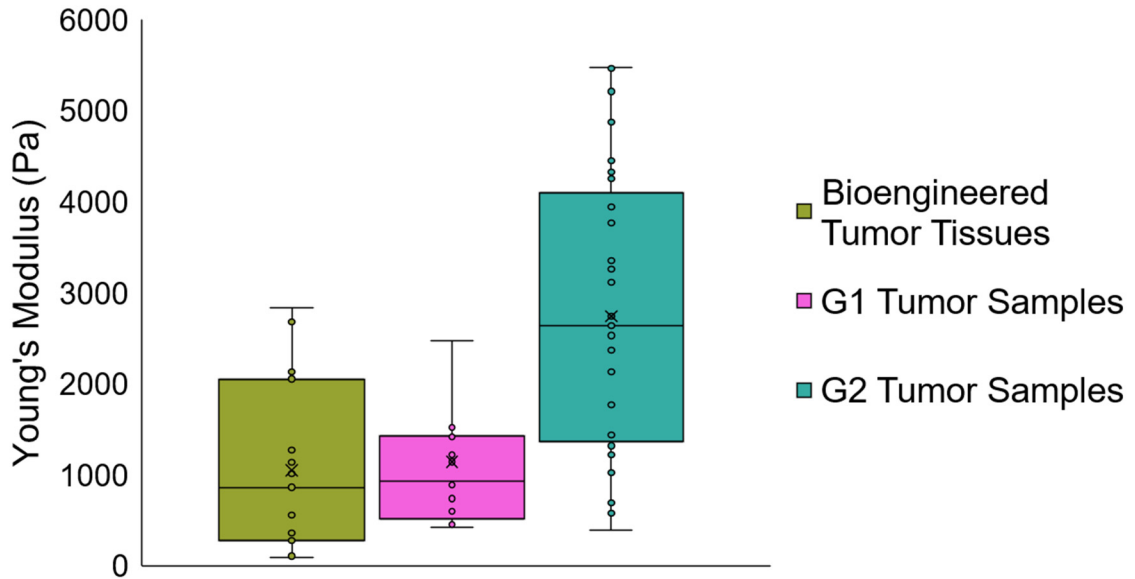
Figure 59: G2 *in vivo* PC-3 tumors are found to exceed the range of achievable bioengineered tumor tissue stiffness. *Box and whisker plots illustrate the distribution of collected values, emphasizing the mean, median, upper and lower quartiles, and highest and lowest observations. (n = 45 bioengineered tumor and G1 tumor samples, n = 99 G2 tumor samples)*

3.4. Conclusions

Overall, modulating the mechanical properties of PF based bioengineered tumor tissues through the addition of excess PEGDA proved to be an appropriate method to augment the biomimicry of the *in vitro* model. Modulations in the polymer composition of the biomaterial scaffold did not significantly affect encapsulated cell behavior including cell adhesion, proliferation, colonization, and migration. PC-3 and BJ-5ta cells were found to maintain greater than 80% viability over increased culture time in PF, PF+1%PEG, and PF+2%PEG. Furthermore, appropriate circular cancer cell morphology was observed in all

three polymer compositions, with an even cell type distribution throughout the bioengineered tumor tissue.

Young's moduli quantification revealed a statistically significant increase in mechanical stiffness on days 8, 15, 22, and 29 post-encapsulation between PF and both PF+1%PEG and PF+2%PEG. Bioengineered tumor tissues on days 15 were also found to exhibit statistically significant variations between PF+1%PEG and PF+2%PEG. Overall, a modulus range of approximately 50 Pa to 2800 Pa was found to be achievable within PF based bioengineered tumor tissues through modulation of culture duration and polymer scaffold composition.

In vivo PC-3 tumors were successfully produced through the subcutaneous injection of cancer cells in athymic nude mice. Resultant tumor masses were excised and sectioned for quantification of *in vivo* tissue stiffness. G1 tumors were found to be softer than G2 tumors, with little to no spatial variation in mechanical stiffness in regard to geometric region. Conversely, G2 tumors were found to exhibit increasing stiffness with an increasing locational progression from the core to the midpoint to the periphery of the mass.

Bioengineered tumor tissues were found to accurately recapitulate the full mechanical stiffness range of G1 tumors through the modulation of polymer scaffold composition. However, G2 tumors were found to exceed this achievable range at the geometric midpoint and periphery. Ongoing experiments are currently being performed utilizing 3% (w/v) excess PEGDA to increase the maximum Young's modulus attainable by the PC-3 and BJ-5ta coculture bioengineered tumor tissues.

A Bioengineered Colorectal Tumor Tissue Model Utilizing Patient-Derived Xenografts for 3D *In Vitro* Conservation of the Native Tumor Cell Population

Chapter 4.   3D Culture of Colorectal Cancer Patient-Derived Xenograft Cells in PEG-fibrinogen Based Hydrogels

4.1. Introduction

It is widely accepted that naturally occurring tumors *in vivo* exhibit genotypic and phenotypic heterogeneities not only intertumorally between cancer types, but also intertumorally between patients with the same type of cancer.[7,26,27] As a result, patients are often found to exhibit drastically different responses to the same anti-cancer therapeutic, thus exemplifying the immense need for personalized medicine in the field of clinical oncology. While this can be attempted through patient-specific therapeutic targeting mechanisms, preclinical anti-cancer therapeutic testing models can also be modified to employ patient-derived tumor cells.[113]

This study reports the development of a 3D PF based *in vitro* colorectal cancer tumor model utilizing patient-derived xenografts from patients diagnosed with stage II, III-B, and IV CRC adenocarcinomas. Through the implementation of PDX methodology, it is important to note that a more complete tumor and stromal cell cadre containing both mouse and human cells is employed in the investigation. Flow cytometry was performed to monitor and quantify changes in the human, CRC, and proliferative cell population over 29 days of 2D and 3D culture. Overall, these findings can be utilized to assess the ability

of the PF based bioengineered CRC tumor tissue model to maintain important cell populations of interest from the initial dissociated PDX tumor.

4.2. Materials and Methods

All chemicals were acquired from Sigma-Aldrich (St. Louis, MO) unless stated otherwise.

4.2.1. PEGDA Synthesis and Characterization

PEGDA was synthesized according to established protocols.[106] 10kDA molecular weight PEG was reacted with acryloyl chloride (1:4 molar ratio) in anhydrous dichloromethane with triethylamine (1:2 molar ratio) under argon overnight at 25 ºC. The resultant PEGDA was purified through phase separation with 2M potassium carbonate. The organic phase, containing PEGDA, was dried using anhydrous magnesium sulfate and subsequently filtered. Finally, the synthesized PEGDA was precipitated utilizing diethyl ether, again filtered, and dried overnight under vacuum at 25 ºC. ^{1}H NMR was performed to characterize the degree of acrylation achieved during synthesis. PEGDA was stored at -20 ºC.

4.2.2. PEG-fibrinogen Synthesis and Characterization

PF was synthesized according to established protocols.[70] Bovine fibrinogen was dissolved in an 8M urea solution in 10mM PBS at a final concentration of 7 mg/mL. TCEP-HCl was added to the solution at a TCEP to fibrinogen cysteine molar ratio of 1.5:1. The final solution pH was adjusted to 8.0. Synthesized PEGDA was also dissolved and subsequently centrifuged in an 8M urea in 10mM PBS buffer solution at a final concentration of 280 mg/mL. The PEGDA solution was slowly added to the fibrinogen

solution, and the consequent reaction was allowed to proceed under dark conditions for 3 hours at 25 ºC. The reaction solution was next diluted with an equal volume of the urea-PBS buffer solution and precipitated through the addition of acetone at a 4:1 volumetric ratio of acetone to reaction solution. The precipitate product was separated from the liquid phase via centrifugation, weighed, and re-dissolved in the urea-PBS buffer at a final concentration of 2.2 mL buffer per gram of precipitate. The product solution was then dialyzed against 1L sterile PBS three times over a period of 24 hours under dark conditions at 4 ºC. The final PF product was aliquoted into sterile microcentrifuge tubes and stored at -80 ºC. A standard Pierce™ BCA Protein Assay Kit (Thermo Fisher Scientific, Rockford, IL) was utilized to characterize the protein concentration of the synthesized PF.

4.2.3. PDX Tumor Dissociation and Cell Culture

PDX tumors were propagated in collaboration with Dr. Michael Greene (Department of Nutrition, Dietetics, and Hospitality Management, Auburn University) by subcutaneously injecting 5×10^6 patient CRC cells suspended in DMEM at a 1:1 ratio with sterile Matrigel (CAT#: 354230, BD Biosciences, Inc., Franklin Lakes, NJ) into the flank of NOD-SCID mice; after three passages, biopsies of the PDX CRC tumor were orthotopically implanted into RAG1 mice. Tumor growth was measured twice weekly by utilizing calipers to estimate the length, width and height of the mass; these values were then employed to calculate the approximate tumor volume was calculating utilizing Equation 8 found in *Section 3.2.3.*

Tumors were excised from the host animal at weights ranging from 0.6 g – 1.5 g. Upon excision, the tumor mass was washed with 1X PBS, placed in the dissociation solution (Hank's Balanced Salt Solution (HBSS) (Lonza, Walkersville, MD) with 1 mg/mL

collagenase type IV (CAT#: LS004188, Worthington Biochemical Corporation, Newark, NJ) and 0.015 mg/mL deoxyribonuclease I (DNAse) with an activity of 2910 Kunitz units/mg, or equally 200 Kunitz units/mL, (CAT#:LS002139, Worthington Biochemical Corporation, Newark, NJ)) and minced with a scalpel. The tumor fragments were then suspended in dissociation solution and incubated in a water bath at 37 °C for 30 minutes with slight agitation every 10 minutes to disperse the fragments. Upon completion of the incubation time, the supernatant was removed and placed in a separate centrifuge tube in the water bath, while the tumor fragments were resuspended in dissociation solution. This process was repeated until complete tissue dissociation was achieved. Subsequently, the combined supernatant from each of the dissociation steps was filtered through a 40 μm Falcon® cell strainer (Corning®, Corning, NY) and then centrifuged for 5 minutes at 300 g. The resultant cell pellet was resuspended in 10 mL of HBSS, recentrifuged, and washed with yet another 10 mL of HBSS six times.

The resultant CRC PDX cells were then either encapsulated for 3D culture in PF hydrogels or plated for 2D culture in plasma-treated polystyrene tissue-culture flasks, stored in a humidified atmosphere with 5% CO_2 and a constant temperature of 37 ºC, and maintained utilizing DMEM (Lonza, Walkersville, MD) containing 4 mM L-glutamine, 4.5 g/L glucose and 1.5 g/L sodium bicarbonate, supplemented with 1% (v/v) 200mM glutaGRO™ (Corning®, Corning, NY), 10% FBS (Atlanta Biologicals, Flowery Branch, GA), and 1% (v/v) Pen-Strep (GE Healthcare Bio-Sciences, Pittsburgh, PA). Culture media was renewed twice weekly.

4.2.4. Cell Encapsulation in PF Hydrogels

Bioengineered PDX tumor tissues were formed in cylindrical shaped PDMS molds, which were prefabricated for use in the encapsulation process. PDMS sheets were constructed utilizing the SYLGARD 184 Elastomer Kit (Thermo Fisher Scientific, Rockford, IL) and shaped utilizing a 4 mm diameter biopsy punch. PDMS molds were firmly adhered to the bottom of a 6-well polystyrene plasma treated tissue-culture plate to prevent leakage of the cell-laden hydrogel precursor solution. The hydrogel precursor solution was prepared by adding 1.5% (v/v) TEOA, 37 mM NVP, and 0.1 mM Eosin Y as a photoinitiator to the synthesized PF in solution with 1X PBS.

To encapsulate cells within the hydrogel scaffold, dissociated PDX cells were counted utilizing a hemocytometer with 0.4% Trypan Blue (Lonza, Walkersville, MD) and resuspended in the hydrogel precursor solution at a concentration of 20×10^6 cells/mL. A volume of 10 μL of the cell-laden hydrogel precursor solution was pipetted into each PDMS mold well and photocrosslinked via high-intensity visible light exposure (light intensity: 203 mW/cm^2) for 2 minutes. Upon crosslinking completion, the PDMS mold was carefully peeled back from the well plate surface, thus leaving behind disc-shaped, bioengineered PDX tumor tissues. Appropriate culture media was added to the well plate, which was finally stored in a humidified atmosphere with 5% CO_2 and a constant temperature of 37 ºC; culture media was renewed twice weekly.

4.2.5. Cell Population Investigation

Flow cytometry was performed to quantify cell populations both in 2D culture and in 3D bioengineered PDX tumor tissues on days 8, 15, 22, and 29 post-tumor dissociation. Day 1 samples are representative of the initial cell populations found in the dissociated

CRC PDX tumor. Zombie Green™ (BioLegend®, San Diego, CA) was utilized to positively label dead cells and cell debris. The Zenon™ R-Phycoerythrin Mouse IgG$_{2a}$ Labeling Kit (CAT#: Z25155, Thermo Fisher Scientific, Rockford, IL) was employed with either the Anti-Human Beta-2-Microglobulin (B2M) (CAT#: BM604S, OriGene Technologies Inc., Rockville, MD) antibody at a 1:2500 dilution to positively label all human cells or the mouse Anti-Mouse major histocompatibility complex (MHC) Class I H-2 Db (H2Db) (CAT#: AM08080PU-N, OriGene Technologies Inc., Rockville, MD) antibody at 0.4 μg/mL to positively label all mouse cells. The Zenon™ Alexa Fluor™ 647 Rabbit IgG Labeling Kit (CAT#: Z25308, Thermo Fisher Scientific, Rockford, IL) was utilized with both the Anti-Ki67 (CAT#: ab15580, Abcam, Cambridge, MA) antibody at a 1:2000 dilution and the Anti-Keratin 20 D9Z1Z XP® (CK20) (CAT#: 13063S, Cell Signaling Technology, Danvers, MA) antibody at a 1:500 dilution to positively label proliferative cells and human colon adenocarcinoma cells, respectively. Furthermore, isotype controls were performed utilizing the antibody Mouse IgG$_{2a}$ Isotype Control (MSIgG$_{2a}$), kindly provided by Dr. Michael Greene (Department of Nutrition, Dietetics, and Hospitality Management, Auburn University), at a 1:500 dilution with the Zenon™ R-Phycoerythrin Mouse IgG$_{2a}$ Labeling Kit, and the antibody Rabbit IgG Isotype Control (RbIgG) (CAT#: 02-6102, Thermo Fisher Scientific, Rockford, IL) at a 1:1000 dilution with the Zenon™ Alexa Fluor™ 647 Rabbit IgG Labeling Kit. Unstained single cell suspensions were also analyzed to monitor cell auto-fluorescence, as well as auto-fluorescence from the Eosin Y photoinitiator used in the PF photocrosslinking procedure.

The 2D CRC PDX cells were enzymatically detached from the surface of the flask in preparation for staining; it is important to note that the initial cell culture media was

preserved and centrifuged along with the enzymatically detached cells to preserve both adherent and non-adherent cell types. Bioengineered PDX tumor tissues were dissociated at 37 ºC utilizing collagenase type IV (CAT#: LS004188, Worthington Biochemical Corporation, Newark, NJ) at a concentration of 1 mg/mL in 1X PBS for 1 hour, or until completely dissociated. Forced pipetting was also used to aid the degradation of the polymer matrix. The cell suspension solution was centrifuged at 300 g for 5 minutes with the brake off and resuspended in Accumax (Innovative Cell Technologies, Inc., San Diego, CA) for 15 minutes to yield single cells. 2D and 3D culture CRC PDX cells were re-centrifuged, washed with 1X PBS, centrifuged again, and resuspended in Zombie Green™ at a 1:1000 dilution in 1X PBS and incubated at 4 ºC in the dark for 30 minutes. Cells were washed with 0.2 μm filtered blocking buffer (10% FBS and 1% BSA in 1X PBS), centrifuged, resuspended in blocking buffer, and incubated for 30 minutes at 4 ºC in the dark. The Zenon™ R-Phycoerythrin-B2M, Zenon™ R-Phycoerythrin-H2Db, or Zenon™ R-Phycoerythrin-MSIgG$_{2a}$ extracellular staining solution was subsequently added and followed by another 30-minute incubation at 4 ºC in the dark. Finally, eBioscience™ Foxp3 Fixation/Permeabilization (Foxp3) (Invitrogen, Carlsbad, CA) working solution was added to the samples and incubated at 4 ºC in the dark overnight.

The next day, samples were centrifuged, washed with 1X permeabilization buffer (Invitrogen, Carlsbad, CA), resuspended in FACS buffer (10% FBS and 1% BSA in 1X permeabilization buffer), and allowed to incubate in the dark at 25 °C for 30 minutes. The Zenon™ Alexa Fluor™ 647-CK20, Zenon™ Alexa Fluor™ 647-Ki67, or Zenon™ Alexa Fluor™ 647-RBIgG intracellular staining solution was subsequently added and followed by another 30-minute incubation at 25 °C in the dark. Stained cells were washed with 1X

permeabilization buffer twice, resuspended in blocking buffer at a concentration of approximately 1×10^6 cells/mL, and finally passed through a 40 μm Flowmi™ Cell Strainer filter.

The stained cell population was quantified utilizing an Accuri™ C6 (BD Biosciences, Franklin Lakes, NJ) personal flow cytometer according to manufacturer instructions. The analysis was stopped after the incidence of 20,000 events within gating that excluded positively labeled Zombie Green™ cells, as well as size-excluded small debris and PF particles. Results were analyzed, and event gating was performed utilizing FlowJo® (FlowJo, LLC, Ashland, OR) software.

4.3. Results and Discussion

4.3.1. Effect of Culture Dimensionality on PDX Cell Populations

Temporal variations in human, CRC, and proliferative cell populations as a result of maintenance in 2D or 3D culture were quantified through the use of immunolabeling and subsequent flow cytometry. A positive CK20 label indicates a CRC cell, a positive B2M label indicates a human cell, a positive H2Db label indicates a mouse cell, and finally a positive Ki67 label indicates a proliferative cell. As shown in Figures 60 and 61, Stage II PDX cells cultured in 2D polystyrene flasks exhibited a decrease in both CK20 positive CRC cells, as well as B2M positive human cells, arguably the two most important cell populations provided by the PDX tumor. Conversely, 3D PF microspheres were found to not only maintain the initial proportion of human and CRC cells, but also provided an appropriate scaffold to support proliferation of these two populations. Culture dimensionality was not found to produce a significant effect on overall encapsulated cell

proliferation, however, when considered alongside the findings presented in Figures 60 and 61, it can be concluded that mouse cells were found to experience higher proliferation in 2D culture while human cells were found to experience higher proliferation in 3D culture. This unexpected finding further validates the PF based PDX model as an appropriate platform for implementation in personalized *in vitro* anti-cancer therapeutic testing.
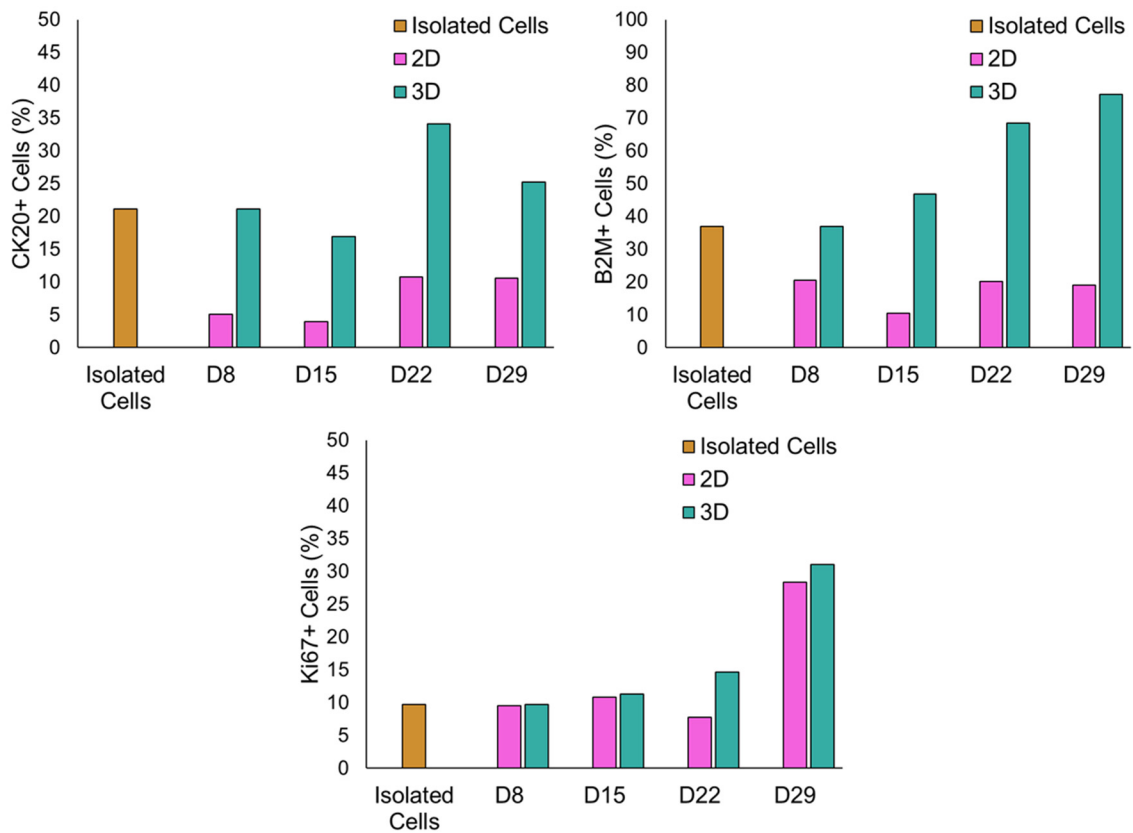
Figure 60: Variations in stage II PDX CRC cell populations with respect to culture dimensionality. *CK20 positive CRC cell populations and B2M positive human cell populations were found to be better maintained throughout long-term culture in 3D PF microspheres than 2D polystyrene cell culture flasks. Culture dimensionality was not found to have a significant effect on the proliferative cell population. CK20+ label indicates CRC cells, B2M+ label indicates human cells, Ki67+ label indicates proliferative cells.*
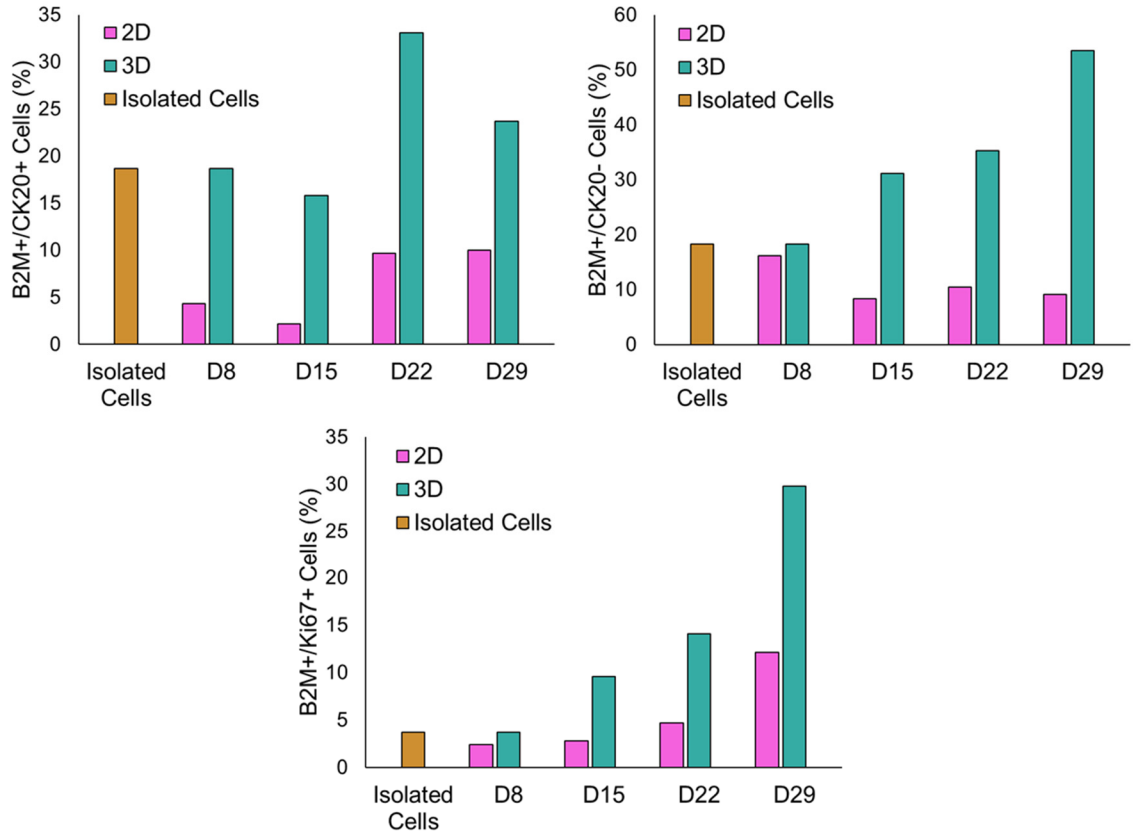
Figure 61: Variations in dual-labeled stage II PDX CRC cell populations with respect to culture dimensionality. *Human CRC cells are shown to be better maintained in 3D PF microsphere culture than 2D culture. A similar trend was noted in human non-CRC cell populations. Finally, human cells were shown to be significantly more proliferative in 3D culture than in 2D culture. B2M+/CK20+ labels indicate human CRC cells, B2M+/CK20- labels indicate human non-CRC cells, B2M+/Ki67+ labels indicate human proliferative cells.*

4.4. Conclusions

Overall, CRC PDX cell populations of interest derived from a stage II colorectal adenocarcinoma were found to be better maintained in 3D PF microsphere culture than on 2D polystyrene culture flasks. Notably, positively labeled human CRC and non-CRC cell populations were found to not only maintain a baseline level of their preliminary proportions, but also expand over 29 days in *in vitro* culture. These significant findings ascertain a strong correlation between isolated *in vivo* PDX tumor cells and dissociated *in vitro* PDX hydrogel cells. Therefore, further validating the PF based CRC PDX bioengineered tumor tissues as a viable *in vitro* model for personalized anti-cancer therapeutic screening.

Summary and Future Directions

This investigation demonstrates the development of a hybrid biomaterial based, three-dimensional coculture tumor model for improved *in vitro* recapitulation of the native tumor microenvironment and future application in preclinical anti-cancer therapeutic development processes. PEG-based hydrogels were functionalized for cell adhesion and cell-mediated degradation through the introduction of fibrinogen into the polymer matrix. Cancer cells, along with supporting stromal cell types, were suspended in the polymer precursor solution and photocrosslinked under high intensity visible light to form cell-laden bioengineered tumor tissues. A myriad of characterization experiments were then performed to evaluate the degree of biomimicry achieved by the *in vitro* tumor model.

The work presented in this thesis is divided in to three major studies, with each serving to assess the ability of the PF bioengineered tumor tissues to accurately recapitulate a specific characteristic of the native TME. In the first study, the aggressively metastatic PC-3 prostate cancer cell line was encapsulated within PF hydrogels in a variety of cell ratios with BJ-5ta stromal fibroblasts and maintained in coculture for a period of 29 days. Notably, the encapsulated cells were found to remodel their microenvironment over increasing culture time, as well as colonize, proliferate, migrate, and exhibit appropriate morphology throughout the polymeric scaffold. Furthermore, a cell line comparison study was performed utilizing the more indolent LNCaP prostate cancer cells, which were appropriately found to exhibit less aggressive behavior than the PC-3 cell line.

The second study aimed to further augment the physiological relevancy of the coculture PF bioengineered tumor tissues by modulating mechanical characteristics of the polymeric matrix to mimic the *in vivo* prostate tumor microarchitecture. In support of this, PC-3 tumors were induced in partially immunocompromised mice and subsequently characterized to quantify the mechanical stiffness of the tissue and provide an *in vivo-in vitro* comparison. Through the addition of excess PEGDA, bioengineered tumor tissues were appropriately stiffened to recapitulate the wide range of naturally observed rigidity.

Overall, the notable findings from the first two studies demonstrate significant potential for more accurate *in vitro* recapitulation of the complex native tumor microenvironment, as compared to traditional 2D or cell aggregate models. In future work, it is recommended that the bioengineered prostate tumor tissues be additionally characterized through ECM analysis, additional fluorometric or BCA assays to identify proteinase excretion, and immunohistochemical staining. Furthermore, the complexity of bioengineered prostate tumor tissues can be improved through the employment of additional or more representational cell types such as tumor associated macrophages, tumor associated fibroblasts, or dissociated PDX tumor cells. Finally, it is recommended that the mechanical stiffness of soft-tissue prostate tumor metastases from human cancer patients be quantified to provide a more consequential *in vivo-in vitro* microarchitectural comparison.

In the third study, cells from a patient-derived stage II colorectal adenocarcinoma xenograft were encapsulated both within the PF matrix, as well as on 2D cell culture flasks, and maintained for a period of 29 days. Notably, the PF based 3D microspheres were found to sustain PDX cell populations of interest significantly better than 2D polystyrene flasks

throughout long-term culture. These findings serve to assist in the validation of the bioengineered CRC PDX tumor tissues as an appropriate *in vitro* model for personalized anti-cancer therapeutic screening.

It is recommended that the physiological relevancy of both the cell line and PDX bioengineered tumor tissues be further augmented through extension to a microfluidic chip-based platform. Ongoing studies aim to achieve this through collaboration with SynVivo, Inc. (Huntsville, AL). To best mimic the complexity of a native tumor, proposed microfluidic chip designs are comprised of a microvascular network derived from *in vivo* computerized tomography (CT) images of rodent vasculature with added tumor tissue chambers and leaky vessels, as shown in Figure 62.[114,115] These patterns recapitulate the tortuous geometries and bifurcations of the pathophysiological vasculature and expose the bioengineered tumor to varying shear flow and drug concentration gradients, similar to those experienced by tumors *in vivo*. Human umbilical vein endothelial cells (HUVECs) are seeded into the microvascular network and held under dynamic flow conditions to form a lumenized endothelium, and thus introduce another cell type to the tumor model. Bioengineered tumor tissues are encapsulated within the primary tumor chamber, while the secondary and tertiary tumor chambers are left empty to monitor cancer cell invasion and metastasis to distal locations via intravasation and extravasation. Thus, the microfluidic chip platform not only demonstrates significant potential for accurate prediction of anti-cancer therapeutic efficacy, but also serves to model the tumorigenic process *in vitro*.

In conclusion, the notable findings presented in this thesis reveal significant advancement in *in vitro* modeling of the native TME. Through the amalgamation of this study with the proposed future work, this research will bridge the gap between preclinical

and clinical trials during the drug development process and result in the production of safer

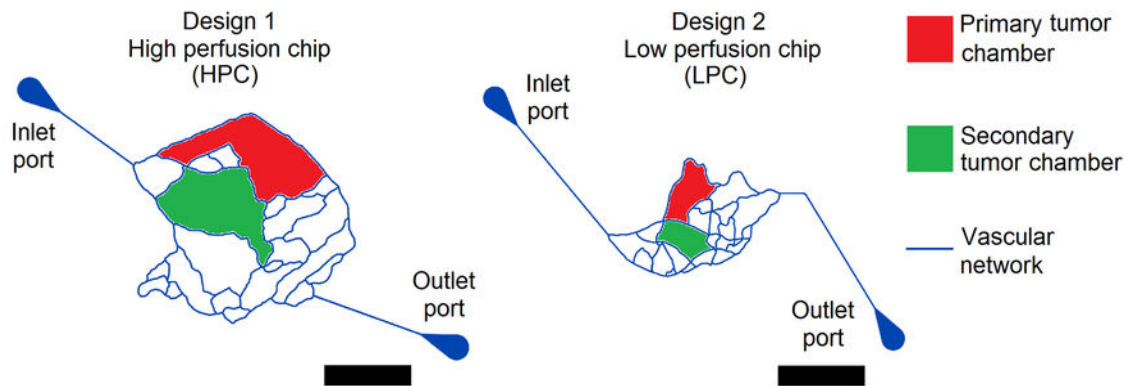and more efficacious anti-cancer therapeutics.

Figure 62: SynVivo microfluidic chip platform design. *The high-perfusion (HPC) and low-perfusion (LPC) microfluidic chip platform designs are comprised of a microvascular network derived from CT images of in vivo rodent vasculature with added primary and secondary tumor tissue chambers. (Scale bar = 5 mm) (Reprinted with permission from Pradhan et al. 2018)*

References

1   American Cancer Society. *Early History of Cancer* <https://www.cancer.org/cancer/cancer-basics/history-of-cancer/what-is-cancer.html > (2018).

2   National Cancer Institute. *Cancer Statistics* <https://www.cancer.gov/about-cancer/understanding/statistics> (2017).

3   International Agency for Research on Cancer. World Cancer Report. (World Health Organization 2014).

4   Vogelstein, B. & Kinzler, K. W. Cancer genes and the pathways they control. *Nature Medicine* **10**, 789, doi:10.1038/nm1087 (2004).

5   Hanahan, D. & Weinberg, R. A. The Hallmarks of Cancer. *Cell* **100**, 57-70, doi:https://doi.org/10.1016/S0092-8674(00)81683-9 (2000).

6   Hanahan, D. & Weinberg, Robert A. Hallmarks of Cancer: The Next Generation. *Cell* **144**, 646-674, doi: https://doi.org/10.1016/j.cell.2011.02.013 (2011).

7   Burrell, R. A., McGranahan, N., Bartek, J. & Swanton, C. The causes and consequences of genetic heterogeneity in cancer evolution. *Nature* **501**, 338, doi:10.1038/nature12625 (2013).

8   Whiteside, T. L. The tumor microenvironment and its role in promoting tumor growth. *Oncogene* **27**, 5904, doi:10.1038/onc.2008.271 (2008).

9   National Institute of Biomedical Imaging and Bioengineering. *Tissue Engineering and Regenerative Medicine*, <https://www.nibib.nih.gov/science-education/science-topics/tissue-engineering-and-regenerative-medicine> (2018).

10   Horch, R. E. *et al.* Cancer research by means of tissue engineering – is there a rationale? *Journal of Cellular and Molecular Medicine* **17**, 1197-1206, doi:10.1111/jcmm.12130 (2013).

11   Pharmaceutical Research and Manufacturers of America. Drug Discovery and Development. (2007).

12   US Food & Drug Administration. *The Drug Development Process* <https://www.fda.gov/ForPatients/Approvals/Drugs/default.htm> (2018).

13   Biotechnology Innovation Organization. Clinical Development Success Rates 2006-2015. (2016).

14   Breslin, S. & O'Driscoll, L. The relevance of using 3D cell cultures, in addition to 2D monolayer cultures, when evaluating breast cancer drug sensitivity and resistance. *Oncotarget* **7**, 45745-45756, doi:10.18632/oncotarget.9935 (2016).

15   Myungjin Lee, J. *et al.* A three-dimensional microenvironment alters protein expression and chemosensitivity of epithelial ovarian cancer cells in vitro. *Laboratory Investigation* **93**, 528, doi:10.1038/labinvest.2013.41 https://www.nature.com/articles/labinvest201341#supplementary-information (2013).

16   Chauhan, V. P., Stylianopoulos, T., Boucher, Y. & Jain, R. K. Delivery of Molecular and Nanoscale Medicine to Tumors: Transport Barriers and Strategies.

Annual Review of Chemical and Biomolecular Engineering **2**, 281-298, doi:10.1146/annurev-chembioeng-061010-114300 (2011).

17   Minchinton, A. I. & Tannock, I. F. Drug penetration in solid tumours. *Nat Rev Cancer* **6**, 583-592, doi:10.1038/nrc1893 (2006).

18   Das, V. *et al.* Pathophysiologically relevant in vitro tumor models for drug screening. *Drug Discovery Today* **20**, 848-855, doi:https://doi.org/10.1016/j.drudis.2015.04.004 (2015).

19   Imamura, Y. *et al.* Comparison of 2D- and 3D-culture models as drug-testing platforms in breast cancer. *Oncol Rep* **33**, 1837-1843, doi:10.3892/or.2015.3767 (2015).

20   Katt, M. E., Placone, A. L., Wong, A. D., Xu, Z. S. & Searson, P. C. In Vitro Tumor Models: Advantages, Disadvantages, Variables, and Selecting the Right Platform. *Front Bioeng Biotechnol* **4**, 12, doi:10.3389/fbioe.2016.00012 (2016).

21   Mehta, G., Hsiao, A. Y., Ingram, M., Luker, G. D. & Takayama, S. Opportunities and Challenges for use of Tumor Spheroids as Models to Test Drug Delivery and Efficacy. *Journal of controlled release : official journal of the Controlled Release Society* **164**, 192-204, doi:10.1016/j.jconrel.2012.04.045 (2012).

22   Denayer, T., Stöhr, T. & Van Roy, M. Animal models in translational medicine: Validation and prediction. *New Horizons in Translational Medicine* **2**, 5-11, doi:https://doi.org/10.1016/j.nhtm.2014.08.001 (2014).

23   Kersten, K., de Visser, K. E., van Miltenburg, M. H. & Jonkers, J. Genetically engineered mouse models in oncology research and cancer medicine. *EMBO Molecular Medicine* **9**, 137-153, doi:10.15252/emmm.201606857 (2017).

24   Singh, V. P. *et al.* Critical evaluation of challenges and future use of animals in experimentation for biomedical research. *International Journal of Immunopathology and Pharmacology* **29**, 551-561, doi:10.1177/0394632016671728 (2016).

25   Junttila, M. R. & de Sauvage, F. J. Influence of tumour micro-environment heterogeneity on therapeutic response. *Nature* **501**, 346, doi:10.1038/nature12626 (2013).

26   Dingli, D., Chalub, F. A. C. C., Santos, F. C., Van Segbroeck, S. & Pacheco, J. M. Cancer phenotype as the outcome of an evolutionary game between normal and malignant cells. *British Journal of Cancer* **101**, 1130-1136, doi:10.1038/sj.bjc.6605288 (2009).

27   Liu, J., Dang, H. & Wang, X. W. The significance of intertumor and intratumor heterogeneity in liver cancer. *Experimental &Amp; Molecular Medicine* **50**, e416, doi:10.1038/emm.2017.165 (2018).

28   Balani, S., Nguyen, L. V. & Eaves, C. J. Modeling the process of human tumorigenesis. *Nature Communications* **8**, 15422, doi:10.1038/ncomms15422 (2017).

29   Yang, L. V. Tumor Microenvironment and Metabolism. *International Journal of Molecular Sciences* **18**, 2729, doi:10.3390/ijms18122729 (2017).

30   Quail, D. F. & Joyce, J. A. Microenvironmental regulation of tumor progression and metastasis. *Nature medicine* **19**, 1423-1437, doi:10.1038/nm.3394 (2013).

31   Cairns, R., Papandreou, I. & Denko, N. Overcoming physiologic barriers to cancer treatment by molecularly targeting the tumor microenvironment. *Mol Cancer Res* **4**, 61-70, doi:10.1158/1541-7786.MCR-06-0002 (2006).

32   Justus, C. R., Dong, L. & Yang, L. V. Acidic tumor microenvironment and pH-sensing G protein-coupled receptors. *Front Physiol* **4**, 354, doi:10.3389/fphys.2013.00354 (2013).

33   Lyssiotis, C. A. & Kimmelman, A. C. Metabolic Interactions in the Tumor Microenvironment. *Trends in Cell Biology* **27**, 863-875, doi:10.1016/j.tcb.2017.06.003 (2017).

34   Milotti, E., Vyshemirsky, V., Sega, M. & Chignola, R. Interplay between distribution of live cells and growth dynamics of solid tumours. *Scientific Reports* **2**, 990, doi:10.1038/srep00990 https://www.nature.com/articles/srep00990 #supplementary-information (2012).

35   Budczies, J. *et al.* The landscape of metastatic progression patterns across major human cancers. *Oncotarget* **6**, 570-583 (2015).

36   Martin, T. A., Ye, L., Sanders, A. J., Lane, J. & Jiang, W. G. in *Metastatic Cancer: Clinical and Biological Perspectives* (ed Rahul Jandial) (Landes Bioscience, 2013).

37   Kalluri, R. & Weinberg, R. A. The basics of epithelial-mesenchymal transition. *The Journal of Clinical Investigation* **119**, 1420-1428, doi:10.1172/JCI39104 (2009).

38   Heerboth, S. *et al.* EMT and tumor metastasis. *Clinical and Translational Medicine* **4**, 6, doi:10.1186/s40169-015-0048-3 (2015).

39   Lam, C. R. I. *et al.* A 3D Biomimetic Model of Tissue Stiffness Interface for Cancer Drug Testing. *Molecular Pharmaceutics* **11**, 2016-2021, doi:10.1021/mp500059q (2014).

40   Baccelli, I. *et al.* Identification of a population of blood circulating tumor cells from breast cancer patients that initiates metastasis in a xenograft assay. *Nature Biotechnology* **31**, 539, doi:10.1038/nbt.2576 https://www.nature.com/ articles/nbt.2576#supplementary-information (2013).

41   Polzer, B. & Klein, C. A. Metastasis Awakening: The challenges of targeting minimal residual cancer. *Nature Medicine* **19**, 274, doi:10.1038/nm.3121 (2013).

42   Lee, K. M., Choi, K. H. & Ouellette, M. M. Use of exogenous hTERT to immortalize primary human cells. *Cytotechnology* **45**, 33-38, doi:10.1007/ 10.1007/s10616-004-5123-3 (2004).

43   Jha, K. K., Banga, S., Palejwala, V. & Ozer, H. L. SV40-Mediated Immortalization. *Experimental Cell Research* **245**, 1-7, doi:https://doi.org/10.1006/excr.1998.4272 (1998).

44   Kaur, G. & Dufour, J. M. Cell lines: Valuable tools or useless artifacts. *Spermatogenesis* **2**, 1-5, doi:10.4161/spmg.19885 (2012).

45   Sharma, S. V., Haber, D. A. & Settleman, J. Cell line-based platforms to evaluate the therapeutic efficacy of candidate anticancer agents. *Nature Reviews Cancer* **10**, 241, doi:10.1038/nrc2820 (2010).

46   Gillet, J.-P., Varma, S. & Gottesman, M. M. The Clinical Relevance of Cancer Cell Lines. *JNCI Journal of the National Cancer Institute* **105**, 452-458, doi:10.1093/jnci/djt007 (2013).

47   Damhofer, H. *et al.* Establishment of patient-derived xenograft models and cell lines for malignancies of the upper gastrointestinal tract. *Journal of Translational Medicine* **13**, 115, doi:10.1186/s12967-015-0469-1 (2015).

48   Jang, J. *et al.* Development of Novel Patient-Derived Preclinical Models from Malignant Effusions in Patients with Tyrosine Kinase Inhibitor–Resistant Clear Cell Renal Cell Carcinoma. *Translational Oncology* **10**, 304-310, doi:https://doi.org/10.1016/j.tranon.2017.01.016 (2017).

49   Cheung, P. F. Y. *et al.* Comprehensive characterization of the patient-derived xenograft and the paralleled primary hepatocellular carcinoma cell line. *Cancer Cell International* **16**, 41, doi:10.1186/s12935-016-0322-5 (2016).

50   Mattern, J., Bak, M., Hahn, E. W. & Volm, M. Human tumor xenografts as model for drug testing. *Cancer Metastasis Rev* **7**, 263-284 (1988).

51   Fong, E. L. *et al.* A 3D in vitro model of patient-derived prostate cancer xenograft for controlled interrogation of in vivo tumor-stromal interactions. *Biomaterials* **77**, 164-172, doi:10.1016/j.biomaterials.2015.10.059 (2016).

52   Choi, S. Y. C. *et al.* Lessons from patient-derived xenografts for better in vitro modeling of human cancer. *Advanced Drug Delivery Reviews* **79-80**, 222-237, doi:https://doi.org/10.1016/j.addr.2014.09.009 (2014).

53   Daniel, V. C. *et al.* A primary xenograft model of small-cell lung cancer reveals irreversible changes in gene expression imposed by culture in vitro. *Cancer Res* **69**, 3364-3373, doi:10.1158/0008-5472.CAN-08-4210 (2009).

54   Zhang, X. *et al.* A renewable tissue resource of phenotypically stable, biologically and ethnically diverse, patient-derived human breast cancer xenograft models. *Cancer Res* **73**, 4885-4897, doi:10.1158/0008-5472.CAN-12-4081 (2013).

55   Lin, D. *et al.* High fidelity patient-derived xenografts for accelerating prostate cancer discovery and drug development. *Cancer Res* **74**, 1272-1283, doi:10.1158/0008-5472.CAN-13-2921-T (2014).

56   Siolas, D. & Hannon, G. J. Patient-derived tumor xenografts: transforming clinical samples into mouse models. *Cancer Res* **73**, 5315-5319, doi:10.1158/0008-5472.CAN-13-1069 (2013).

57   Liu, Z. & Vunjak-Novakovic, G. Modeling tumor microenvironments using custom-designed biomaterial scaffolds. *Current opinion in chemical engineering* **11**, 94-105, doi:10.1016/j.coche.2016.01.012 (2016).

58   Gill, B. J. & West, J. L. Modeling the tumor extracellular matrix: Tissue engineering tools repurposed towards new frontiers in cancer biology. *Journal of Biomechanics* **47**, 1969-1978, doi:https://doi.org/10.1016/j.jbiomech.2013.09.029 (2014).

59   Alemany-Ribes, M. & Semino, C. E. Bioengineering 3D environments for cancer models. *Advanced Drug Delivery Reviews* **79-80**, 40-49, doi:https://doi.org/10.1016/j.addr.2014.06.004 (2014).

60   Duval, K. *et al.* Modeling Physiological Events in 2D vs. 3D Cell Culture. *Physiology* **32**, 266-277, doi:10.1152/physiol.00036.2016 (2017).

61   Gurski, L. A. *et al.* Hyaluronan (HA) interacting proteins RHAMM and hyaluronidase impact prostate cancer cell behavior and invadopodia formation in 3D HA-based hydrogels. *PLoS One* **7**, e50075, doi:10.1371/journal.pone.0050075 (2012).

62   Yu, X. & Machesky, L. M. Cells assemble invadopodia-like structures and invade into matrigel in a matrix metalloprotease dependent manner in the circular invasion assay. *PLoS One* **7**, e30605, doi:10.1371/journal.pone.0030605 (2012).

63   Provenzano, P. P. *et al.* Collagen density promotes mammary tumor initiation and progression. *BMC Med* **6**, 11, doi:10.1186/1741-7015-6-11 (2008).

64   Weigel, T., Schinkel, G. & Lendlein, A. Design and preparation of polymeric scaffolds for tissue engineering. *Expert Review of Medical Devices* **3**, 835-851, doi:10.1586/17434440.3.6.835 (2006).

65   Caliari, S. R. & Burdick, J. A. A Practical Guide to Hydrogels for Cell Culture. *Nature methods* **13**, 405-414, doi:10.1038/nmeth.3839 (2016).

66   Chau, Y. *et al.* Incorporation of a matrix metalloproteinase-sensitive substrate into self-assembling peptides – A model for biofunctional scaffolds. *Biomaterials* **29**, 1713-1719, doi:https://doi.org/10.1016/j.biomaterials.2007.11.046 (2008).

67   Ruoslahti, E. RGD and Other Recognition Sequences for Integrins. *Annual Review of Cell and Developmental Biology* **12**, 697-715, doi:10.1146/annurev.cellbio.12.1.697 (1996).

68   Xu, X. *et al.* Recreating the tumor microenvironment in a bilayer, hyaluronic acid hydrogel construct for the growth of prostate cancer spheroids. *Biomaterials* **33**, 9049-9060, doi:https://doi.org/10.1016/j.biomaterials.2012.08.061 (2012).

69   Park, K. M., Lewis, D. & Gerecht, S. Bioinspired Hydrogels to Engineer Cancer Microenvironments. *Annual Review of Biomedical Engineering* **19**, 109-133, doi:10.1146/annurev-bioeng-071516-044619 (2017).

70   Almany, L. & Seliktar, D. Biosynthetic hydrogel scaffolds made from fibrinogen and polyethylene glycol for 3D cell cultures. *Biomaterials* **26**, 2467-2477, doi:https://doi.org/10.1016/j.biomaterials.2004.06.047 (2005).

71   Pradhan, S., Hassani, I., Clary, J. M. & Lipke, E. A. Polymeric Biomaterials for In Vitro Cancer Tissue Engineering and Drug Testing Applications. *Tissue Eng Part B Rev* **22**, 470-484, doi:10.1089/ten.TEB.2015.0567 (2016).

72 American Cancer Society. *Key Statistics for Prostate Cancer*, <https://www.cancer.org/cancer/prostate-cancer/about/key-statistics.html> (2018).

73 American Cancer Society. *Treating Prostate Cancer*, <https://www.cancer.org/cancer/prostate-cancer/treating.html> (2018).

74 Corn, P. G. The tumor microenvironment in prostate cancer: elucidating molecular pathways for therapy development. *Cancer Management and Research* **4**, 183-193, doi:10.2147/CMAR.S32839 (2012).

75 Josson, S., Matsuoka, Y., Chung, L. W. K., Zhau, H. E. & Wang, R. Tumor–stroma co-evolution in prostate cancer progression and metastasis. *Seminars in Cell & Developmental Biology* **21**, 26-32, doi:https://doi.org/10.1016/j.semcdb.2009.11.016 (2010).

76 Montanari, M. *et al.* Epithelial-mesenchymal transition in prostate cancer: an overview. *Oncotarget* **8**, 35376-35389, doi:10.18632/oncotarget.15686 (2017).

77 Rowley, D. R. What might a stromal response mean to prostate cancer progression? *Cancer Metastasis Rev* **17**, 411-419 (1998).

78 Nelson, A. R., Fingleton, B., Rothenberg, M. L. & Matrisian, L. M. Matrix metalloproteinases: biologic activity and clinical implications. *J Clin Oncol* **18**, 1135-1149, doi:10.1200/JCO.2000.18.5.1135 (2000).

79 Lafleur, M. A., Handsley, M. M. & Edwards, D. R. Metalloproteinases and their inhibitors in angiogenesis. *Expert Rev Mol Med* **5**, 1-39, doi:doi:10.1017/S1462399403006628 (2003).

80 Gilles, C., Newgreen, D. F., Sato, H. & Thompson, E. W. in *Madame Curie Bioscience Database* (Landes Bioscience, 2013).

81 Egeblad, M. & Werb, Z. New functions for the matrix metalloproteinases in cancer progression. *Nature Reviews Cancer* **2**, 161, doi:10.1038/nrc745 https://www.nature.com/articles/nrc745#supplementary-information (2002).

82 Jin, J.-K., Dayyani, F. & Gallick, G. E. Steps in Prostate Cancer Progression that lead to Bone Metastasis. *International journal of cancer. Journal international du cancer* **128**, 2545-2561, doi:10.1002/ijc.26024 (2011).

83 Sobel, R. E. & Sadar, M. D. Cell Lines Used in Prostate Cancer Research: A Compendium of Old and New Lines—Part 1. *The Journal of Urology* **173**, 342-359, doi:https://doi.org/10.1097/01.ju.0000141580.30910.57 (2005).

84 Tai, S. *et al.* PC3 Is a Cell Line Characteristic of Prostatic Small Cell Carcinoma. *The Prostate* **71**, 1668-1679, doi:10.1002/pros.21383 (2011).

85 Fitzgerald, K. A. *et al.* The use of collagen-based scaffolds to simulate prostate cancer bone metastases with potential for evaluating delivery of nanoparticulate gene therapeutics. *Biomaterials* **66**, 53-66, doi:https://doi.org/10.1016/j.biomaterials.2015.07.019 (2015).

86 Fitzgerald, K. A. *et al.* Nanoparticle-mediated siRNA delivery assessed in a 3D co-culture model simulating prostate cancer bone metastasis. *International Journal of*

Pharmaceutics **511**, 1058-1069, doi:https://doi.org/10.1016/j.ijpharm.2016.07.079 (2016).

87   Windus, L. C., Glover, T. T. & Avery, V. M. Bone-stromal cells up-regulate tumourigenic markers in a tumour-stromal 3D model of prostate cancer. *Molecular Cancer* **12**, 112, doi:10.1186/1476-4598-12-112 (2013).

88   Florczyk, S. J. *et al.* 3D Porous Chitosan-Alginate Scaffolds: New Matrix for Studying Prostate Cancer Cell-Lymphocyte Interactions In Vitro. *Advanced healthcare materials* **1**, 590-599, doi:10.1002/adhm.201100054 (2012).

89   Varzavand, A. *et al.* Integrin A3β1 Regulates Tumor Cell Responses to Stromal Cells and can Function to Suppress Prostate Cancer Metastatic Colonization. *Clinical & experimental metastasis* **30**, 541-552, doi:10.1007/s10585-012-9558-1 (2013).

90   Herroon, M. K., Diedrich, J. D. & Podgorski, I. New 3D-Culture Approaches to Study Interactions of Bone Marrow Adipocytes with Metastatic Prostate Cancer Cells. *Frontiers in Endocrinology* **7**, 84, doi:10.3389/fendo.2016.00084 (2016).

91   Sieh, S., Lubik, A. A., Clements, J. A., Nelson, C. C. & Hutmacher, D. W. Interactions between human osteoblasts and prostate cancer cells in a novel 3D in vitro model. *Organogenesis* **6**, 181-188 (2010).

92   Hsiao, A. Y. *et al.* Microfluidic system for formation of PC-3 prostate cancer co-culture spheroids. *Biomaterials* **30**, 3020-3027, doi:https://doi.org/10.1016/j.biomaterials.2009.02.047 (2009).

93   Taubenberger, A. V. *et al.* 3D extracellular matrix interactions modulate tumour cell growth, invasion and angiogenesis in engineered tumour microenvironments. *Acta Biomaterialia* **36**, 73-85, doi:https://doi.org/10.1016/j.actbio.2016.03.017 (2016).

94   Sieh, S. *et al.* Paracrine interactions between LNCaP prostate cancer cells and bioengineered bone in 3D in vitro culture reflect molecular changes during bone metastasis. *Bone* **63**, 121-131, doi:https://doi.org/10.1016/j.bone.2014.02.001 (2014).

95   Bott, K. *et al.* The effect of matrix characteristics on fibroblast proliferation in 3D gels. *Biomaterials* **31**, 8454-8464, doi:https://doi.org/10.1016/j.biomaterials.2010.07.046 (2010).

96   Temenoff, J. S., Athanasiou, K. A., LeBaron, R. G. & Mikos, A. G. Effect of poly(ethylene glycol) molecular weight on tensile and swelling properties of oligo(poly(ethylene glycol) fumarate) hydrogels for cartilage tissue engineering. *J Biomed Mater Res* **59**, 429-437 (2002).

97   Pradhan, S., Hassani, I., Seeto, W. J. & Lipke, E. A. PEG-fibrinogen hydrogels for three-dimensional breast cancer cell culture. *J Biomed Mater Res A* **105**, 236-252, doi:10.1002/jbm.a.35899 (2017).

98   Alconcel, S. N. S., Baas, A. S. & Maynard, H. D. FDA-approved poly(ethylene glycol)-protein conjugate drugs. *Polymer Chemistry* **2**, 1442-1448, doi:10.1039/C1PY00034A (2011).

99   Elbert, D. L. & Hubbell, J. A. Conjugate Addition Reactions Combined with Free-Radical Cross-Linking for the Design of Materials for Tissue Engineering. *Biomacromolecules* **2**, 430-441, doi:10.1021/bm0056299 (2001).

100   Sahni, A. & Francis, C. W. Vascular endothelial growth factor binds to fibrinogen and fibrin and stimulates endothelial cell proliferation. *Blood* **96**, 3772-3778 (2000).

101   Sahni, A., Khorana, A. A., Baggs, R. B., Peng, H. & Francis, C. W. FGF-2 binding to fibrin(ogen) is required for augmented angiogenesis. *Blood* **107**, 126-131, doi:10.1182/blood-2005-06-2460 (2006).

102   Rybarczyk, B. J. & Simpson-Haidaris, P. J. Fibrinogen assembly, secretion, and deposition into extracellular matrix by MCF-7 human breast carcinoma cells. *Cancer Res* **60**, 2033-2039 (2000).

103   Dikovsky, D., Bianco-Peled, H. & Seliktar, D. The effect of structural alterations of PEG-fibrinogen hydrogel scaffolds on 3-D cellular morphology and cellular migration. *Biomaterials* **27**, 1496-1506, doi:https://doi.org/10.1016/j.biomaterials.2005.09.038 (2006).

104   Pradhan, S., Clary, J. M., Seliktar, D. & Lipke, E. A. A three-dimensional spheroidal cancer model based on PEG-fibrinogen hydrogel microspheres. *Biomaterials* **115**, 141-154, doi:10.1016/j.biomaterials.2016.10.052 (2017).

105   Kerscher, P. *et al.* Direct hydrogel encapsulation of pluripotent stem cells enables ontomimetic differentiation and growth of engineered human heart tissues. *Biomaterials* **83**, 383-395, doi:10.1016/j.biomaterials.2015.12.011 (2016).

106   Pradhan, S., Chaudhury, C. S. & Lipke, E. A. Dual-Phase, Surface Tension-Based Fabrication Method for Generation of Tumor Millibeads. *Langmuir* **30**, 3817-3825, doi:10.1021/la500402m (2014).

107   Werb, Z. ECM and Cell Surface Proteolysis: Regulating Cellular Ecology. *Cell* **91**, 439-442, doi:https://doi.org/10.1016/S0092-8674(00)80429-8 (1997).

108   Wallace, D. I. & Guo, X. Properties of Tumor Spheroid Growth Exhibited by Simple Mathematical Models. *Frontiers in Oncology* **3**, 51, doi:10.3389/fonc.2013.00051 (2013).

109   Kalli, M., Papageorgis, P., Gkretsi, V. & Stylianopoulos, T. Solid Stress Facilitates Fibroblasts Activation to Promote Pancreatic Cancer Cell Migration. *Ann Biomed Eng* **46**, 657-669, doi:10.1007/s10439-018-1997-7 (2018).

110   Kalli, M. & Stylianopoulos, T. Defining the Role of Solid Stress and Matrix Stiffness in Cancer Cell Proliferation and Metastasis. *Front Oncol* **8**, 55, doi:10.3389/fonc.2018.00055 (2018).

111   Rice, A. J. *et al.* Matrix stiffness induces epithelial–mesenchymal transition and promotes chemoresistance in pancreatic cancer cells. *Oncogenesis* **6**, e352,

doi:10.1038/oncsis.2017.54   https://www.nature.com/articles/oncsis201754 #supplementary-information (2017).

112   Handorf, A. M., Zhou, Y., Halanski, M. A. & Li, W.-J. Tissue Stiffness Dictates Development, Homeostasis, and Disease Progression. *Organogenesis* **11**, 1-15, doi:10.1080/15476278.2015.1019687 (2015).

113   Lai, Y. *et al.* Current status and perspectives of patient-derived xenograft models in cancer research. *J Hematol Oncol* **10**, 106, doi:10.1186/s13045-017-0470-7 (2017).

114   Pradhan, S. *et al.* A Microvascularized Tumor-mimetic Platform for Assessing Anti-cancer Drug Efficacy. *Scientific Reports* **8**, 3171, doi:10.1038/s41598-018-21075-9 (2018).

115   Prabhakarpandian, B. *et al.* Synthetic tumor networks for screening drug delivery systems. *J Control Release* **201**, 49-55, doi:10.1016/j.jconrel.2015.01.018 (2015).

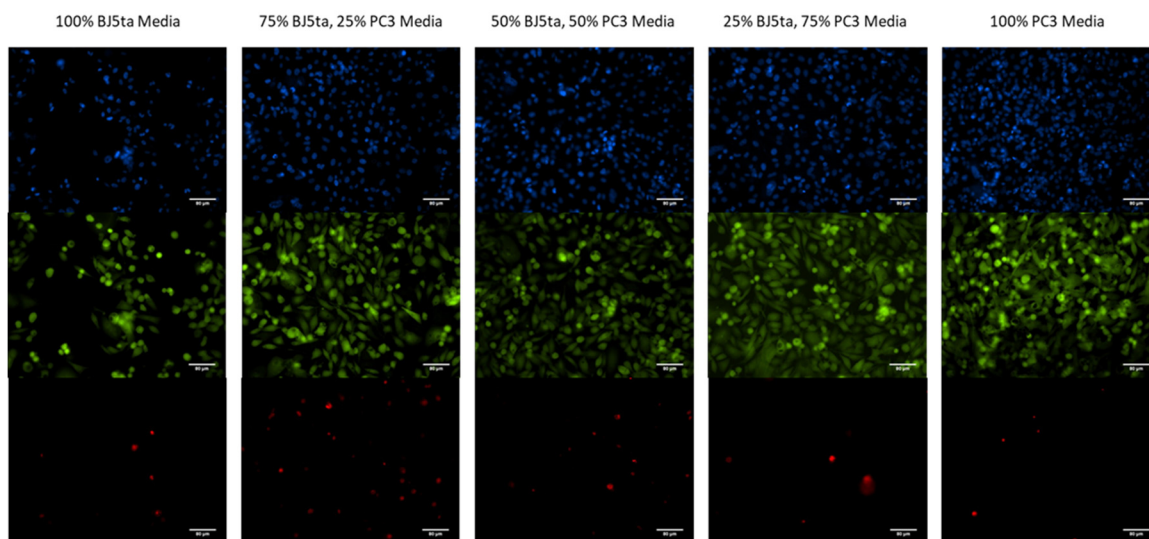**Appendix A: Prostate Cancer and Fibroblast Cell Coculture Medium Determination and Impact**

Figure 63: Analysis of culture media blends on PC-3 cell viability. *A variety of culture media blends were not shown to impact PC-3 cell viability. (20X scale bars = 80 μm)*
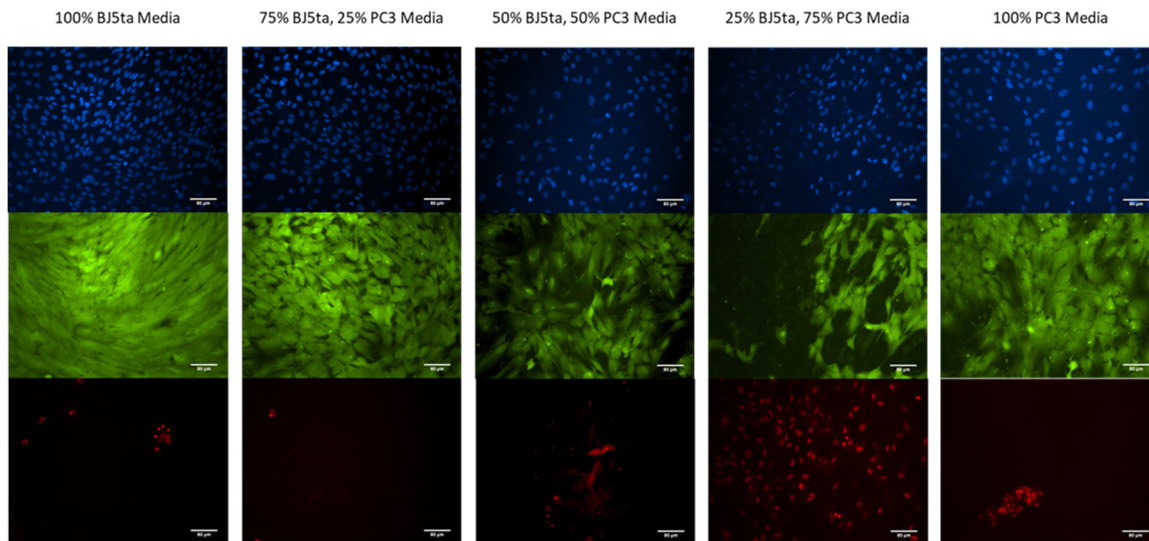
Figure 64: Analysis of culture media blends on BJ-5ta cell viability. *BJ-5ta cells were shown to exhibit slightly increased cell death in increasing levels of PC-3 media. (20X scale bars = 80 μm)*
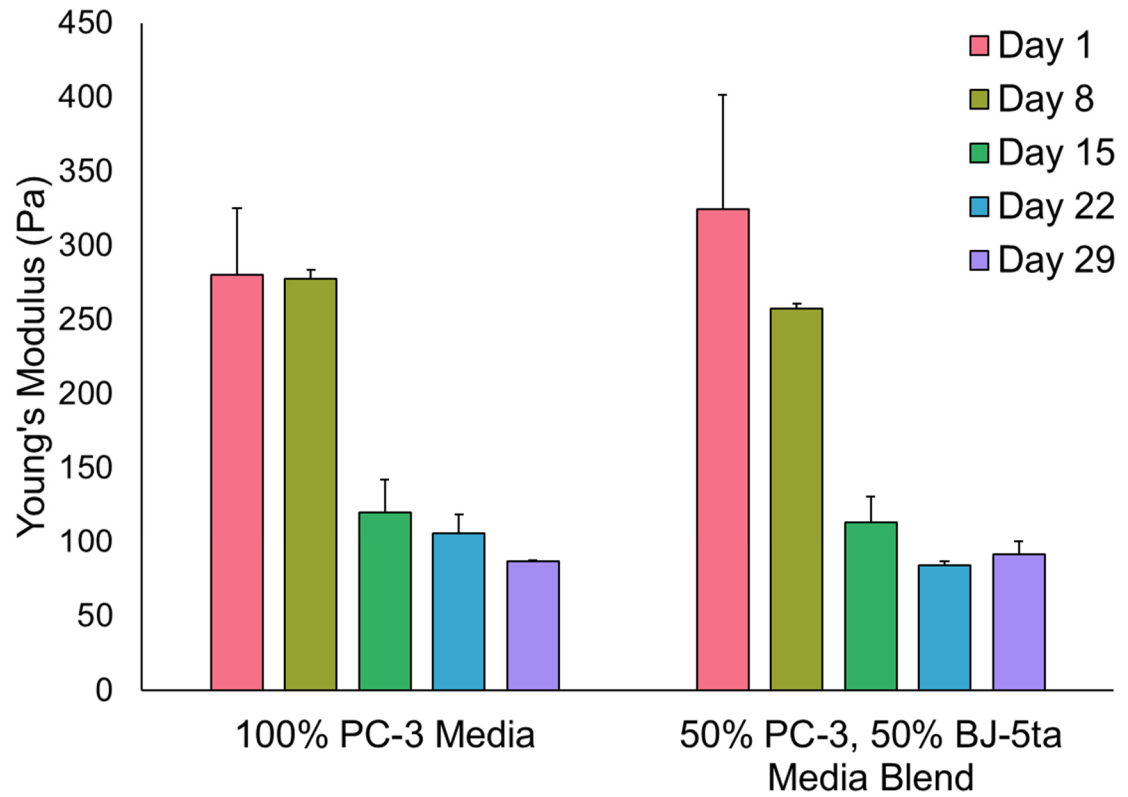
Figure 65: Effect of culture media on mechanical stiffness quantification. *Culture media was not found to affect the decreasing trend in mechanical stiffness with increasing culture duration. (Error bars represent a population based standard deviation)*
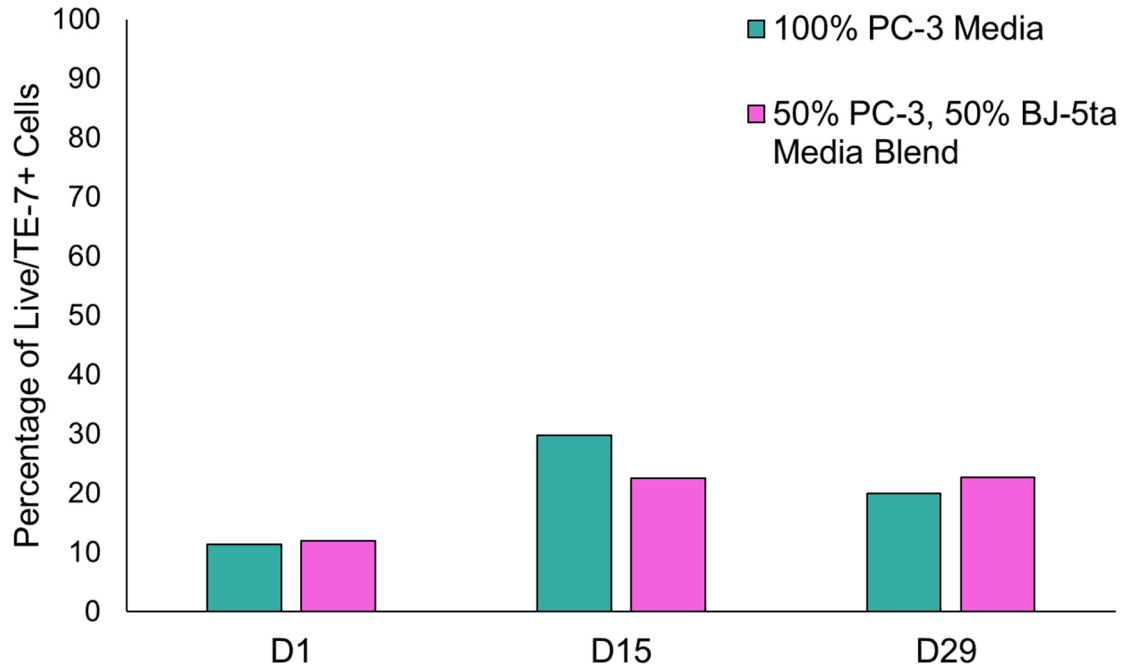
Figure 66: Effect of culture media on cell populations over time. *Culture media was not found to significantly affect the percentage of live fibroblasts in bioengineered tumor tissues on days 1 and 29 post-encapsulation. A slight variation is noted on day 15.*